Queen Mary University of London

Collisionless Magnetic Reconnection in a Stressed X-point Collapse

by

Jan Graf von der Pahlen

supervised by

David Tsiklauri

A thesis submitted in partial fulfilment for the
degree of Doctor of Philosophy

in the
The Space, Solar and Astrophysical Plasmas group
School of Physics and Astronomy

July 2016

Declaration of Authorship

I, Jan Graf von der Pahlen, confirm that the research included within this thesis is my own work or that where it has been carried out in collaboration with, or supported by others, that this is duly acknowledged below and my contribution indicated. Previously published material is also acknowledged below.

- I attest that I have exercised reasonable care to ensure that the work is original, and does not to the best of my knowledge break any UK law, infringe any third partys copyright or other Intellectual Property Right, or contain any confidential material.
- I accept that the College has the right to use plagiarism detection software to check the electronic version of the thesis.
- I confirm that this thesis has not been previously submitted for the award of a degree by this or any other university.
- The copyright of this thesis rests with the author and no quotation from it or information derived from it may be published without the prior written consent of the author.

Signed:
Jan Graf von der Pahlen

Date:
27.07.2016

Queen Mary University of London

Abstract

The Space, Solar and Astrophysical Plasmas group
School of Physics and Astronomy

Doctor of Philosophy

Collisionless Magnetic Reconnection in a Stressed X-point Collapse

by Jan Graf von der Pahlen

Magnetic X-point collapse is investigated using a 2.5D fully relativistic particle-in-cell simulation, with varying strengths of guide-field as well as open and closed boundary conditions. In the zero guide-field case we discover a new signature of Hall-reconnection in the out-of-plane magnetic field, namely an octupolar pattern, as opposed to the well-studied quadrupolar out-of-plane field of reconnection. The emergence of the octupolar components was found to be caused by ion currents and is a general feature of X-point collapse. The effect was shown to be independent of system size and ion mass and confined to a few ion inertial lengths from the reconnection current sheet. In a comparative study of tearing-mode reconnection, signatures of octupolar components are found only in the out-flow region. It is argued that space-craft observations of magnetic fields at reconnection sites may be used accordingly to identify the type of reconnection. Further, initial oscillatory reconnection is observed, prior to reconnection onset, generating electromagnetic waves at the upper-hybrid frequency, matching solar flare progenitor emission. When applying a guide-field, in both open and closed boundary conditions, thinner dissipation regions are obtained and the onset of reconnection is increasingly delayed. Investigations with open boundary conditions show that, for guide-fields close to the strength of the in-plane field, shear flows emerge, leading to the formation of electron flow vortices and magnetic islands. Asymmetries in the components of the generalised Ohm's law across the dissipation region are observed and inertial components are shown to play a role at the X-point. Extended in 3D geometry, it is shown that locations of magnetic islands and vortices are not constant along the height of the current-sheet. Vortices formed on opposite sides of the current-sheet travel in opposite directions along it, leading to a criss-cross vortex pattern. Similarly to oblique current sheets previously observed in 3D guide-field reconnection studies, vortex-tubes are inclined at the same angle as the magnetic field.

Contents

"Students using astrophysical textbooks remain essentially ignorant of even the existence of plasma concepts, despite the fact that some of them have been known for half a century. The conclusion is that astrophysics is too important to be left in the hands of astrophysicists who have gotten their main knowledge from these textbooks."

Hannes Alfvén

Acknowledgements

My thanks go to all the wonderful people that have supported me during my PhD studies, including my supervisor, my family, my friends, my colleagues, the staff at Queen Mary University and the many acquaintances I made along the way.

Publications

The majority of the research presented in this thesis has been previously published in the following publications:

- J. Graf von der Pahlen, D. Tsiklauri, "The effect of guide-field and boundary conditions on collisionless magnetic reconnection in a stressed X-point collapse", Phys. Plasmas 21, 012901 (2014)
- J. Graf von der Pahlen, D. Tsiklauri, "Octupolar out-of-plane magnetic field structure generation during collisionless magnetic reconnection in a stressed X-point collapse", Phys. Plasmas 21, 060705 (2014)
- J. Graf von der Pahlen, D. Tsiklauri, "The effects of ion mass variation and domain size on octupolar out-of-plane magnetic field generation in collisionless magnetic reconnection", Phys. Plasmas 22, 032905 (2015)
- J. Graf von der Pahlen, D. Tsiklauri, "Role of electron inertia and reconnection dynamics in a stressed X-point collapse with a guide-field", Astron. Astrophys. 595, A84 (2016)

Further, the results included in this thesis have been presented at the following meetings:

- National Astronomy Meeting 2013
- National Astronomy Meeting 2014
- UK MHD Meeting 2014
- European Solar Physics Meeting 2014
- National Astronomy Meeting 2015
- UK MHD Meeting 2014
- American Geophysical Union Fall Meeting 2015

Overview

This thesis presents the culmination of my work, which for the most part was independently submitted as four separate journal articles. The structure of this thesis is as follows:

Chapter 1 presents an introduction to plasma and solar physics and relevant scientific and computational concepts that pertain to this thesis. This is done to provide the necessary background for chapters 2, 3 and 4, which are otherwise self-contained.

Chapter 2 contains the scientific findings presented in the journal paper J. Graf von der Pahlen, D. Tsiklauri, Phys. Plasmas 21, 012901 (2014) as well as those of the letter J. Graf von der Pahlen, D. Tsiklauri, Phys. Plasmas 21, 060705 (2014). The results presented in this chapter include general characteristics of X-point collapse with a guide-field, as well as the discoveries of vortex generation, electromagnetic wave excitation and octupolar out-of-plane magnetic field structure.

Chapter 3 contains the scientific findings presented in the journal paper J. Graf von der Pahlen, D. Tsiklauri, Phys. Plasmas 22, 032905 (2015). Here the discovery of out-of-plane magnetic octupolar structure is addressed in detail, including parametric studies and theoretical cosnderations.

Chapter 4 contains the scientific findings presented in J. Graf von der Pahlen, D. Tsiklauri, Astron. Astrophys. 595, A84 (2016). Here the appearance of vortices in X-point collapse simulations is further analysed and it is found that their emergence is the result of a shift in the instability causing the reconnection, i.e. tearing-mode to Kelvin-Helmholtz, as well as a shift in the reconnection mechanism, i.e. pressure tensor terms to inertial terms.

Chapter 5 contains the overarching conclusions of the three preceding chapters.

Chapter 6 provides a discussion on the wider relevance of the results to the plasma and solar physics community.

Chapter 1

Introduction

The works presented in this thesis relate to solar-plasma physics. In physics, a plasma describes a collection of charged particles, interacting in an unbound state. While the term generally refers to ionised gases, i.e. plasmas comprised of electrons and ions, it extends to more abstract cases, including electron-positron and dusty plasmas. In this thesis, unless otherwise specified, plasma refers to an ionised gas.

Based on current models and observations, more than 99% of the mass of the visible matter in the universe is made up of plasma, including stars and accretion disks. Furthermore, the vast majority of known space is occupied by plasma. Main sequence stars constantly emit a stream of plasma in all directions, occupying a volume that spans for hundreds of solar radii. Beyond this radius, space is filled with residual ions and electrons making up the inter-stellar medium. Needless to say, the sheer abundance of plasma in the universe more than justifies the study of plasma processes. The topic of this thesis is magnetic reconnection, which is likely to be responsible for a number of energetic plasma phenomena, including solar flares and, in part, coronal mass ejections.

The works in this thesis relate to reconnection in the solar atmosphere and the Earth-Sun system. While the physical principles relating to magnetic reconnection addressed here equally apply to reconnection in magnetic confinement fusion experiments and in pulsars, the focus of this work is to address the open questions in solar physics, which are discussed in section 1.1.

1.1 Reconnection in the Solar System

The first reference to magnetic reconnection is Dungey's model of magnetic energy conversion in the Earth's magnetosphere [1], which describes a reconnection model now

known as X-point collapse. This is also the first model of the open magnetosphere. Shortly after its publication, magnetic reconnection became the prime candidate mechanism for numerous energetic processes observed on the Sun and in the magnetosphere. The purpose of this section is to outline our current understanding of the Sun and the various observations that lead to the investigation of reconnection mechanisms.

Due to the presence of a magnetic field, particles in a plasma gyrate around field-lines and thus couple the two together. On a most basic level, magnetic reconnection is the decoupling and reconfiguration of a magnetic field from a plasma that it is otherwise frozen into. This can lead to the release of magnetic energy as kinetic energy and heat. The purpose of this section is to explain the role of magnetic reconnection in the open questions and challenges relating to solar physics. It closely follows the reviews on the solar corona contained in [2].

1.1.1 Solar Structure

The structure of the Sun (as illustrated in Fig. 1.1) is a well studied field and a wide consensus exists on its general features [3, 4]. Thermal energy originates from the solar core and powers all dynamical processes inside the Sun and on its surface. The gravitational force pushes the mass of the Sun onto its centre, leading to a particle pressure and density at the core sufficient for nuclear fusion to proceed through the proton-proton chain, i.e. through the reactions

$$^1H + ^1H \rightarrow ^2D + e^+ + v, \tag{1.1}$$

$$^2D + ^1H \rightarrow ^3He + \gamma, \tag{1.2}$$

and

$$^3He + ^3He \rightarrow ^4He + ^1H + ^1H. \tag{1.3}$$

The reaction rate of the first step in this series is comparatively low, as it requires the decay of a proton to a neutron via the weak force. The others however progress rapidly, sustaining a temperature of the order of $10^7 K$. Energy generated at the core is transferred away from the centre, first through thermal radiation in the radiative layer, then via convection in the convective layer. Due to the convectional flows, a strong shear exists in the plasma fluid motion between the two layers, and numerous dynamical features emerge [5]. This separation is known as the tachocline and modern simulations suggest that it plays a significant role in the solar dynamo [6]. At the uppermost layer of the Sun, the reduced plasma density allows for photons being emitted into space, thus coining this layer the photosphere. This layer represents the image of the Sun

that is seen through visible light, including dark regions known as solar spots, which are associated with areas of strong emerging magnetic fields. Beyond this layer a sharp drop in density is observed, marking the transition to the solar atmosphere.

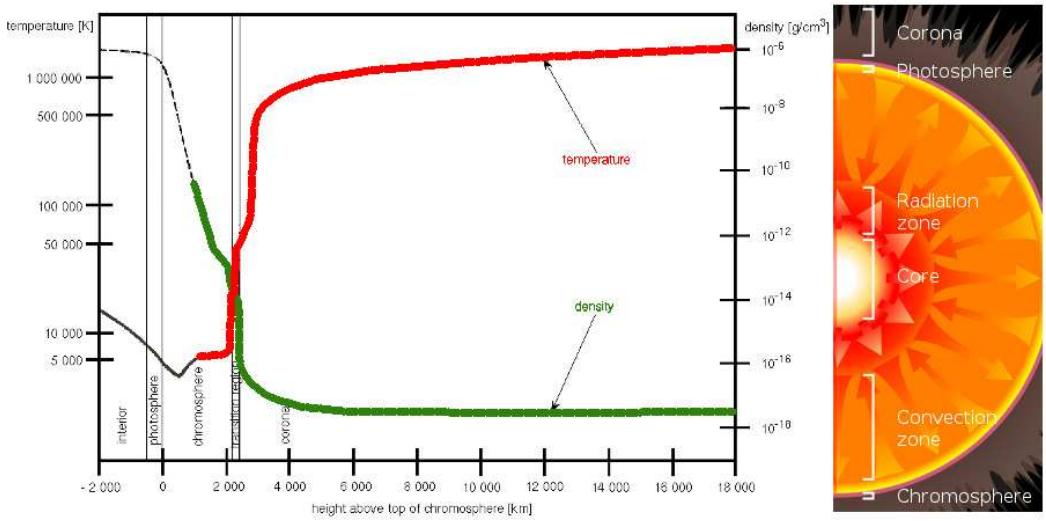

FIGURE 1.1: Showing on the right a cross-section of the Sun, indicating different inner regions, and on the left corresponding temperature and density profiles, taken from [7].

The Sun's atmosphere starts with the chromosphere, which is of notable importance to observable reconnection events. The chromosphere can be viewed through light emitted from H-alpha emission and indicates magnetic filaments, prominences, spicules and bright areas around Sun-spots. Further, emissions can be detected as a responses of solar flares. This is followed by the solar corona, the outermost layer of the Sun. Contrary to expectation, the temperature of of the Sun rises when reaching the solar corona (see Fig. 1.1), rather than cooling as the solar plasma approaches outer space. This is considered one of the major open questions in solar physics. Further, the corona exhibits localised incidences of large X-ray emission, i.e. solar flares, often accompanied by expulsions of plasma, i.e. coronal mass ejections. These events are also associated with brightening of the photosphere and sun quakes [8]. The driving mechanism of these emissions and their role in the coronal heating process is also an active area of investigation. Lastly, from the surface of the Sun, a constant stream of plasma is emitted at speeds of hundreds of kms^{-1} in all directions, known as the solar wind. The solar wind plasma extends to the point where it is slowed down by the inter-stellar medium, making up the heliosphere, which encompasses the Earth and the rest of the solar system.

1.1.2 The Solar Dynamo

As discussed in chapter 11.3 of Ref. [4], the magnetic field of the Sun has also been matter of investigation and was shown to reverse in polarity every eleven years, as first

indicated by the periodic occurrence of maxima and minima in the average number of sunspots. While this process is not fully understood, Babcock in 1961 [9] formulated a model of the solar magnetic dynamo that incorporates this effect (see Fig. 1.2), which is still of relevance today. The model predicts that the magnetic field of the Sun is caused by current flows in the convective layer. Due to the differential rotation of the Sun, and freezing of the magnetic field into the solar plasma, field-lines are dragged along the equator creating a toroidal field component. Convection in the mantle then twists field lines into tubular structures, known as flux ropes. Magnetic pressure pushes these ropes out of the surface, resulting in the sunspot maxima. Flux ropes are then carried towards the poles, changing the average polarity of the magnetic field. Eventually flux ropes diffuse into a new poloidal field with opposite polarity to the original.

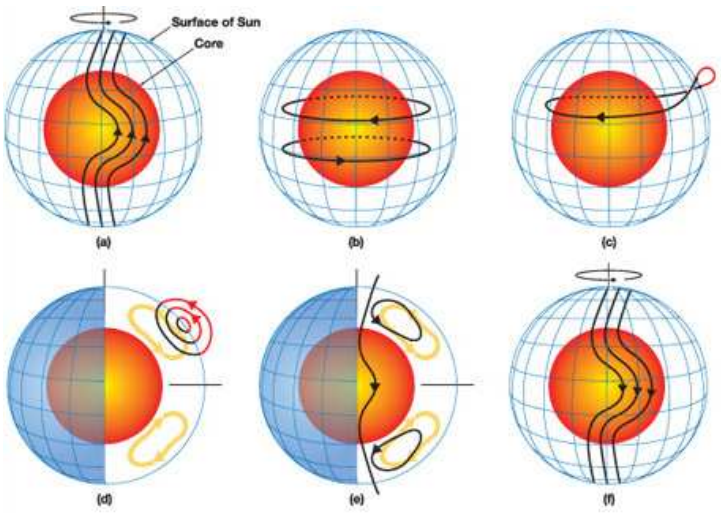

FIGURE 1.2: From Ref. [10], showing the evolution of the Sun's magnetic field during half a solar cycle according to Ref. [9]. Panel a) shows an initial poloidal magnetic field twisted by the differential flow, leading to panel b), where a strong toroidal magnetic field component is established. Panel c) shows flux-ropes being pushed out into the solar surface and carried towards the poles by the convective flow. Panel d) and e) show how the convective flow generates new magnetic field loops, which eventually diffuse to form the reversed poloidal field.

1.1.3 Solar Flares and Coronal Mass Ejections

Solar Flares are explosive phenomena in the solar atmosphere, releasing vast amounts of energy in radiation and heat. These events are often accompanied by coronal mass ejections (CMEs), which are sporadic ejections of large plasma structures (up to $10^{14} kg$ ejections observed [11]), i.e. more so then what is ejected by the solar-wind background. While the nature of these phenomena is not completely understood, the majority of models explaining them are rooted in magnetic reconnection, leading to the standard model of flares [12]. The generally accepted mechanism of solar flaring and CMEs was

given by Hirayama in 1974 [13] and most modern reconnection modelling efforts into flaring are to some extent based on this model. As shown in Fig. 1.3, in this model a magnetic flux rope extends over an area of anti-parallel magnetic field that is tethered in the chromosphere. Reconnection occurs in the anti-parallel magnetic field, pushing up the flux rope and generating energetic particles that travel along the field to the photosphere. Light is emitted at the surface while the plasma contained in the flux rope is pushed out into space.

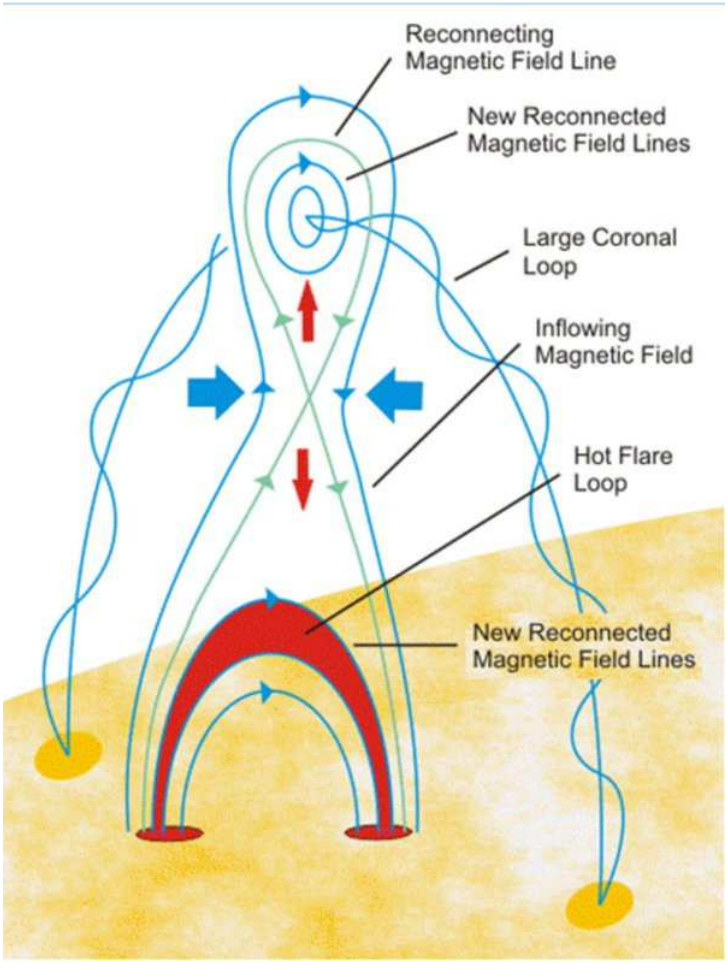

FIGURE 1.3: From Ref. [14] showing Hiryama's model of a flaring coronal loop [13], project on the surface of the Sun.

Currently, numerous numerical simulations are being carried out to gain a better understanding of the reconnection process in flaring regions [11, 15]. Also, using a semi-analytical model, using magnetorgrams as input, remarkable progress has been made in predicting energy releases in pre-flaring regions in the solar corona [16]. Furthermore, hundreds of flares have been observed and catalogued [17], and an empirical relationship has been established by Shibata, linking flaring temperature, density and magnetic field strength [18]. Despite the apparent order implied by this relationship, the sizes of flares greatly vary, allowing for what has been coined super flares, which have been

shown to occur on solar-type stars [19]. The potentially destructive effect of a flare of extreme proportions on a technologically advanced society stresses the need for a clear understanding of the flaring process.

1.1.4 Coronal Heating and Solar Wind Acceleration

A number of physical models have been proposed to explain the effect of coronal heating, involving mechanisms including:

- Stress-induced magnetic reconnection - magnetic energy conversion to heat (see Ref. [20]).
- Stress-induced current cascades - Ohmic dissipation due to currents induced from magnetic field foot-point movements in the lower solar atmosphere (see Ref. [21]).
- Stress-induced turbulence - magnetic foot-point motion leading to large eddy currents being pumped up to the corona which cascade through turbulent motion to smaller scales (see Ref. [22]).
- Alfvénic Resonance/Absorption - energy transferred upwards from the chromosphere and photosphere as waves into the corona (see Ref. [23]).

Further, spectral analysis shows the occurrence of Micro-Flares, seen in Soft X-Rays, and Nano-Flares, seen in EUV. Having an energy release far lower than previously observed flares, but also a far greater occurrence, it was speculated to be a viable mechanism for coronal heating. A modern consensus on observation places the limits of energy output by micro and nano flares in a range including the limits for the energy requirements of coronal heating [24]. Naturally, also in this case, the prime candidate for the cause of the flaring is reconnection, here over minuscule reconnection sites.

The solar wind can be separated into two types, namely the unsteady slow solar wind (about $300 kms^{-1}$) emanating from temporarily active magnetic regions, and the steady fast solar wind (about $800 kms^{-1}$), emanating from polar coronal holes. The acceleration of the fast solar wind has energy requirements of a similar extent to that of coronal heating, with the added modelling challenge of restoring particle density and recreating observed particle distributions. To date, no adequate model has been derived to describe the fast solar-wind acceleration, but a strong case has been made that such a model would require a full consideration of particle kinetics [25]. Further a strong case can be made for the involvement of Alfvén waves in the acceleration process of solar wind ions (see Ref. [26]).

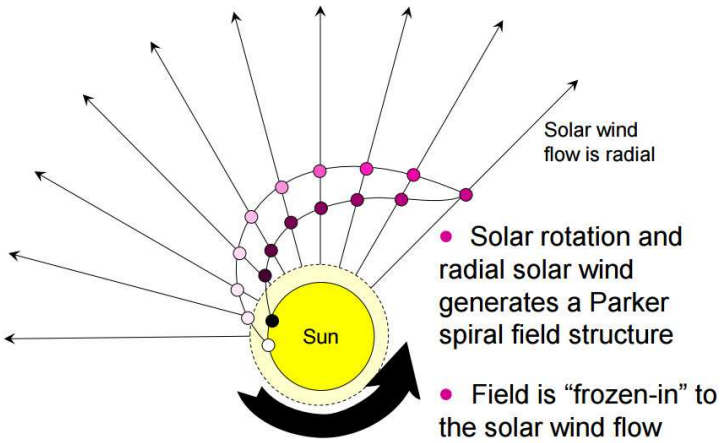

FIGURE 1.4: From Ref. [27] showing the how magnetic field-line freezing of a coronal loop and the rotation of the Sun lead to the formation of the Parker Spiral.

1.1.5 The Sun-Earth System

Accelerated solar-wind particles couple with the magnetic field of the Sun and drag it outwards into the solar-system. Due to the rotation of the Sun, and variation in the local polarity of the Sun's magnetic field, the solar-wind magnetic field direction spirals away from the Sun (see Fig. 1.4). Since the magnetic field varies in strength perpendicular to the field direction, this gives rise to the heliospheric current sheet (see Ref. [28]), where evidence for magnetic reconnection has been detected by satellite missions (see Ref. [29]).

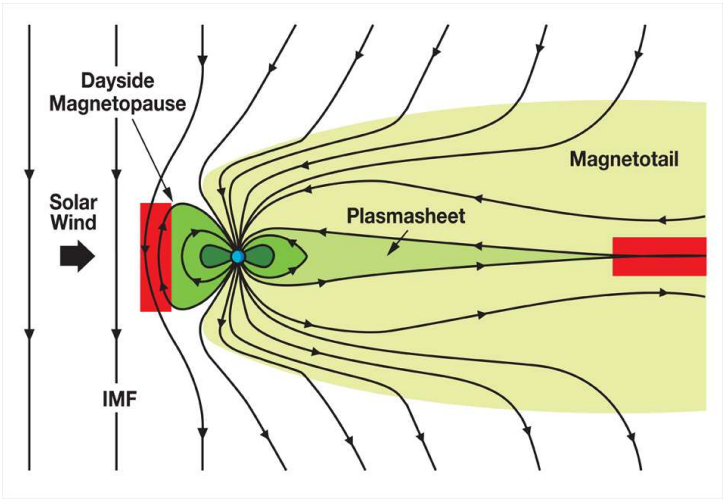

FIGURE 1.5: From Ref. [30] showing day-side and night-side reconnection of the Sun's magnetic field with the magnetic field of the Earth due to the solar wind.

The interaction of the Sun's magnetic field with the Earth has a great impact on the Earth's magnetopshere, and in rare cases leads to solar wind particles entering the

inner atmosphere, causing effects such as the northern lights. When the two fields are aligned (e.g. when both point northwards), no interaction occurs and the Sun's magnetic field passes around the Earth. However, when the fields are anti-aligned, a reconnection region forms between the Sun and the Earth (dayside of the magnetosphere) and opened field-lines are dragged past the Earth, further away from the Sun (see Fig. 1.5). When opened field-lines are dragged far enough, their distances reduces, forming the magneto-tail at the nightside of the magnetosphere, where they again reconnect and close the Earth's magnetic field. Observational studies show reconnection at the dayside is highly asymmetric, leading to the motion of reconnection sites along the southwards and northwards along the Earth's magnetic field [31]. At the nightside, the stretched-out magnetic-field lines form a highly symmetric reconnection region, allowing for theoretical signatures of magnetic reconnection to be tested (see Ref. [32]). Works in this thesis aims to add to both of these branches of investigation of reconnection in the magnetosphere.

1.2 Fundamentals of Plasma Physics

This section serves to introduce the reader to the concepts of plasma physics pertaining to this thesis. The derivations shown here closely follow those in plasma physics books by Dendy [33], Fitzpatrick [34] and Burgess [35].

1.2.1 The Plasma State

Just like in solids, liquids and gases the components of a plasma consist of electrons and ions, interacting predominantly through the electromagnetic force. Similarly to the transition from liquids to gases, a sufficient increase in energy can facilitate a transition from gas to plasma, i.e. the ionisation of the gas. When a gas is ionised, free charges become the force carriers and a new state of matter is reached with distinctly different properties. Due to the lack of atomic structure, a plasma is free of magnetisation or polarisation, and Maxwell's equation for a plasma can always be represented as follows:

Gauss's law:

$$\nabla \cdot \mathbf{E} = -\frac{\rho}{\epsilon_0} \tag{1.4}$$

Gauss's law for magnetism:

$$\nabla \cdot \mathbf{B} = 0 \tag{1.5}$$

Faraday's law of induction:

$$\nabla \times \mathbf{E} = -\frac{\partial \mathbf{B}}{\partial t} \tag{1.6}$$

Ampère's law:

$$\nabla \times \mathbf{B} = \mu_0 \mathbf{J} + \frac{1}{c^2}\frac{\partial \mathbf{E}}{\partial t} \tag{1.7}$$

These equations prescribe the dynamics of magnetic and electric fields in a plasma and thus determine how charged particles in the plasma are accelerated by the Lorentz force,

$$\mathbf{F} = q(\mathbf{E} + \mathbf{v} \times \mathbf{B}). \tag{1.8}$$

Since charged particles themselves interact through their own electric fields, in the absence of external forces, a plasma adopts a state of quasi-neutrality. Here particles are arranged to shield other charges such that on average the plasma appears neutral. Perturbing this quasi-neutral state by a shift in the electron or ion density leads to a restorative electric field and hence an oscillatory motion. The frequency of this oscillation is characteristic physical property of every plasma and is known as the plasma frequency. It is trivial to show using Gauss's law and Stoke's theorem that the electron and ion plasma frequencies are given by

$$\omega_{pe}^2 = \frac{n_e e}{m_e \epsilon_0}, \quad \omega_{pi}^2 = \frac{Z n_i e}{m_i \epsilon_0}. \tag{1.9}$$

where e is the electron charge, m_e and m_i are the electron and ion mass respectively, n_0 the particle density and Z the number of protons per ion (for simplicity, throughout this thesis Z is assumed to be 1 and number densities are assumed equal, i.e. $n_e = n_i = n_0$).

In order to observe the effects of plasma oscillations, time scales must be considered which are longer than the plasma oscillation period, i.e. $1/\omega_{pe}$. I.e. time scales over which the dynamics of the plasma particles average out. Similarly length scales must be considered that are large enough such that charge screening is effective and the plasma appears quasi-neutral. This length essentially represents the distance from an ion at which its charge is effectively screened by electrons, and is known as the Debye length. The Debye screening due to a test charge can be determined as follows: for a plasma perturbed by a point-charge Q, resulting in an electric potential ϕ, Boltzmann's equation gives the number densities of electrons and ions as

$$n_e = n_0 e^{-e\phi/k_B T}, \quad n_i = n_0 e^{e\phi/k_B T}. \tag{1.10}$$

Accordingly the charge density of the plasma surrounding Q is given by

$$\rho = e(n_i - n_e) = -2n_0 e \sinh(e\phi/k_B T). \tag{1.11}$$

Using the fact that i.e. $\mathbf{E} = -\nabla\phi$, we can rewrite Gauss's law as

$$\nabla^2\phi = -\rho/\epsilon_0, \tag{1.12}$$

and substituting Eqn. (1.11) into Eqn. (1.12) gives a spatial relationship of the electric potential of the form

$$\nabla^2\phi = \frac{2n_0 e}{\epsilon_0} \sinh(e\phi/k_B T). \tag{1.13}$$

since the strength of ϕ reduces with distance from Q, at a large enough distance the potential energy falls below the electron thermal energy and $\sinh(e\phi/k_B T) \approx e\phi/k_B T$. Thus Eqn. (1.13) can be expressed as

$$\nabla^2\phi = \frac{2e^2 n_0 e}{\epsilon_0 k_B T}\phi. \tag{1.14}$$

In other words, the potential due to Q is diminished over a length scale of the order of

$$\lambda_D = \sqrt{\frac{\epsilon_0 k_B T}{e^2 n_0 e}}, \tag{1.15}$$

where λ_D represents the Debye length.

Furthermore, due the Lorentz force, the presence of a magnetic field in a plasma leads to charged particles particles moving in gyro orbits perpendicular to the direction of the magnetic field. By equating the centripetal force of an orbiting charged particle with the Lorentz force, the cyclotron frequencies for electrons and ions are found as.

$$\omega_{ce} = \frac{q_e B}{m_e}, \omega_{ci} = \frac{q_i B}{m_i}. \tag{1.16}$$

Since electrons and ions are oppositely charged, they orbit in opposite directions and since ions are heavier, their period of oscillation is much longer. The natural state of oscillation in magnetised plasma is in part determined by the thermal energy of particles and we obtain the cyclotron radius of particles by dividing the their thermal speed by their gyro frequency i.e.

$$r_{ce} = \frac{v_{the}}{\omega_{ce}}, r_{ci} = \frac{v_{thi}}{\omega_{ci}}. \tag{1.17}$$

The parameters given in this section represent the most defining features of the collective plasma interaction and will be used throughout this thesis.

1.2.2 Collisionless Plasma and Flux Freezing

Like all interacting many-body systems, plasmas can be either collisional or collisionless, meaning that ranges over which their mean free path, λ_{mfp}, extends can be small or large compared to the size of the system. In a collisional plasma, particles interact directly with each other and experience coulomb collisions, whereas in collisionless plasma particles interact only through the collective electromagnetic field. For a given electron, we can approximate the mean free path by equating the coulomb potential to another charged particle with the thermal energy of that electron, such that

$$\frac{e^2}{4\pi\epsilon_0 r_C} = \frac{3}{2}k_b T_e, \tag{1.18}$$

and derive from it the interaction distance, r_C, which can be used to obtain the interaction cross-section and hence the mean free path:

$$\lambda_{mfp} = \frac{1}{n_0 \sigma_C} = \frac{1}{n_0 \pi r_C^2} = \left(\frac{6\epsilon_0 k_b T_e}{e^2\sqrt{\pi n_0}}\right)^2. \tag{1.19}$$

When collisions are relevant in a plasma, i.e. when λ_{mfp} is smaller than the size of the system, they result in an effective resistivity, known as the Spitzer resistivity. When an electric field is applied in this case, a plasma behaves like a resistor and electrons require forcing simply to move past ions. We can thus write the equation of motion of electrons as

$$m_e \frac{d\mathbf{v_e}}{dt} = -e\mathbf{E} - e\mathbf{v} \times \mathbf{B} - \frac{\nabla \cdot \mathbf{P_e}}{n_e} - m_e \nu_{ei}(\mathbf{v_e} - \mathbf{v_i}). \tag{1.20}$$

where the terms on the right hand side are, from left to right, the electric field, magnetic advection, the divergence of the electron pressure tensor and the added collision term, for collisions between electrons and ions for a collision frequency ν_{ei}.

In most astrophysical plasmas resistivity is estimated to be very small. Thus charges can move virtually without obstruction and the plasma behaves as a super-conductor. I. e. electric fields accelerate particles without loss of energy and the resistivity is zero. Currents therefore do not require an electric field to be sustained and the collision term can be neglected. For a collisionless plasma we thus rewrite equation 1.20 in the form of an Ohm's law as

$$\mathbf{E} + \mathbf{v_e} \times \mathbf{B} = -\frac{\nabla \cdot \mathbf{P_e}}{n_e e} - \frac{m_e}{e}\frac{\partial \mathbf{v_e}}{\partial t} - \frac{m_e}{e}(\mathbf{v_e} \cdot \nabla)\mathbf{v_e}. \tag{1.21}$$

In solar corona and many other astrophysical plasmas the mean free path of electrons is generally much larger than the spatial scales over which these plasmas exist. For this reason, this thesis focuses of collisionless plasmas and Eqn. 1.21 will be used in the analysis of plasma dynamics.

In the absence of collisions, inertial effects or pressure divergences, a plasma is considered ideal and Eqn. 1.21 reduces to

$$\mathbf{E} = -\mathbf{v} \times \mathbf{B}, \tag{1.22}$$

where $\mathbf{v_e}$ now matches the mean velocity of the plasma. Further applying the Faraday's law of induction yields

$$\frac{\partial \mathbf{B}}{\partial t} = \nabla \times (\mathbf{v} \times \mathbf{B}). \tag{1.23}$$

From this relationship it can be shown that the magnetic flux, Φ, through a given surface S does not change as this surface moves with the plasma. I.e. $\frac{d\Phi_S}{dt} = 0$. We can define the rate of change of flux through an open surface S as

$$\frac{d\Phi_S}{dt} = \int_S \frac{\partial \mathbf{B}}{\partial t} \cdot d\mathbf{S} + \oint_C \mathbf{B} \cdot \mathbf{v} \times d\mathbf{l}, \tag{1.24}$$

where $\mathbf{v} \times d\mathbf{l}$ is the velocity of plasma elements on the boundary of the surface. Inserting Eqn. 1.23 into the first term on the right hand side gives

$$\frac{d\Phi_S}{dt} = \int_S \nabla \times (\mathbf{v} \times \mathbf{B}) \cdot d\mathbf{S} + \oint_C \mathbf{B} \cdot \mathbf{v} \times d\mathbf{l}. \tag{1.25}$$

Applying Stokes' theorem then shows that the two terms on the right cancel and

$$\frac{d\Phi_S}{dt} = 0. \tag{1.26}$$

When considering a magnetic field as a set of unbroken flux-tubes, the implication of this result is that plasma is coupled to the flux-tubes, meaning that neither can move independently and particles are thus 'frozen' into the field. Therefore, moving plasmas can transport magnetic fields or magnetic fields can trap plasma depending on the particular configuration of the system.

On the other hand, in the strongly collisional case, we can neglect the pressure and inertial terms and rewrite equation 1.20 as

$$\mathbf{E} + \mathbf{v_e} \times \mathbf{B} = \eta \mathbf{j}, \tag{1.27}$$

where $\mathbf{v_e} - \mathbf{v_i}$ has been replaced with $\mathbf{j}/e$ and η represents the resistivity. Here, the only response to an electric field is to drive a current through the resistive medium. While this approximation most closely resembles materials in a non-plasma state it has become the basis for countless numerical simulations due the simplicity in its applicability.

1.2.3 Dissipative Plasma Instabilities

Throughout the solar system there are flux-frozen plasmas that are in a stable state. However, in certain configurations, a perturbation to the state of a plasma can lead to self-sustained dynamical changes (i.e. an instability), which in turn can lead to transformations in the magnetic structure of the plasma. While there are multitudes of possible plasma instabilities (see ref. [36]), here we will focus on some of the unstable systems which are of known relevance to reconnection studies, namely the tearing-mode instability, X-point collapse and the Kelvin-Helmholtz instability (see Fig. 1.6).

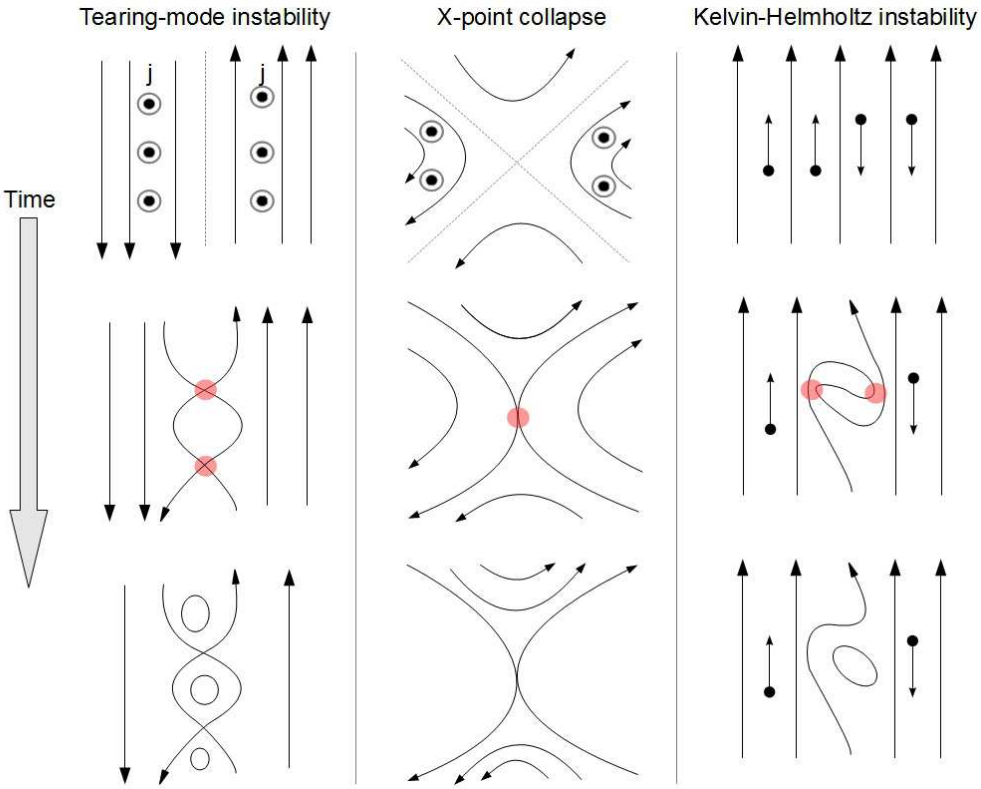

FIGURE 1.6: We show from left to right the evolution of the tearing-mode instability, X-point collapse and the Kelvin-Helmholtz instability.

Ref. [37] presents an analysis of plasmas containing a planar magnetic field of the form $B_y = B_0 x$, with an out-of-plane current, j_z. The Lorentz force (or $\mathbf{j} \times \mathbf{B}$ force in this case) acts to push field lines towards the $x = 0$ line, but is countered by the plasma pressure. When allowing for magnetic-field annihilation as a function of $\nabla \times \mathbf{B}$ and adding perturbations that squeeze field lines together along the $x = 0$ line, a self-sustained process is initiated: magnetic field-lines are pushed towards points of annihilation due to the $\mathbf{j} \times \mathbf{B}$ force while plasma is moved away along the $x = 0$ line with newly reconnected field-lines. This instability is known as the tearing-mode instability and has been subject to numerous reconnection studies.

A simple modification to this setup is to introduce an additional sheared magnetic field in the x direction, i.e. $B_x = B_0' y$. In this case, magnetic field dissipation occurs at a predetermined point where magnetic separatrices meet, i.e. the X-point. This setup is the earliest proposed model of magnetic reconnection (see Ref. [1]) and is the prime focus of this thesis.

When rather than a shear in magnetic field, a velocity shear is imposed on a plasma, small perturbations in the interface between the two velocity regimes tend to grow as they are being dragged along by the flows, leading to a growing instability. In extreme cases this can lead to the formation of flow vortices. This process is known as the Kelvin-Helmholtz (KH) instability. In studies of collisionless plasmas, where a sheared velocity field was imposed parallel to a magnetic field (see Ref. [38]), the KH instability was shown to deform field lines, causing local compressions, which in turn lead to magnetic field dissipation (see Fig. 1.6). This type of instability will also be addressed in this thesis (see chapter 4).

1.2.4 Plasma Waves

The excitation of waves in a magnetised plasma is determined by the response of the plasma to electromagnetic excitations, which is determined by the Lorentz force. For an electron plasma with a uniform unidirectional magnetic field (here defined to be in the z direction), the acceleration of the plasma parallel to the magnetic field due to an electric field component is given by

$$\frac{\partial \mathbf{v_z}}{\partial t} = -\frac{e}{m}\mathbf{E_z}, \tag{1.28}$$

while the acceleration perpendicular to the magnetic field is given by

$$\frac{\partial \mathbf{v}_\perp}{\partial t} = \frac{q}{m}\mathbf{E}_\perp + \boldsymbol{\omega_{ce}} \times \mathbf{v}_\perp. \tag{1.29}$$

Substituting Eqn. (1.29) into the time derivative of Eqn. (1.29) gives

$$\frac{\partial^2 \mathbf{v}_\perp}{\partial t^2} + \omega_{ce}^2 \frac{\partial \mathbf{v}_\perp}{\partial t} = -\frac{e}{m}\left(\frac{\partial \mathbf{E}_\perp}{\partial t} + \boldsymbol{\omega_{ce}} \times \mathbf{E}_\perp\right). \tag{1.30}$$

Substituting a waveform of $\mathbf{A}e^{i(\mathbf{kr}-\omega t)}$ for $\mathbf{E}$ and $\mathbf{v}_\perp$ into Eqns. (1.28) and (1.30) gives relations between electric field and plasma velocities as

$$-i\omega \mathbf{v_z} = -\frac{e}{m}\mathbf{E_z}, \tag{1.31}$$

and

$$(\omega_{ce}^2 - \omega^2)\mathbf{v}_\perp = -\frac{e}{m}\left(-i\omega\mathbf{E}_\perp + \omega_{ce} \times \mathbf{E}_\perp\right), \tag{1.32}$$

which can be represented in matrix form as

$$\mathbf{v} = \mathbf{a} \cdot \mathbf{E} = \begin{vmatrix} \frac{i\omega}{\omega_{ce}^2-\omega^2} & \frac{\omega_c e}{\omega_{ce}^2-\omega^2} & 0 \\ \frac{-\omega_{ce}}{\omega_{ce}^2-\omega^2} & \frac{i\omega}{\omega_{ce}^2-\omega^2} & 0 \\ 0 & 0 & -\frac{i}{\omega} \end{vmatrix}. \tag{1.33}$$

Assuming a plasma of constant electron density, we relate the electron velocity to a current in the form of an Ohm's law, i.e.

$$\mathbf{j} = -en\mathbf{v} = -en\mathbf{a} \cdot \mathbf{E} = \sigma \cdot \mathbf{E}, \tag{1.34}$$

where σ does not refer to the overall conductivity of the plasma, but the microscopic response of particles to an electric field (the same derivation applies to the ion plasma, except that the sign of ω_{ci} is reversed relative to ω_{ce}).

σ can be applied in Ampère's law such that

$$\nabla \times \mathbf{B} = \mu_0\mathbf{J} + \frac{1}{c^2}\frac{\partial \mathbf{E}}{\partial t} = (\mu_0\sigma - \frac{i\omega}{c^2}\mathbf{I}) \cdot \mathbf{E} = -\frac{i\omega}{c^2}\epsilon \cdot \mathbf{E}, \tag{1.35}$$

where ϵ represents the plasma permittivity tensor. By further applying a time differential and substituting Faraday's law of induction, the relationship becomes

$$0 = \nabla^2\mathbf{E} - \nabla(\nabla \times \mathbf{E}) + \frac{\omega^2}{c^2}\epsilon \cdot \mathbf{E} = (\mathbf{kk} - k^2\mathbf{I} + \frac{\omega^2}{c^2}\epsilon) \cdot \mathbf{E} = \mathbf{M} \cdot \mathbf{E}. \tag{1.36}$$

To fulfil the above equation, the relation $det(\mathbf{M}) = 0$ must hold true, and from this the relationship between wave frequency, ω, and wave vector, $\mathbf{k}$, can be determined for any direction of wave propagation.

The relationship between ω and $\mathbf{k}$ depends on the direction of wave propagation relative to the magnetic field, while the wave speed is given by the derivative $\frac{\partial\omega}{\partial k}$. For a plasma of a given density and magnetic field these relationships can be displayed in the form of a dispersion diagram as shown in 1.7. Using the dispersion diagram of an observed wave pattern we can identify the wave-mode and draw conclusions about its origin (see chapter 2). Plasma waves are important both in the driving of magnetic reconnection and generating the signatures thereof.

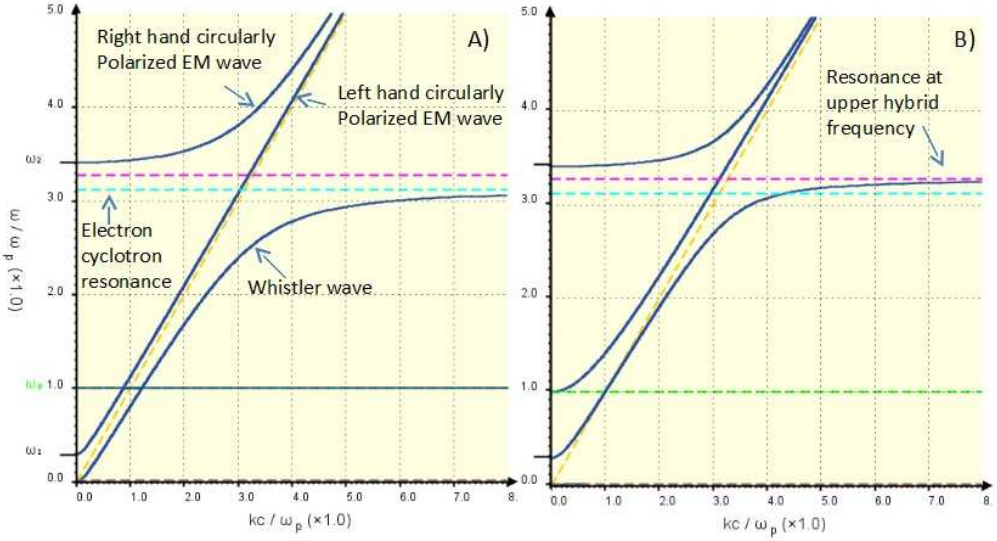

FIGURE 1.7: The dispersion plots for a plasma with $n_0 = 10^{14}m^{-3}$ and B = 0.01T, with wave propagation at an angle relative to B of 0 degrees, showing right-hand and left-hand polarised modes (left) and 90 degrees, showing the ordinary and extraordinary wave modes (right).

1.3 Magnetic Reconnection in 2.5D

Like most substances, plasma in nature exhibits three dimensional (3D) qualities. However, the physical interactions of ions and electrons do not depend on the existence of a third spatial dimension and plasmas can be modelled in two dimensions. When modelled this way, particles in the plasma only have two spatial components (i.e. in x and y), yet three velocity components can be included (v_x, v_y, v_z), where the out-of-plane velocity component does not affect the particle position. Modelling a plasma in such a position-velocity space has been coined 2.5D and it allows for a unique treatment of magnetic fields in plasmas.

Due to a lack of 3D structure in the 2.5D case, flux-frozen magnetic fields can not be treated as flux-tubes, but rather as magnetic field lines, i.e. an arbitrary array of unbroken lines tracing the in-plane components of the magnetic field. Here, a useful tool in analysing the movement of magnetic field lines is the magnetic vector potential, $\mathbf{A}$, defined as

$$\mathbf{B} = \nabla \times \mathbf{A}\,, \quad \mathbf{E} = -\nabla\phi - \frac{\partial \mathbf{A}}{\partial t}, \tag{1.37}$$

where ϕ represents the electric potential. If we consider a magnetic field $\mathbf{B} = B_x\hat{\mathbf{x}} + B_y\hat{\mathbf{y}}$ defined over a plane of coordinates x and y, the value of the out-of-plane component of the magnetic vector potential, A_z, represents a contour whose equipotential lines trace the direction of the in-plane magnetic field. Due to gauge-invariance, we can define an arbitrary $A_z(0,0)$ and integrate over the plane to find the value of A_z at an arbitrary

position (x', y') on the plane, i.e.

$$A_z(x', y') = A_z(0, 0) + \int_0^{y'} B_x 0, y + \int_0^{x'} B_y x, y'. \tag{1.38}$$

Defining magnetic field lines as equipotential lines on A_z makes it possible to track the dynamics of magnetic fields and thus that of the frozen-in plasma. Also, from this definition, we see that A_z effectively represents an in-plane magnetic flux-function. Changes in A_z thus correspond to changes in magnetic flux.

A further consequence of this definition is that the rate of change of A_z is equal to the out-of-plane electric field, i.e.

$$E_z = -\frac{\partial A_z}{\partial t}, \tag{1.39}$$

since there can be no gradient in ϕ in the out-of-plane direction. This shows that any changes in the magnetic field lines must correspond to an out-of-plane electric field. Such an electric field can generally be attributed to magnetic advection, i.e. term $\mathbf{V} \times \mathbf{B}$, where $\mathbf{V}$ corresponds to the movement of field lines. However, at a point where the magnetic field is zero, there is no magnetic field component to move, i.e. $\mathbf{V} \times \mathbf{B} = 0$, and instead the electric field must correspond to a reconfiguration of field lines. In the case of an O-point, i.e. at maxima or minima of an magnetic field, this reconfiguration progresses as an annihilation or generation of magnetic field lines. On the other hand, an X-point in the field lines corresponds to a saddle point in the vector potential. Here field lines move towards the null-point from opposite directions, change topology and the reconfigured field-lines move away in the perpendicular direction.

In order for such magnetic field reconfiguration to occur, by neccesity there must exist a magnetic X-point and the out-of-plane electric field at the X-point by neccesity provides the rate at which field lines are chaging topology, i.e. E_z at the X-point can be used as a measure of the reconnection rate.

1.3.1 Resistive Modelling of 2.5D Reconnection

The earliest attempts of modelling magnetic reconnection were based in Magneto–Hydrodynamics (MHD), which is to say that they treated plasmas as magnetised fluids where ions and electrons move together in the plane as one and quantities such as velocity or density can be treated as a property of the fluid. i.e. $n_e, n_i, \mathbf{v_e}$ and $\mathbf{v_i}$ reduce to n_0 and $\mathbf{V}$. This similarly applies to the Spitzer resistivity, η, as well as the current, $\mathbf{J}$.

In this framework we can take the form of the Ohm's law given in Eqn. 1.27 and apply Faraday's law of induction to obtain the induction equation,

$$\frac{\partial \mathbf{B}}{\partial t} = \nabla \times (\mathbf{V} \times \mathbf{B}) + \eta \nabla^2 \mathbf{B}. \tag{1.40}$$

The first term on the right represents magnetic advection, i.e. movement of field lines and plasma, and the second term on the right dissipation through resistivity. In the MHD approach, this equation governs the dissipation or generation of magnetic fields.

1.3.1.1 Purely Resistive Reconnection - Sweet

In 1956 Sweet proposed a model of merging coronal loops, based on magnetic diffusion, which he later published in Ref. [39]. This represents one of the first mathematical treatments of magnetic reconnection. Here we consider a magnetic field, defined over a thin strip of length $2L$ and width $2l$, representing the diffusion region between two coronal loops (see Fig. 1.8). The direction of the field is parallel to the length of the strip and its strength is strongly sheared across the middle of the strip such that the two sides of the diffusion region have opposite field strength. Assuming that the diffusion term dominates, Eqn. 1.40 reduces to

$$\frac{\partial \mathbf{B}}{\partial t} = \eta \nabla^2 \mathbf{B}, \tag{1.41}$$

and the strong shear at the centre smooths out over the diffusion region until $\eta \nabla^2 \mathbf{B}$ is diminished (see panel (c) of Fig. 1.8).

By substituting B_0 as the initial magnetic field strength of both halves of the diffusion region and l as the characteristic length scale in Eqn. 1.41 we obtain an equation for the characteristic time scale, τ_s, of the diffusion process as

$$\tau_s \approx \frac{l^2}{\eta}, \tag{1.42}$$

i.e. the time scale of the Sweet reconnection model. Since, as discussed, the resistivity of solar plasmas is negligibly small, while length scales of solar processes are large, when inserting characteristic solar parameters into Eqn. 1.42, one obtains reconnection time scales of the order of hundreds of years [40], which stands in strong contrast to flaring time scales, which have been observed to be of the order of hours [15].

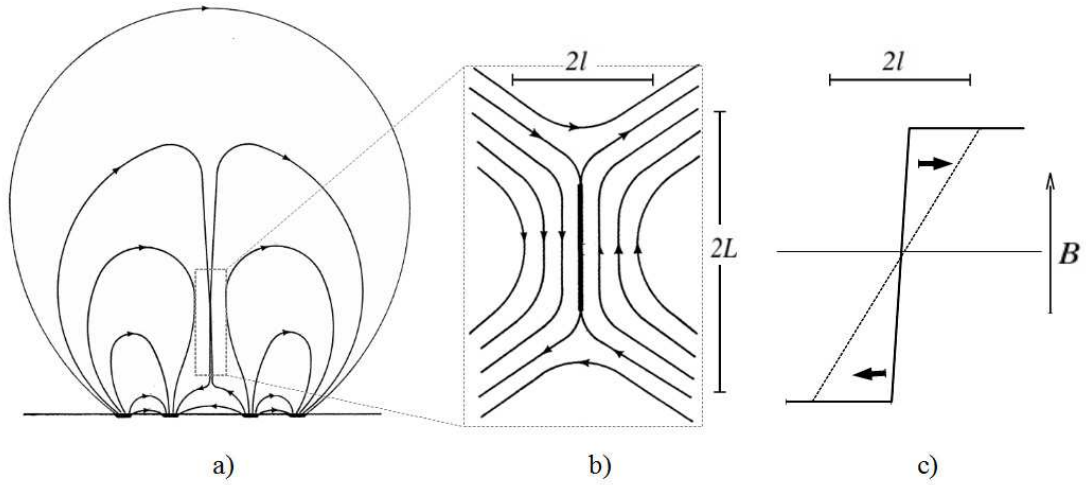

FIGURE 1.8: After [39], showing in (a) a schematic sketch of two coronal loops, in (b) the sheared magnetic field making up the diffusion region between the two coronal loops, and in (c) the profile of the magnetic field strength across the diffusion region, where the solid line and the dashed line show the sheared magnetic field before and after diffusion respectively.

1.3.1.2 Resistive Diffusion and Advection - Sweet-Parker

Shortly following Sweet's initial analysis, Parker published a modified model including the advection term of Eqn. 1.40 [40]. Here we again consider a sheared magnetic field over a thin sheet of length $2L$ and width $2l$. Again, magnetic diffusion occurs at the centre of the magnetic field, but unlike in the purely resistive case, the shear gradient is maintained by a constant inflow of magnetic field lines from both sides of the diffusion region (See Fig. 1.9). If we further assume that reconnected field-lines are removed through the width of the diffusion region, we can assume a steady system, i.e. $\frac{\partial \mathbf{B}}{\partial t} = 0$, and Eqn. 1.40 reduces to

$$\nabla \times (\mathbf{V} \times \mathbf{B}) = -\eta \nabla^2 \mathbf{B}. \tag{1.43}$$

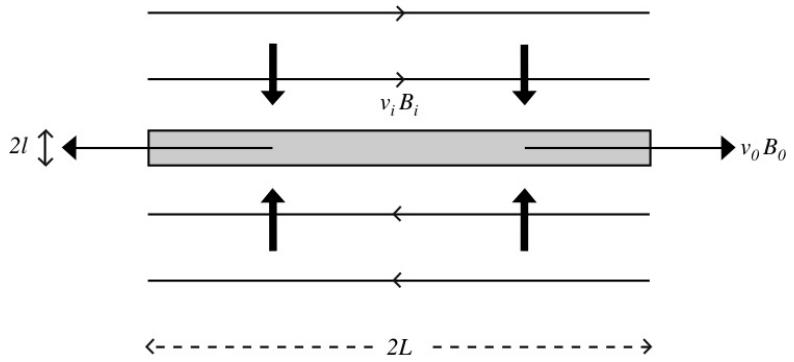

FIGURE 1.9: From Ref. [41], showing the Sweet-Parker reconnection model.

Again we substitute the characteristic length scales, i.e. l, for the spatial gradients and determine the relationship between the inflowing magnetic field, the inflow speed and the diffusion width length to be

$$\frac{V_{in}B_{in}}{l} = -\eta\frac{B_{in}}{l^2}. \tag{1.44}$$

Secondly we note that, due to particle number conservation, the inflow speed at the edge of the diffusion region is related to the outflow speed by $n_{in}V_{in}L = n_{out}V_{out}l$. Treating the plasma as incompressible, $n_{in} = n_{out}$ this relationship reduces to

$$V_{in}L = V_{out}l. \tag{1.45}$$

Lastly, we note that plasma from the centre of the diffusion region is accelerated towards the outflow region by a force corresponding to the gradient of the plasma pressure over that region, such that $\Delta P_p = \frac{\rho V_{out}^2}{2}$. Assuming force balance, the plasma pressure difference between the centre and the edge of the diffusion region can be set as the magnetic pressure at the inflow region, i.e. $\Delta P_p = \frac{B_{in}^2}{2\mu_0}$. Thus we find

$$V_{out} = \frac{B_{in}}{\sqrt{\rho\mu}}, \tag{1.46}$$

which implies that the outfow speed is given by the Alfvén speed at the inflow region, i.e. $V_{out} = V_{A,in}$. Combining equations 1.44, 1.45 and 1.46 the reconnection speed of Sweet-Parker's model is given as

$$V_{in} = \sqrt{\frac{\eta V_{A,in}}{L}}, \tag{1.47}$$

which in turn gives a dimensionless rate of reconnection as

$$M = \frac{V_{in}}{V_{A,in}} = \sqrt{\frac{\eta}{LV_{A,in}}} = \frac{1}{\sqrt{R_m}}, \tag{1.48}$$

where R_m is the magnetic Reynolds number.

In contrast to Sweet's original model, the Sweet-Parker reconnection velocity scales with $L^{-1/2}$ and B_{in} (or $R_m^{-1/2}$), rather than $1/L$ which allows for higher reconnection regimes to be reached. While this model provides some improvement on the original analysis by Sweet, it still falls short of reproducing flaring velocities. Based on solar-corona parameters, V_{in} falls between $10^{-6}V_{A,in}$ and $10^{-3}V_{A,in}$ [42], which is much smaller than flaring speeds observed.

1.3.1.3 Shock Mediated Resistive Reconnection - the Petscheck Model

A reconnection model capable of describing solar eruptions needed to be orders of magnitude faster than the Sweet-Parker model. In 1964 Petschek proposed a modification that both provides an increased reconnection rate, as well as a reconnection region geometry that relates the model to real physical systems (see Ref. [43] and Ref. [42], section 4.3). In this model, a smaller diffusion region lies embedded in a larger magnetic structure of characteristic scales. Here we denote B_e as the external magnetic field and B_i as the internal magnetic field (see Fig. 1.10). The outer region effectively represents a Sweet-Parker Inflow region, and has a size corresponding to characteristic solar length scales, whereas the inner region is much smaller and mediates the physical dynamics in manner that allows for fast reconnection. In order to connect the two regions, the model uses shock-fronts, where magnetic field line directions are discontinuous.

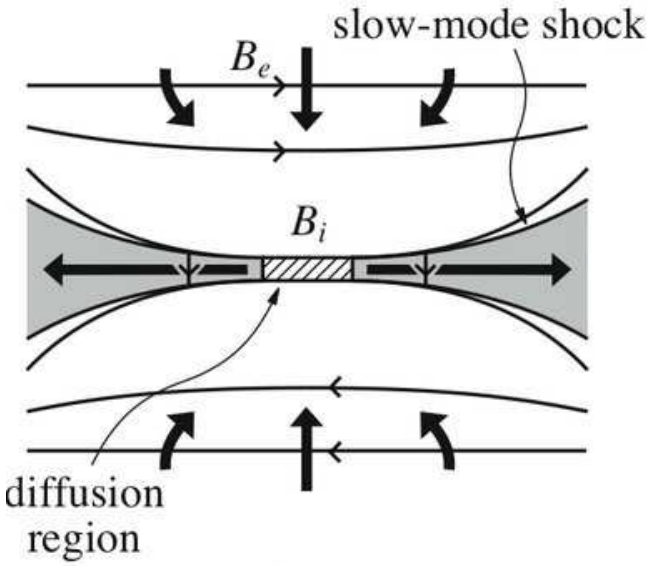

FIGURE 1.10: From Ref. [41] showing Petschek's model of reconnection

The scaling between the two regions is determined by flux-conservation, i.e. $V_e B_e = V_i B_i$. Assuming the outflow speed to be the Alfven speed in the larger and the smaller region, this gives a scaling of the reconnection rate of

$$\frac{M_i}{M_e} = \frac{B_e^2}{B_i^2}. \tag{1.49}$$

Combining Equation 1.49 and Equation 1.48 and considering that, and by imposing that $B_i \approx B_e$, this relation can be expressed as

$$\frac{L_i}{L_e} \approx \frac{1}{R_{me} M_e^2}. \tag{1.50}$$

In the mathematical treatment of Petschek's shock fronts, it is assumed that the difference between the external and internal magnetic field is small, and based on shock dynamics and geometric considerations is found to be

$$B_i = B_e \left(1 - \frac{4M_e}{\pi} \ln\left(\frac{L_e}{L_i}\right)\right). \tag{1.51}$$

Substituting Eqn. 1.50 into Eqn. 1.51, a relation is obtained showing a scaling of the external reconnection velocity with the inverse of the log of the external magnetic Reynolds number, i.e.

$$M_e \sim \frac{1}{\ln R_{me}}, \tag{1.52}$$

thus providing a reconnection speed greatly enhanced to the Sweet-Parker model, which scales with $1/R_{me}$. Effectively that means that a sheared magnetic field region of a characteristic length scale L_e corresponds to a logarithmically smaller inner region of length L_i, where fast reconnection is possible, both being connected through shocks (see Fig. 1.11). As long as this geometry is maintained the reconnection can be fast. While Petschek's analysis included several assumptions, some of which arbitrary by his own admission, his model of fast reconnection became the prime justification for the investigation of magnetic reconnection as an energy release mechanism in the Sun.

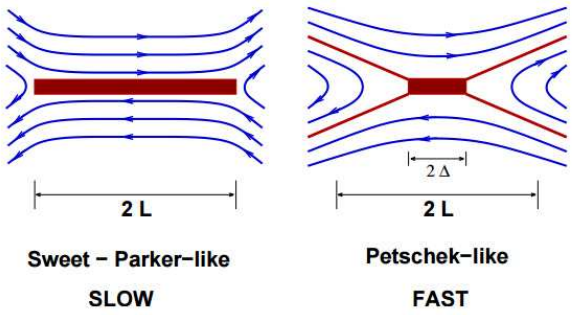

FIGURE 1.11: From Ref. [44] showing on the left Sweet-Parker and on the right Petschek type reconnection. As discussed in [45], under reconnection with uniform resistivity an initial Petschek setup diffuses into a Sweet Parker one.

However, later numerical modelling results of magnetic reconnection lead Biskamp to concluded that Petschek type reconnection was not sustainable and quickly diffused into a Sweet-Parker like setup [45], reducing the impact of this result (see Sect. 1.3.1.4).

1.3.1.4 Resistive MHD Modelling

Since 1980 numerous studies of 2.5D MHD simulations have been carried out to test the viability of fast Petschek reconnection. Being based in MHD, the simulation treated

plasmas as a single fluid on a simulation grid, where each grid point contains a value for the various simulation parameters. In order to do so, simulations need to solve the MHD equations iteratively. These equations are given by

- Mass conservation:

$$\frac{\partial \rho}{\partial t} + \nabla \cdot (\rho \mathbf{V}) = 0 \tag{1.53}$$

This condition assures that no mass gets created or destroyed on the simulation grid.

- Equation of motion:

$$\rho \left(\frac{d}{dt} + \mathbf{V} \cdot \nabla \right) \mathbf{V} = \mathbf{J} \times \mathbf{B} - \nabla p \tag{1.54}$$

This shows that the rate of change of momentum has to be equal to the force components on the grid, which are the pressure divergence and the Lorentz force. Due to quasi-neutrality, the force contribution from any electric field is always zero.

- Energy conservation:

$$\frac{\mathrm{d}}{\mathrm{d}t} \left(\frac{p}{\rho^{\gamma}} \right) = 0 \tag{1.55}$$

Here γ is the specific heat ratio. Depending on the nature of the simulation, more complex variations of this equation have been used to account for heating processes.

For a given initial configuration of density, velocity, plasma pressure and magnetic field, where the initial magnetic field is constrained by Gauss's law, these equations determine the evolution of ρ, $\mathbf{V}$ and P. The evolution of the magnetic field is in turn determined by the nature of the resistive Ohm's law, given by

$$\mathbf{E} + \mathbf{V} \times \mathbf{B} = \eta \mathbf{j}, \tag{1.56}$$

which when substituted into Faraday's law gives the time evolution of the magnetic field as

$$\frac{\partial \mathbf{B}}{\partial t} = \nabla \times (\mathbf{V} \times \mathbf{B}) + \eta \nabla^2 \mathbf{B}, \tag{1.57}$$

where a uniform value of η, i.e. uniform resistivity has been assumed. By applying a leap-frog algorithm the simulation iteratively computes the values of ρ, $\mathbf{V}$, P and $\mathbf{B}$ to give the evolution of the system.

The first simulation of MHD reconnection of this kind was carried out by Biskamp [45] and showed that for an initial Petschek configuration, the magnetic field and velocity flow field would quickly devolve into a Sweet-Parker like configuration. I.e. The length of the initial small current sheet grew and the inflow speed decreased, bringing the system into a slow-reconnection regime. It was later shown by Erkaev, in a slightly modified MHD simulation [46], that a Petschek like reconnection can be maintained if resistivity is

defined only along a thin region along the current sheet and set as zero everywhere else. Similarly MHD simulations by Otto [47] show that increased reconnection rates can be reached when a resistivity proportional to the out-of-plane current is applied. Despite the lack of a physical justification, studies based on anomalous resistivity remained the primary focus of reconnection studies for several decades (see Ref. [48]) and even in modern studies, no consensus on the justification of its application has been reached (see Ref. [49]).

1.3.2 Collisionless Plasma Modelling

1.3.2.1 Collisionless Kinetic Theory

In an analysis including collisionless processes in reconnection dynamics by Vasyliunas [50] in 1975, it was shown that different terms in the generalised Ohm's law would play a role at different scale lengths from the point of reconnection (i.e. the X-point): the divergence of the non-scalar pressure tensor terms, resulting from the meandering motion of electrons, plays a role where magnetic forces cease to determine the electron motion, i.e. up to the electron cyclotron radius (r_{ce}); electron inertial terms play a role up to the electron inertial length ($c\omega_{pe}^{-1}$); and ion inertial terms (the Hall term) play a role up to the ion inertial length ($c\omega_{pi}^{-1}$).

Further, Sonnerup in 1979 [51] considered the two-dimensional structure of the collisionless diffusion region and pointed out that, due to the difference in the distance between the ion and electron acceleration regions near the X-point, decoupled electrons travel further into the diffusion region, leading to an inflowing current (j_x) as shown in Fig. 1.12. Thus, for charge to be conserved there need to be additional perpendicular currents (j_y) leading in and out of the diffusion region, creating loop structure and a quadrupolar magnetic field. This theoretical prediction presented a basis on which current understanding of magnetic reconnection could be tested in simulations, and later in observations.

1.3.2.2 The Hall-MHD model

The lack of self-consistent MHD simulations of fast-reconnection posed a serious demand for models that contained the necessary physics to make magnetic reconnection work. The simplest computational model that allows for the inclusion of decoupled electron-ion dynamics is known as Hall-MHD. While the inclusion of electron-ion decoupling is only one effect that distinguishes MHD to fully collisionless modelling, it would later be shown to be a vital contribution to fast reconnection. In this model we employ the same

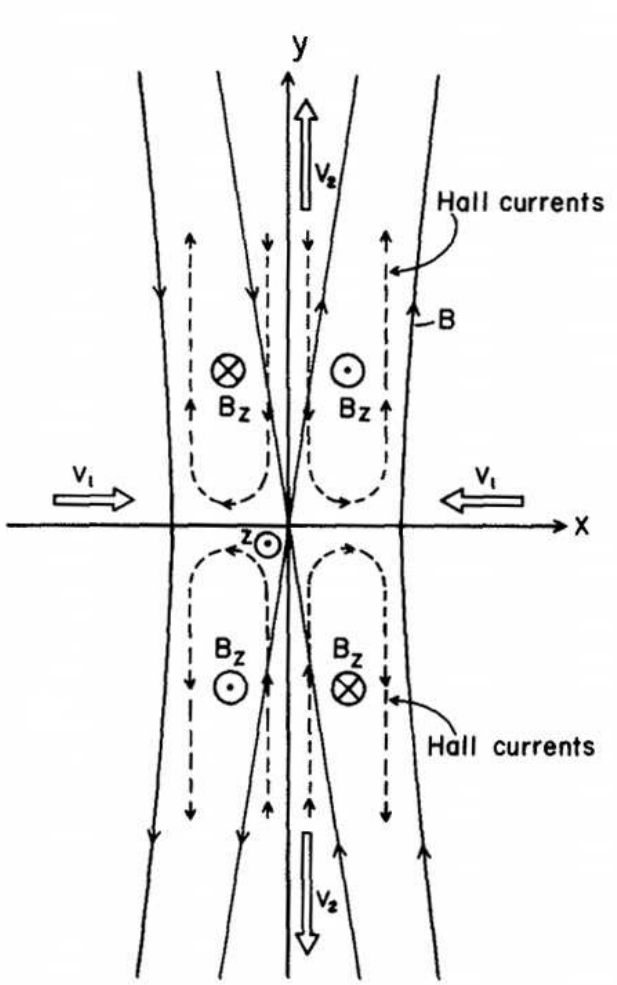

FIGURE 1.12: From [51], showing the Hall electron currents and out-of-plane magnetic field in the collisionless diffusion region as predicted by Sonnerup.

MHD equations, i.e. equations (1.53), (1.54) and (1.55), but use an Ohm's law that is adjusted to account for the fact that the magnetic field near the X-point is frozen only into the electron fluid, i.e. $\mathbf{E} = \mathbf{v_e} \times \mathbf{B}$. This can be accounted for by the inclusion of the Hall-term, $\frac{\mathbf{J}\times\mathbf{B}}{en_0}$, in the generalised Ohm's law such that

$$\mathbf{E} + \mathbf{v} \times \mathbf{B} = \frac{\mathbf{J} \times \mathbf{B}}{en_0}. \tag{1.58}$$

where $\mathbf{v}$ now represents the ion bulk velocity, $\mathbf{v_i}$, and $\mathbf{J} = en_0(\mathbf{v_i} - \mathbf{v_e})$. For an initial planar shear magnetic field, and a corresponding out-of-plane current, the direction of the Hall term is also in the plane, and thus applying Faraday's law now leads to a growth of an magnetic field in the out-of-plane direction. This gives rise to Sonnerup's quadrupolar field as has been demonstrated in numerical Hall simulations [47]. Reconnection in this model was shown to be fast, restoring faith in the possibility of magnetic

reconnection mediating eruptive energetic events in the Sun.

In addition to the Hall-term, several other approximations from the electron equation of motion (i.e. Eqn. 1.20) can be added to account for electron inertia and electron pressure, giving an Ohm's law of the form

$$\mathbf{E} + \mathbf{v} \times \mathbf{B} = \eta \mathbf{J} - \frac{\mathbf{J} \times \mathbf{B}}{e n_0} - \frac{\nabla \cdot P_e}{e n_0} + \frac{m_e}{n_0 e^2} \frac{d\mathbf{J}}{dt}. \tag{1.59}$$

However, as this type of simulation lacks full particle dynamics, pressure can only be treated as a scalar. Also, since the all the terms are added manually, rather than naturally emergent, this type of model cannot tell us about the specifics of the particle dynamics involved in the reconnection processes. Nevertheless, the model is a great step forward from resistive MHD and proves the importance of collisionless processes in reconnection.

1.3.2.3 Kinetic models - Particle-In-Cell and Hybrid Codes

A completely different approach to the ad-hoc method to modelling applied in the Hall-MHD model is to use a kinetic model, where plasmas are modelled as collections of charged particles, interacting with self-consistent electromagnetic fields (descriptions used in this section are based on [52]). In a standard kinetic model the force on every particle is the sum of the electric field contributions from all other particles in the system. For simulations of astrophysical plasmas with a typical density this would require a summation of the order of 10^{16} particles per meter cubed of simulation domain, which is far too computationally demanding for modern parallel high performance computing clusters to model over meaningful spatial scales. The well-studied particle-in-cell (PIC) model, first fully formulated in Ref. [53], addresses this problem two-fold: firstly it does so by grouping and representing particles by a smaller number of super-particles. Secondly, the super-particles do not physically collide, but their dynamical information is used to compute electric and magnetic field quantities on a discrete simulation grid (similarly to the MHD case), which is then in turn used to accelerate the particles. A particle pusher routine is thus used to determine the change in velocity of the super-particles based on the corresponding Lorentz-force. Unlike in the MHD case, no assumptions need to be made about charge neutrality and the system can be evolved naturally without loss of generality. The updated positions and velocities of the super-particles are then used to update the values of current and number densities on the grid, as shown in 1.13.

Each super-particle represents a number of particles, here either electrons or ions, and is thus assigned a spatially dependent distribution function, or shape function, of the form

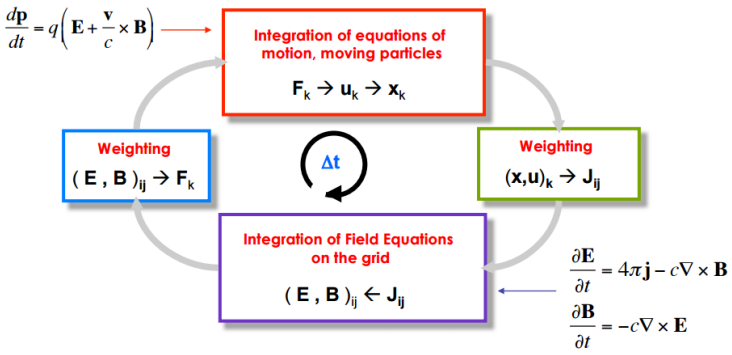

FIGURE 1.13: from [54], showing the computational processes carried for each time-step in a PIC code, where Δt represents teh simulation time-step.

$S(\mathbf{x} - \mathbf{x_p})$, where $\mathbf{x_p}$ is the position vector of the super-particle and $\mathbf{x}$ is an arbitrary position on the grid. While $\mathbf{x}$ is a continues variable that can take any value, field variables are restricted to positions on the simulation grid, i.e. $\mathbf{E}$ and $\mathbf{B}$ have discrete position values. The shape function thus determines the interaction of the super-particles with the field values defined on the simulation grid, such that the effective field interacting with the particle takes the form

$$\mathbf{E}(\mathbf{x}) = \sum_i \mathbf{E}_i S(\mathbf{x}_i - \mathbf{x_p}), \tag{1.60}$$

where $\sum_i$ represents the summation over the simulation grid points. This effectively gives a weighting to each field-super-particle interaction. Based on the chosen shape-function, super-particles can have an effective size corresponding to the particles they represent, and the calculations by the code can be more physically representative, but can also add to the demand on the computing processor.

Both the use of super-particles and a discrete grid is associated with numerical errors. Thermal fluctuations in particle motion, i.e. random meandering of particles from one grid cell to another, results in fluctuations in field values at grid points, which can result in a low signal-to-noise ratio, making the results of the simulation difficult to interpret [55]. Because of this, a great enough numbers of super-particles, and to a lesser degree more complex shape functions, are required to reduce this effect. In most simulations this requires super-particle numbers of the order of 100 particles per grid cell. A further consequence of discrete grid cells is that electromagnetic field structures are sampled only at grid locations, rather than continuously, which can creates new wave-modes (aliases) that tend to destabilise plasma oscillations (see Ref. [56, 57]). This effect is known as the finite grid instability. While particle momentum is preserved to machine accuracy, this instability can lead to spurious changes in system energy if not accounted for, which can be accomplished by limiting the length of grid cells to approximately the

Debye length. As shown in Ref. [57], for PIC simulations a simulation grid cell size of $\Delta l = 2\lambda_D$ was sufficient to negate the instability and preserve total energy. Further, the energy conservation and stability of the simulation depends on the type the size of the simulation time-step and field-particle solver used (for more details see Appendix A).

A substantial alternative simulation model to the standard PIC model are hybrid codes. Here, ions are modelled as super-particles, while electrons are treated as a massless fluid. The advantage of this methodology is that the code no longer has to be resolved at electron inertial time or length scales. As such, hybrid codes are the least computationally demanding models that allow for full kinetic treatment of ions.

1.3.2.4 Successes of Collisionless Modelling

In one of the largest collective works relating to reconnection physics, the Geospace Modelling (GEM) challenge [58], several types of simulation models were tested against each other using different numerical codes and a number of conclusions were drawn about the nature of reconnection modelling. All results were obtained by modelling tearing-mode reconnection in a Harris-sheet setup, which is a pressure balanced current-sheet setup. All simulations used an initial magnetic field of the form

$$\mathbf{B} = B_0 \tanh(x/\lambda)\mathbf{e}_z, \tag{1.61}$$

where λ represents the initial half-width of the current sheet. The initial temperature is set to be uniform and a particle density is set to be

$$n_{e,i} = n_0' \operatorname{sech}^2(x/\lambda) + n_b, \tag{1.62}$$

such that the thermal pressure along the current-sheet balances the external magnetic pressure, i.e. $n_0 kT = B_0^2/\mu_0$. An initial current density satisfying Ampère's law is thus provided by uniform ion and electron velocities normal to the simulation grid.

An overarching consensus was established relating the to reconnection rates reached in different reconnection simulations: In all simulation runs that accounted for the decoupling of ions and electrons (Hall-MHD, PIC and Hybrid), fast reconnection rates (i.e. where $\frac{E_{Z,X-point}}{V_A B_0} > 0.1$) were reached. Purely resistive simulations were only fast when a localised resistivity was defined, here taken to be proportional to the current density [47]. The most prominent plot of the study, as shown in panel a) of Fig. 1.14, shows the change in magnetic flux between the X-point and the simulation boundary, which equates to the reconnection rate integrated over time. As shown, all simulation types exhibit similar dynamics apart from the pure MHD case. It has thus been concluded

that the mechanism that sustains the reconnection electric field does not determine the reconnection rate and that only Hall dynamics (i.e. ion inertial effects) need to be accounted for to achieve fast reconnection.

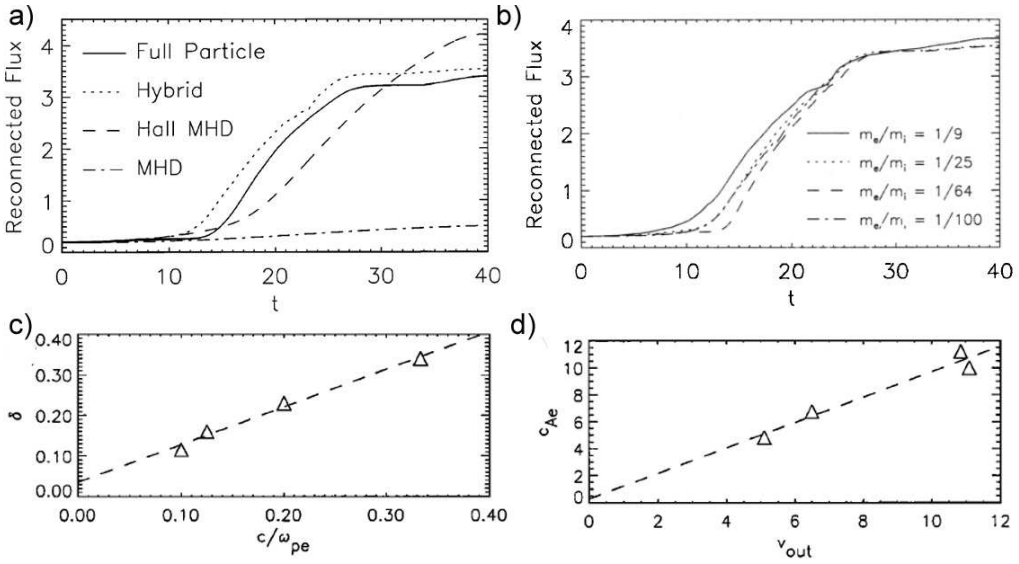

FIGURE 1.14: Plots from studies based on the GEM reconnection setup [58, 59], showing in a) the growth of reconnected flux for different reconnection models, normalised by the initial magnetic flux between the simulation boundary and the X-point, over time, normalised by the ion cyclotron frequency; in b) similarly showing reconnected flux for different electron masses in a PIC code; c) showing electron diffusion region widths as a function of electron plasma frequency in a PIC code; d) showing outflow speed as function of the Alfvén speed for a PIC code

Furthemore, as shown in Ref. [59], in the same setup, changing the electron mass in PIC simulations does also not affect the rate of reconnection (see panel b) of Fig. 1.14). Instead, increasing the electron mass leads to an increased diffusion region width, preserving the relationship, M=$V_{in}/V_{A,e} = l/L$, as proposed by Parker (see Eqn. (1.45)). As a result, the diffusion region width scales with the electron inertial length, c/ω_{pe}, as shown in panel c) of Fig. 1.14. This further shows that, while decoupled electron dynamics facilitate fast reconnection, the reconnection rate is determined by the bulk ion dynamics. The out-flow speed at the ends of the current sheet scales with the Alfvén speed, as shown in panel d) of Fig. 1.14, further confirming the validity of Parker's diffusion region model.

While the specific electron dynamics have been shown to have no direct impact the reconnection rate in tearing-mode reconnection, it is still of importance to determine how the reconnection electric field is generated as this represents the mechanism that breaks the frozen-in condition. Using particle velocity and position data obtained from a PIC simulation of tearing-mode reconnection setup, it was established that the term in the generalised Ohm's law that sustains the out-of-plain electric field at the X-point

in the tearing-mode case corresponds to the divergence of the off-diagonal electron-pressure tensor components as shown by Hesse et al [60] as well as Pritchett [61]. Here the pressure tensor at a given grid cell of coordinates (i,j) is determined by the cell's particle distribution function, $f(r, v, t)$, such that

$$P_{ij} = m_e \int dv(v_i - \langle v_i \rangle)(v_j - \langle v_j \rangle) f. \tag{1.63}$$

This was confirmed in several other studies of tearing-reconnection, as well as in X-point collapse by Tsiklauri and Haruki [62].

Furthermore, the quadrupolar magnetic field predicted Sonnerup was also observed in simulations of collisionless reconnection, first by Mandt in 1994 using a hybrid code, simulating converging flux bundles [63], and later in the Harris current sheet case in several of the GEM simulations, including Hall-MHD, as well as in a PIC simulation of X-point collapse by Tsiklauri and Haruki [64]. Again, the universality of this result for all simulation models that account for the Hall-effect further substantiates the validity of these models and the importance of collisionless effects in reconnection modelling. These simulated results were later confirmed in a physical reconnection experiment using the Magnetic Reconnection Experiment (MRX) [65] as well as in Cluster missions in the Earth's magneto-tail [32, 66, 67], confirming the applicability of 2.5D reconnection models and establishing the quadrupolar magnetic field as usable identifier of magnetic reconnection events in nature.

1.3.2.5 Contemporary 2.5D Collisionless Modelling

Results such as those of the GEM challenge, and their physical confirmation, present a basis upon which many current simulational efforts are based, and as such the vast majority of 2.5D simulational studies use tearing-mode reconnection setups.

While the early collisionless reconnection studies confirmed Parker's relation of the dimensions of the diffusion region and the reconnection rate (Eqn. (1.45)) and proved an independence of the reconnection rate on the electron physics, the shape of the diffusion region is still an active topic of research. In Ref. [68] it was shown that in PIC simulations of tearing-mode reconnection the diffusion region length stabilises on a fixed length, regardless of system size or boundary conditions, reaching length scales up to the order of $10c\omega_{pi}^{-1}$. However, as shown in Ref. [69], while reconnection rates are comparable, the length of the diffusion region in a Hall-MHD simulation of tearing-mode reconnection is an order of magnitude smaller than in an equivalent PIC simulation. This discrepancy underlines the need for models that accurately take account of electron dynamics and shows that the length of the diffusion region can not be determined by MHD based

considerations alone. The nature of the scaling of the diffusion region length remains an open question (see Ref. [70]). Furthermore, as demonstrated in the GEM challenge, the reconnection electric field across the width of the diffusion region is maintained by the divergence of the electron pressure tensor near the X-point and electron inertia at the edge of the diffusion region (see Ref. [60, 61]). Accordingly, the width of the diffusion region is partially determined by the electron inertial length , as is consistent with simulation results (see Fig. 1.14). However, a study comparing the diffusion region width measured in the MRX reconnection experiment and a corresponding PIC simulation study found a mismatch in the results [71], showing distinctly different scalings in both cases. Accounting for this discrepancy and the development of consistent scaling laws, such as that by Tsiklauri [72] and Nakumera et al. [73], is an active research challenge.

Although it was consistently shown that the term breaking the frozen-in condition in tearing-mode reconnection (as well as in X-point collapse) is the divergence of the electron pressure tensor, it has been shown that modifying the standard tearing-mode setup can lead to significant changes in the electron dynamics. This has been established by extending the established simulation framework through the addition of out-of-plane magnetic fields, in-plane shear plasma flows, asymmetric setups, and the inclusion of relativistic effects. The addition of an out-of-plane magnetic was consistently shown to delay the onset of reconnection (see Ref. [74–76]). Further, for increasing guide-fields, an increase in the contribution from electron inertia to the out-of-plane electric field adjacent to the X-point was observed, as well as a spatial compression of the region dominated by the divergence of the electron pressure tensor (see Ref. [77, 78]), thus altering the reconnection dynamics. Further, the inclusion of guide-fields has also been shown to play a role in the generation of electron vortices during reconnection (see Ref. [79]). Similarly, it was shown that when introducing a shear plasma flow along the diffusion region, the reconnection rate could be significantly decreased for flows below the Alfvén speed (see Ref. [80]), and increased for flows above the Alfvén speed (see Ref. [38, 81]), due to a shift in the reconnection instability. In the case of relativistic plasmas (see Ref. [82, 83]) electron dynamics in the diffusion region could be altered to the point that the inertial term replaced the divergence of the pressure tensor at the X-point, presenting a shift from the previously established dynamics. In collisionless simulations using an initial reconnection setup with an asymmetric density profile (see Ref. [84, 85]) it was shown that the inflow stagnation point into the diffusion region did no longer match the location of the magnetic X-point and an entirely new electric field in the diffusion region emerges, coined the Larmor electric field. By studying these modifications to the standard setup, new parameter spaces are explored, aiding the goal of developing models that contain realistic physical conditions that are compatible with observable reconnection events.

When simulating large enough system sizes in a tearing-mode reconnection setup, with an initial perturbation of a small enough wavelength, multiple reconnection sites can emerge, creating magnetic islands. The magnetic islands in turn may be pushed together as they increase in size and coalesce, leading to a different type of reconnection within the tearing sheet (see Ref. [86–88]). Areas of island generation have been shown to exhibit distinct modes of electron acceleration and may play a role in the generation of energetic particles in solar flares (see Ref. [89, 90]). Further, if an initial diffusion region grows long enough, random pertubations can result in secondary reconnection sites within the reconnection current sheet. Shibata in 2001 [91] proposed that coronal magnetic fields reconnect through a fractal structure where large scale tearing leads to sheet thinning and a Sweet-Parker type diffusion region, forming secondary tearing, further sheet thinning and so and so forth, until electron inertial scales are reached (see Fig. 1.15). At this point, numerical simulations and observations only provide indirect evidence for this model of reconnection (see Ref. [92]). On the other hand, a recent theoretical framework proposes the treatment of multiple reconnection sites in a steady state Sweet-Parker-like reconnection model, i.e. reconnection via the the plasmoid instability (see Ref. [93]). In this analysis a Sweet-Parker reconnection sheet is made up by a chain of plasmoids that mediate reconnection and expell plasma through the width of the sheet, giving the potential for fast reconnection under flaring parameters. However, as summarised in Ref. [94], results relating to this framework are still in their infancy.

Regardless of the nature of the large scale magnetic fields involved in reconnection, there still remains a need for a thorough understanding of the processes at the electron and ion-inertial scales that allow reconnection to occur. The results presented in this thesis are part of the effort to investigate the nature of magnetic reconnection by exploring the process in new regimes, here in X-point collapse systems with varying magnetic guide-fields, system sizes, boundary conditions, ion masses and different geometric dimensions (2.5D and 3D), in particular with regards to the electron and ion dynamics. Each of the following three chapters will elaborate on the particular area of contemporary reconnection physics that is being addressed.

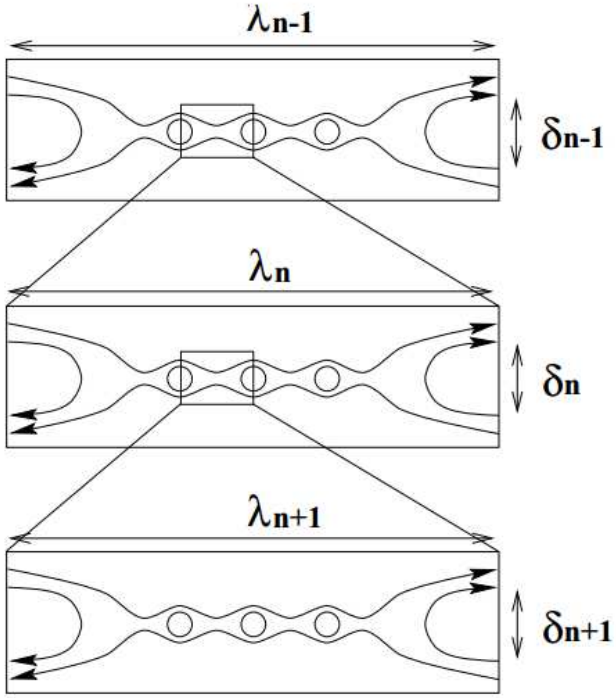

FIGURE 1.15: From [91], showing Shibata's model of fractal reconnection of magnetic fields.

1.4 Magnetic Reconnection in 3D

1.4.1 The nature of 3D reconnection

While 2.5D reconnection modelling is an inexpensive and easily analysable means of studying magnetic reconnection, magnetic structures in nature are inherently three dimensional and can not be expected to be comprehensively represented in this framework. As described in Ref. [95], reconnection in 3D is fundamentally different from its 2.5D counter part. Since magnetic fields are no longer constrained to a 2D plane, the magnetic field-line reconfiguration via reconnection is less limited. Due to the additional degree of freedom, two magnetic field-lines no longer need to break and reconnect in a literal sense but can undergo a transition as shown in Fig. 1.16. Due to the 3rd dimension, the movement of foot-points outside the diffusion region can cause slippage of magnetic field-lines (i.e. movement decoupled form the plasma flow) across a quasi-separatrix without the need of a discontinuity, i.e. without passing through a null point. This immediately tells us that the established measure of the reconnection rate in 2.5D, i.e, the electric field at the X-point, does not necessarily apply in 3D.

Further in Ref. [96] it has been shown that connectivity of flux-tubes (sets of field-lines in 2.5D) is not conserved in a three-dimensional diffusion region, as there generally can not

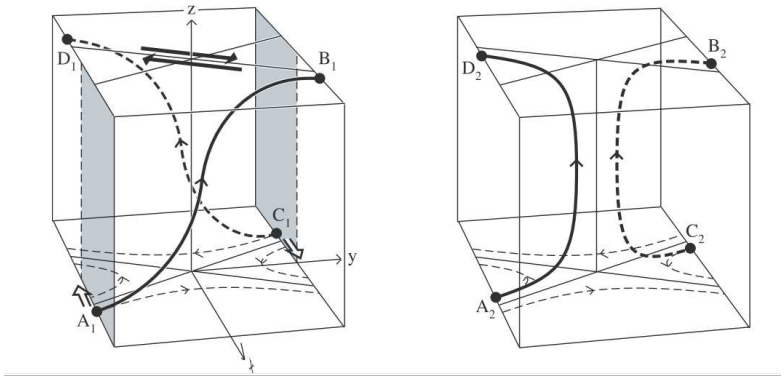

FIGURE 1.16: From [96], showing in panel a) to b) the slippage of a magnetic field line through a three-dimensional diffusion region. As shown, due to the foot-points of the field-line outisde the diffusion region (i.e. B_1 to D_2 and D_1 to B_2), constituting a reconfiguration of the magnetic field without a discontinuity.

exist a field-line velocity that allows for flux conservation. This can be demonstrated by the following analysis: In 2.5D the motion of magnetic-field lines can be described by a flux-conserving velocity field $\mathbf{w}$. Outside the diffusion region $\mathbf{w}$ is equal to the electron-flow velocity as flux is frozen into the plasma. According to Gauss's law magnetic field lines in the diffusion region can not be broken and move through the plane at a velocity such that every inflowing 2D flux-tube (i.e. the space between two field-lines) corresponds to one out-flowing 2D flux-tube. Assuming a flux conserving velocity, $\mathbf{w}$, exists in a 3D diffusion region, we obtain the relation

$$\frac{\partial \mathbf{B}}{\partial t} = \nabla \times (\mathbf{w} \times \mathbf{B}). \tag{1.64}$$

(In the 2.5D case it can be shown that this equation is satisfied everywhere apart from the X-point, where $\mathbf{w}$ tends to a singularity.) By substituting Faraday's law and uncurling the equation one obtains

$$\mathbf{E} = \mathbf{w} \times \mathbf{B} + \nabla F, \tag{1.65}$$

where F is an arbitrary differentiable scalar function. The dot product of Eqn. 1.65 and the magnetic field eliminates the velocity term, giving

$$\mathbf{B} \cdot \nabla F = \mathbf{B} \cdot \mathbf{E}, \tag{1.66}$$

which gives a value of F of the form of the integral of the electric field parallel to the magnetic field, i.e.

$$\Delta F = \int E_{\parallel} ds. \tag{1.67}$$

Outside the diffusion region $\mathbf{w}$ is given by the plasma speed and flux is conserved due to flux freezing and $\mathbf{E} = \mathbf{w} \times \mathbf{B}$. Thus the value of ΔF outside the diffusion region is zero and F on the edge of the diffusion region is fixed. However, for an arbitrary

3D diffusion region with a magnetic field line entering at point A and exiting at point B, where the function F has values F_A and F_B respectively (see Fig. 1.17), there is no limit on the component of the magnetic field parallel to the electric field. As such, generally the integral in Eqn. 1.67 along the field-line is non-zero and $F_A \neq F_B$. This is a contradiction and shows that a flux conserving velocity $\mathbf{w}$ does not generally exist in 3D reconnection. The implication of this result is that the established diffusion region dynamics observed in 2.5D can not be assumed to be found in 3D; there is no requirement for null-points and flux-tube structure is not generally preserved. These factors have to be considered when modelling reconnection in 3D.

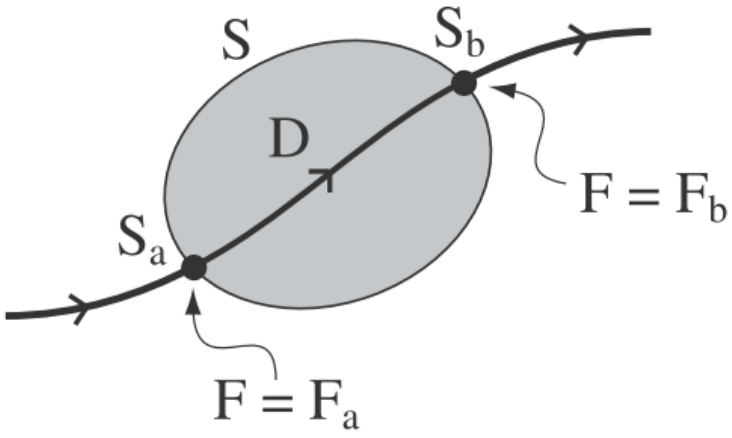

FIGURE 1.17: From [96], showing in grey a diffusion region, connecting two values of F at its surface.

Based on this analysis, and the possibility of magnetic field-line slippage, in 3D reconnection, different physical regimes can apply, constituting different types of diffusion regions. These can be broken down into reconnection with/without a flux-conserving velocity (w) and reconnection with/without a parallel electric field, as summated in Fig. 1.18.

1.4.2 Resistive/Analytical modelling of 3D reconnection

There have been many efforts to study numerically 3D reconnection in resistive MHD simulations as well as kinematic models. Two relevant models for this study are fan reconnection [97, 98] and separator reconnection [99], which allow the investigation of reconnection over 3D null-points (see Fig. 1.19). Furthermore, in an effort to gain an insight into coronal reconnection, simulations of tethered magnetic flux-tubes have been carried out, sometimes with additional twisting [100], resembling observed coronal structures. These studies have demonstrated the likely evolution of current-sheets and magnetic-field structures in uniquely 3D setups. Further, through the inclusion of test

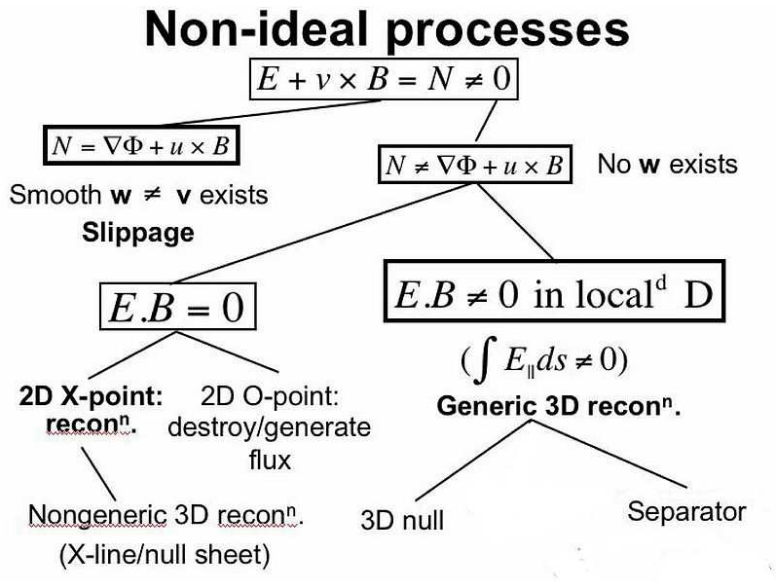

FIGURE 1.18: From [41], showing the distinct regimes of magnetic reconnection in 3D.

particles, i.e. simulation particles that are accelerated by fields without affecting them, the energetics of 3D reconnection has been tested and examples of super-thermal particle acceleration have been established. However, while these studies are promising, they are lacking in their physical reliability in the same way as the resistive 2.5D studies described in section 1.3.1 and rely on anomalous resistivity or analytical extensions to function. Hence, a collisionless, fully kinetic framework is required, which can be accomplished by extending collisionless 2.5D simulations of magnetic reconnection into the 3rd spatial dimension.

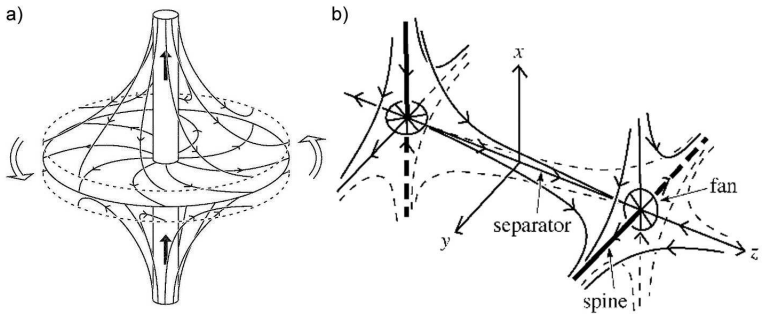

FIGURE 1.19: From [41], showing magnetic field geometries for fan-reconnection in panel a) and separator reconnection in panel b).

1.4.3 Particle In Cell modelling of 3D Reconnection

Pritchett in 2001 extended his PIC simulation of the GEM challenge reconnection setup into the third dimension [101]. Similarly, also in 2001, Tanaka conducted a 3D PIC study of merging flux-bundles [48]. On the time and spatial scales considered in these

simulations, reconnection proceeded in much the same way as in the 2.5D case; current-sheets form in a similar fashion, elongated along the third direction. Only small changes in flux-conversion rate and particle temperature were observed, indicating that despite the possibility of alternative reconnection modes taking hold, reconnection progressed with $\mathbf{E} \cdot \mathbf{B} \approx 0$. In Ref. [74], a GEM challenge-like setup with a guide-field in the third spatial direction was studied in 3D and it was shown that the additional dimension allowed for the generation of Langmuir waves perpendicular to the reconnection plane, adding to the parallel electric field. Later, in one of the most computationally extensive numerical simulation efforts of 3D reconnection (see Refs. [102, 103]) the role of turbulence in three-dimensional reconnection was investigated and it was shown that the emergence of random reconnection sites results in the formation of flux-ropes, proving the correspondence between 2D plasmoids and 3D flux-rope structures. Further, the study demonstrated that the presence of a large enough guide-field results in a split current-sheet which aligns with the magnetic field as well as oblique flux-tubes (see Fig. 1.20). The latter is unique to the 3D geometry case (as will be addressed further in Chapter 4). Remarkably, flux conversion and the width of the diffusion region was not drastically altered from the 2.5D case. Many other 3D PIC studies have been devised, testing features such as particle acceleration [104] and changes in particle distribution functions [105], and have led to a greater understanding of the importance of the inclusion of 3D effects in the reconnection process. The results presented in Chapter 4 of this thesis contribute to this effort.

1.5 X-point Collapse

Dungey's original study of 1953 [1] was the first to introduce the concept of magnetic reconnection at an X-point and to illustrate the reconnection mechanism now referred to as X-point collapse. A more thorough analysis of this instability in X-point magnetic fields was given by Chapman and Kendall in 1963 [106]. X-point collapse is distinguishable as a reconnection setup by its geometry, as illustrated in Ref. [42], chapter 2.1. While in tearing-mode reconnection the initial magnetic field corresponds to a simple gradient in magnetic field strength, X-point geometry implies a more complex initiation mechanism, such as the coalescence of two magnetic structures (e. g. magnetic islands) advected towards each other (see Ref. [63]).

In a X-point collapse set-up, field lines are of the shape of contracted rectangular hyperbolas, with the field strength decreasing towards the midpoint i.e. the X-point. This set-up, for a two-dimensional grid centred on the origin, can be defined most simply as

$$B_x = y, B_y = \alpha^2 x, \tag{1.68}$$

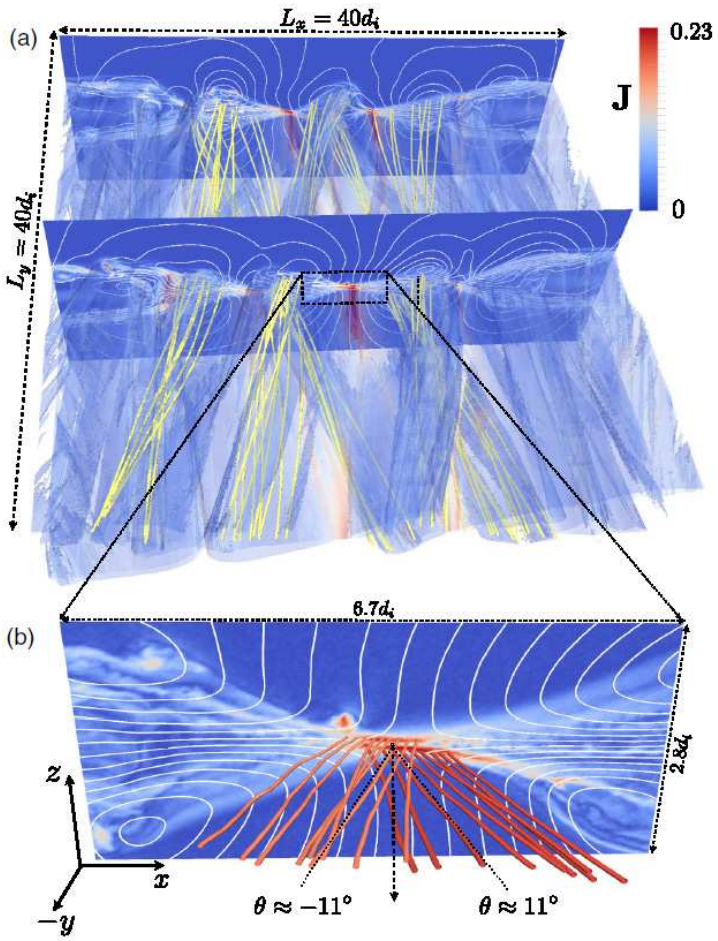

FIGURE 1.20: Simulation results from [103], showing in panel a) current density as indicated by the colour bar, as well as sample magnetic field-lines in yellow and contours of ion in-plane velocity. In panel b) oblique angles of current-sheets are indicated.

and a corresponding out-of-plane current, based on Ampère's law, of

$$j_z = \frac{\alpha^2 - 1}{\mu}. \tag{1.69}$$

Here, α represents the stress parameter, which effectively corresponds to the magnitude of the initial advective force that perturbs the X-point from equilibrium and initiates the collapse. α being greater or smaller than 1 corresponds to a contraction along the x or y axis respectively, and results in an inwards $j \times B$ force on the plasma along the same axis. Field lines are then dragged along by the plasma, further increasing the contraction and thus the current, leading to greater inwards $j \times B$ force. A larger value of α results in a greater initial contraction and thus a faster evolution of the system.

By allowing reconnection to occur, a current sheet forms at the centre of the magnetic structure. Works by Syrovatsky [107, 108] explored the explosive unstable nature of an X-point magnetic configuration and the resulting formation of a current sheet which, in

the MHD regime, was shown to tend to a singularity. These results stood in contrast to Petschek's solution of a steady shock-mediated reconnection dynamic, where the shape of the external field is conserved, and were substantiated by a MHD simulation study by Biskamp in 1986 [45].

Green in 1965 [109] proposed an equation describing the deformation of an X-point magnetic field during current sheet formation. By assuming a vanishing current outside the current sheet, both ∇B and $\nabla \times B$ can be set to zero. The resulting differential equations can be solved by a single analytical solution, given by

$$B_y - iB_x = (z^2 + L^2)^{1/2}, \tag{1.70}$$

where L represents the half-length of the current sheet, and the complex function $z = x + iy$ ranges from $-iL$ to iL. Syrovatsky and Somov in 1976 [110] extended this model by effectively allowing the current sheet to extend beyond the magnetic separatrix (as shown in Fig. 1.21), by an amount of $L - a$, as given by the equation

$$B_y - iB_x = \frac{(z^2 + a^2)}{(z^2 + L^2)^{1/2}}. \tag{1.71}$$

This model implies that reversed current spikes emerge at the edges of the current sheet, which was also shown to be the case in Biskamp's simulation (see Ref. [45]), as well as in a MHD simulation of X-point collapse (see Ref. [111]).

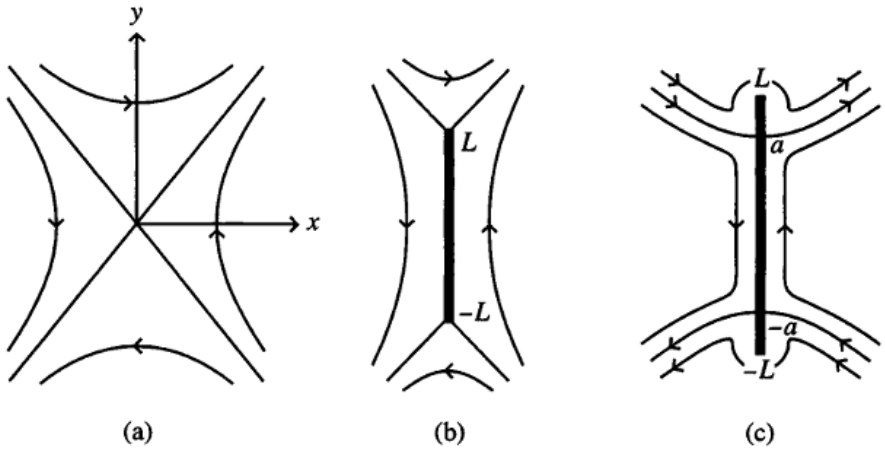

FIGURE 1.21: From [42], showing a sketch of the collapse of an X-point magnetic configuration (see (a)) to a solution given by Eqn. (1.70) in (b) and Eqn. (1.71) in (c).

Furthermore, a theoretical analysis of X-point collapse, in an isolated system, was carried out by Craig and McClymont (see Ref. [112]), demonstrating the cyclic nature of reconnection in a perturbed X-point configuration. Here it was demonstrated that a

perturbed X-point field would undergo consecutive stages of forming vertical and horizontal current-sheets, i.e. reversing the direction of reconnection flow, until a potential stage is reached. This result was further confirmed in a MHD simulation (see Ref. [113]), where shock formation was also accounted for. As explained in Ref. [42], chapter 7.1.1, Craig and McClymont further demonstrated that in the purely resistive case, for a sufficiently thin current sheet to form, allowing for fast-reconnection to be possible in an X-point collapse, the following condition must generally be satisfied,

$$\beta \lesssim \left(\frac{\eta}{V_A L}\right)^{0.565}, \tag{1.72}$$

where β represents the ratio of the thermal pressure to the magnetic pressure in the system. If this condition is not satisfied, the collapse of the X-point will be counteracted by the plasma pressure and choked off. In the case of solar plasmas the right hand side of this condition is of the order of 10^{-8}, implying that $\beta \lesssim 10^{-8}$, which is much smaller than values based on observation. Hence, kinetic effects play a decisive role if reconnection is to be fast. As shown in PIC simulations by Tsiklauri and Haruki [62, 64] fast reconnection was indeed achieved in this regime.

The works presented in this thesis aim to further extend the works of Tsiklauri and Haruki and the study of X-point collapse as a reconnection model.

Chapter 2

The effect of guide-field and boundary conditions on collisionless magnetic reconnection in a stressed X-point collapse

In this chapter, works of D. Tsiklauri, T. Haruki, Phys. of Plasmas, 15, 102902 (2008) and D. Tsiklauri and T. Haruki, Phys. of Plasmas, 14, 112905, (2007) are extended by inclusion of the out-of-plane magnetic (guide) field. In particular, magnetic reconnection during collisionless, stressed X-point collapse for varying out-of-plane guide-fields is studied using a kinetic, 2.5D, fully electromagnetic, relativistic particle-in-cell numerical code. For zero guide-field, cases of both open and closed boundary conditions are investigated, where magnetic flux and particles are lost and conserved respectively. It is found that reconnection rates, out-of-plane currents and density in the X-point increase more rapidly and peak sooner in the closed boundary case, but higher values are reached in the open boundary case. The normalized reconnection rate is fast: 0.10-0.25. In the open boundary case it is shown that an increase of guide-field yields later onsets in the reconnection peak rates, while in the closed boundary case initial peak rates occur sooner but are suppressed. The current at the X-point changes similarly with increasing guide-field, however for low guide-fields it increases, giving an optimal value for the guide-field between 0.1 and 0.2 times the in-plane field in both cases. Also, in the open boundary case, it is found that for guide-fields of the order of the in-plane magnetic field, the generation of electron vortices occurs. Possible causes of the vortex generation, based

on the flow of decoupled particles in the diffusion region and localized plasma heating, are discussed. Before peak reconnection onset, oscillations in the out-of-plane electric field at the X-point are found, ranging in frequency from approximately 1 to 2 ω_{pe} and coinciding with oscillatory reconnection. These oscillations are found to be part of a larger wave pattern in the simulation domain. Mapping the out-of-plane electric field along the central lines of the domain over time and applying a 2D Fourier transform reveals that the waves predominantly correspond to the ordinary and the extraordinary mode and hence may correspond to observable radio waves such as solar radio burst fine structure spikes. It was further discovered that the well known quadrupolar structure in the out-of-plane magnetic field gains four additional regions of opposite magnetic polarity, emerging near the corners of the simulation box, moving towards the X-point. The emerging, outer, magnetic field structure has opposite polarity to the inner quadrupolar structure, leading to an overall octupolar structure. Using Ampère's law and integrating electron and ion currents, defined at grid cells, over the simulation domain, contributions to the out-of-plane magnetic field from electron and ion currents were determined. The emerging regions of opposite magnetic polarity were shown to be the result of ion currents.

2.1 Introduction

Dungey's original work on X-type collapse [1] is the earliest analysis of magnetic reconnection, predating tearing-mode and Sweet-Parker theories, and X-type scenarios are still frequently considered in models of solar flares (see Ref. [2], chapter 10.5.1). Most space and solar plasma simulations of magnetic reconnection predominantly focus on reconnection induced by the tearing-mode instability. Yet, after a Harris type current sheet is disrupted by a tearing instability and magnetic islands and X-points start to form, there are in deed few distinguishable differences between X-point collapse and the well-studied tearing instability. In both cases a stage is reached where X-point symmetry is broken, which means that there is no restoring force and the X-point collapses, resulting in fast reconnection (see Ref. [42], chapter 7.1). Moreover, even the respective causes of the reconnection electric field, as calculated using the generalized Ohm's law, are the same, namely the off-diagonal terms of the divergence of the electron pressure tensor. This was shown in Ref. [62] for the case of X-point collapse and in Ref. [114] for the tearing-mode instability. Equally similar is the quadrupolar structure of the out-of-plane magnetic field at the X-point, caused by the Hall effect (first proposed in Ref. [51] and shown to be critical in fast reconnection in Ref. [63]). This was shown to emerge in the case of X-point collapse in Ref. [64] and in the case of tearing-mode

instability in Ref. [114], as well as in the Magnetic Reconnection Experiment (MRX) [115].

This chapter extends the works of D. Tsiklauri and T. Haruki ([62] and [64]), where X-point collapse was modelled using a fully relativistic 2.5D Particle in Cell (PIC) code, by introducing an uniform out-of-plane magnetic guide-field of varying magnitudes and by comparing the effects of different boundary conditions (details of the code and set-up used are given in 2.2).

The relevance of reconnection with a guide-field in natural reconnection processes is apparent in solar flare models such as that of Hirayama [13], as shown in Fig. 2.1. In this model a rising solar prominence stretches out a current sheet, prone to trigger magnetic reconnection (see Ref. [2], chapter 10.5.1). Here it is clear that the filaments making up the prominence are mostly perpendicular to the plane of the reconnection site (or rather parallel to the current sheet) and thus constitute a guide-field. Similarly guide-fields play a role in reconnection in the magnetotail of the Earth, as demonstrated in Ref. [116].

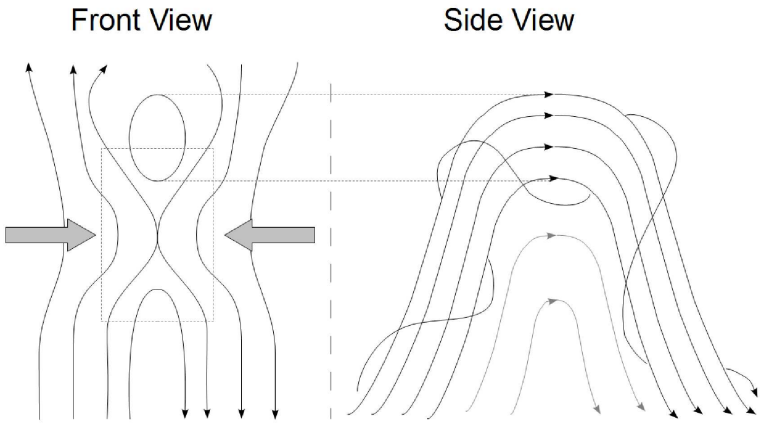

FIGURE 2.1: Adopted from [2], p. 437, based on [13], showing a snap shot of Hirayama's model of solar flares, indicating reconnection site (front view) and guide-field (side view).

There have been several other studies into the matter of magnetic reconnection in the case of a guide-field, with different set-ups, including computational studies by Horiuchi et al. [75], Pritchett et al. [74, 117] and Fermo et al. [79], as well as experimental studies using the MRX [76, 115] and the Versatile Toroidal Facility (VTF) [118, 119]. While the field configurations in these studies were distinctly different from those presented here, some of their findings are similar, including the delays in onset times of peak reconnection [75, 76] and the increase in out-of-plane current along one pair of separatrix arms [74, 75] (see section 2.3.2.1). Further, electron vortices were shown to emerge at the X-point for guide fields approximately equal to the in-plane field, similar to vortex

formation simulated in Ref. [79] (see section 2.3.2.2). These vortices appear singularly at the X-point, as opposed to in multiples along the X-line, and thus appear distinctly different from vortices observed in Ref. [117]. While (as shown in Ref. [79] and [117]) vortices were found previously in similar numerical set-ups, we find for the first time that imposing a guide-field can also lead to electron vortex formation in X-point Collapse. Albeit, this also underscores the similarities between X-point collapse and tearing-mode set-ups and that more attention needs to be paid to the former.

As discussed in Ref. [120] page 91-94, the generation of electromagnetic waves plays a significant role in Hall reconnection scenarios. The generation of whistler and Alfvén waves during reconnection was simulated in Ref. [121] and demonstrated experimentally at the VTF [118]. Further, electro-static waves were detected at the X-point in a VTF experiment during reconnection in Ref. [119]. As shown in section 2.3.3, both electrostatic and electromagnetic waves are produced directly preceding reconnection onset, with the electromagnetic waves being in the radio frequency regime. These could be similar to radiation from events such as Type II precursors (first discovered in Ref. [122]), which are known to release radio waves prior to solar flares and thus prior to reconnection in the Hirayama model.

2.2 Simulation model

2.2.1 Stressed X-point Collapse Reconnection Model

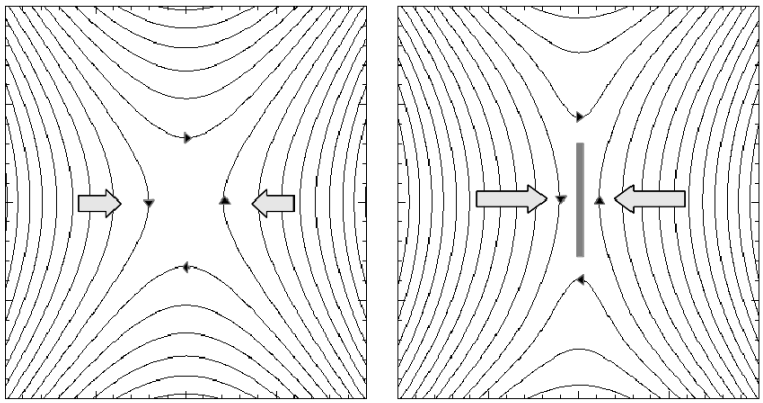

FIGURE 2.2: Magnetic field line configuration at the start of the simulation (left) and at the peak of the reconnection (right). Directions of field lines are indicated. Arrows indicate the acceleration of the field lines due to the $\mathbf{J} \times \mathbf{B}$ force. The grey vertical strip indicates the current sheet.

Following the description of X-point collapse in section 1.5, the left panel of Fig. 2.2 shows the initial set-up of the in-plane magnetic field used in this study. This is mathematically described by the following expressions

$$B_x = \frac{B_0}{L} y, \quad B_y = \frac{B_0}{L} \alpha^2 x, \tag{2.1}$$

where B_0 is magnetic field intensity at the distance L from the X-point for $\alpha = 1.0$, L is the global external length-scale of reconnection, and α is the stress parameter (see e.g. chapter 2.1 in Ref. [120]). In addition a uniform current is imposed at time $t = 0$ in the z-direction, corresponding to the curl of the magnetic field, such that Ampère's law is satisfied

$$j_z = \frac{B_0}{\mu_0 L}(\alpha^2 - 1). \tag{2.2}$$

The configuration above was simulated and analysed in Ref. [64]. In this scenario the initial stress in the field leads to a $\mathbf{J} \times \mathbf{B}$ force that pushes the field lines horizontally inwards. This serves to increase the initial imbalance, which in turn increases the inwards force and the field collapses. Due to the frozen-in condition, this leads to a build up of plasma near the X-point and eventually to the formation of a diffusion region, accompanied by a current sheet as shown in the right panel of Fig. 2.2. The term in the generalized Ohm's law which corresponds to the breaking mechanism of the frozen in condition was shown to be the off-diagonal terms of the electron pressure tensor divergence, due to electron meandering motion (see Ref. [62]).

The new effect introduced in this study is an out-of-plane magnetic guide-field of different intensities. The strengths of the guide-field were chosen to be fractions of the maximum field amplitude within the plane, B_P, i.e.

$$B_{Z0} = (n/10) B_0 \sqrt{1 + \alpha^2} = (n/10) B_P, \tag{2.3}$$

where n is an integer ranging from 1 to 10.

2.2.2 PIC Simulation Code

The simulation code used here is a 2.5D relativistic and fully electromagnetic PIC code, as developed by the EPOCH collaboration [123] and is based on the original PSC code by Hartmut Ruhl [124], employing the the Villasenor and Buneman scheme [125] to update simulation parameters (minor modifications were made in this study to allow for closed boundary conditions). EPOCH uses an explicit second-order fields-particle

solver (as described in Appendix A), is optimised for parallel computing on multiple processors, and accepts simulation parameters via a customisable input deck. The size of the grid cells in both x and y where set to the Debye length, i.e. below the limit set by the finite grid instability, such that

$$\Delta x = \Delta y = \lambda_D = \sqrt{k_B T_e \epsilon_0 / n_e e^2}. \tag{2.4}$$

The timestep in this simulation was determined by the simulation code and set as

$$dt = \frac{\lambda_D}{c\sqrt{2}}, \tag{2.5}$$

i.e. sufficient to resolve the propagation of both light and Langmuir waves, i.e. $c\Delta t < \Delta x$ and $\omega_{pe}\Delta t < 2$.

The parameters in the simulation were chosen such that temperature, particle densities and magnetic fields corresponded to observed values for coronal flaring loops [2, 18]. Observational studies have found flaring temperatures to be in the range of 10^6K to 10^8K, number densities of electrons of $10^{15}m^{-3}$ to $10^{17}m^{-3}$ and magnetic field strengths of the order of 0.01 Tesla. Accordingly, the number density of both electrons and ions in the simulation domain, n_e and n_p, was set to $10^{16}m^{-2}$. Matching conditions in simulations by Tsiklauri and Haruki [64], the magnetic field and temperatures were defined such that $\omega_{pe} = \omega_{ce}$, where ω_{ce} is the electron cyclotron frequency, the characteristic Alfvén speed, $v_{ae0} = 0.1c$ and $v_{Te} = v_{ae0}$, where v_{Te} is the electron thermal velocity. Hence the temperature of electrons and protons, T_e and T_p, was set to 6.0×10^7K, and value of B_0 was set as 0.03207 T. The proton mass was set to 100 times the electron mass, i.e. $m_p = 100m_e$, to speed up the code. These parameters give the characteristic length scales of the plasma, in terms of the Debye length ($\lambda_D = 0.0053454m$) as follows: The electron cyclotron radius, $r_{ce} = \lambda_D$; the electron inertial length (skin depth), $c/\omega_{pe} = 10\lambda_D$; the ion inertial length, $c/\omega_{pi} = 100\lambda_D$ and the ion sound gyro radius, $\sqrt{T_e/m_i}/\omega_{ci} = 10\lambda_D$.

While the length-scales of flaring processes range from 10^6m to 10^8m, PIC simulations using today's technology do not have the capacity to simulate plasma over such vast scales and a reduced area is considered, focussed on the reconnection processes. The simulation used a grid of 400×400 cells, which thus gave the simulation domain a length of $2L = 400\lambda_D = 2.1382$ m, corresponding to $4.0208c/\omega_{pi}$. While much smaller than a coronal magnetic field structure, it contains within itself the ion inertial length, thus allowing for two-fluid effects, as well as the other relevant length scales. The code used 500 particles per species per cell and thus a total 1.6×10^8 particles in total. While the simulation in Ref. [64] used only 100 particles per cell, which is sufficient to accurately resolve electromagnetic field dynamics, it was found that a greater number was needed

to accurately resolve particle dynamics, particularly with regards to the discovery of the electron vortex (see section 2.3.2.2). Convergence tests showed that results converged with those at 1000 particles per cell. The initial stress parameter is set as $\alpha = 1.2$, corresponding to a small initial compression of a X-point magnetic field. In Ref. [64] it was shown that for such an initial compression the system evolved over a period of the order of $200\omega_{pe}^{-1}$, thus allowing for a clear distinction of the time-scales relating to electron effects and the collective dynamics of the system.

2.2.3 Boundary Conditions

The original simulation of Tsiklauri and Haruki (see Ref. [64]) used boundary conditions such that flux at the boundary is conserved. Hence, zero-gradient boundary conditions are imposed both on the electric and magnetic fields in x- and y-directions and the tangential component of electric field was forced to zero, while the normal component of the magnetic field was kept constant. This ensures that magnetic field-lines are fixed on the boundary, whilst also inhibiting loss (or gain) of magnetic flux from the simulation domain. Further, the boundary condition for particles in the simulation was set so that particles are reflected when reaching the boundary. Thus, the the simulation represents an isolated physical system, neither losing nor gaining magnetic or particle flux (we will refer to this as closed boundary conditions).

Here we also consider boundary conditions that allow outflow of electromagnetic flux and particles i.e. where waves or particles travelling past the simulation boundary are removed and no longer affect the simulation (see Ref. [124] chapter 2.4). The routine allowing for the transfer of flux also fixes the mean field tangential to the boundary to its initial value. This effectively corresponds to the initial simulation domain being embedded in a larger X-point collapse setup (we will refer to this as open boundary conditions). Both this and the previous case were investigated, with and without guide-field, such that differences could be established.

Based on simple physical considerations it can be argued that open boundary conditions are more relevant in many astrophysical reconnection scenarios, as for example in the solar flare reconnection model described in Ref. [13], or more generally the space around tearing-unstable X-points, where there is no physical restriction on the motion of field lines and hence particles. On the other hand, closed boundary condition are more relevant to reconnection in confined reconnection scenarios, particularly 'closed-type' experiments (tokamaks, spheromaks etc.) where motion of field lines and particles is restricted (as described in several examples in Ref. [126]), but also natural reconnection events where the motion of foot-points is restricted.

2.3 Simulation Results

2.3.1 Effect of Boundary Conditions

An initial test was carried out for the zero guide-field case, i.e. $B_{Z0} = 0$, showing how the simulation results of the original study [64] vary when applying open instead of closed boundary conditions, as shown in Fig. 2.3. Reconnection electric field, reconnection current and density at the X-point appear to increase more rapidly and peak sooner in the closed boundary case. However, higher values appear to be reached in the open boundary for all three variables, particularly in the reconnection current. Also in the open boundary case, there is a much lesser decline within the simulation time and the characteristic double peak profile in the reconnection electric field in the closed boundary case is not apparent, at least not before $500\omega_{pe}^{-1}$. All of the above observed differences indicate that the change in boundary condition has a significant effect on the reconnection dynamics. By plotting the magnetic flux function (i. e. the z-component of the magnetic vector potential), calculated using the spatial gradients of the magnetic field components and components of E_z, as contours of equal magnitude, at different times in the simulation, these differences in reconnection were shown dynamically (see movie 1 and 2 in [127]).

In both cases, rapid high-amplitude oscillations in the out-of-plane electric field occur immediately before reconnection onset. Plotting contours of the out-of-plane flux-function at the X-point, it was shown that this oscillation corresponds to oscillatory reconnection (see movie 3 in supplementary material [127]), as first demonstrated in Ref. [112]. Further oscillations, with a smaller amplitude, emerge later in the simulation in both cases, but predominantly in the closed case, as shown in the middle panel of Fig. 2.3. As opposed to reconnection in a uni-directionally sheared magnetic field, field lines in X-point collapse reaching the X-point are likely to carry different particle distributions due to their differences in initial geometry, which is a likely factor in the transient nature of the reconnection observed. In the open case, field lines are free to shift on the boundary (see movie 1 in [127]), which may reduce the impact of the geometry, thus reducing the oscillations in the reconnection electric field as shown (these oscillations and the generation of electromagnetic waves preceding reconnection onset will be discussed further in section 2.3.3).

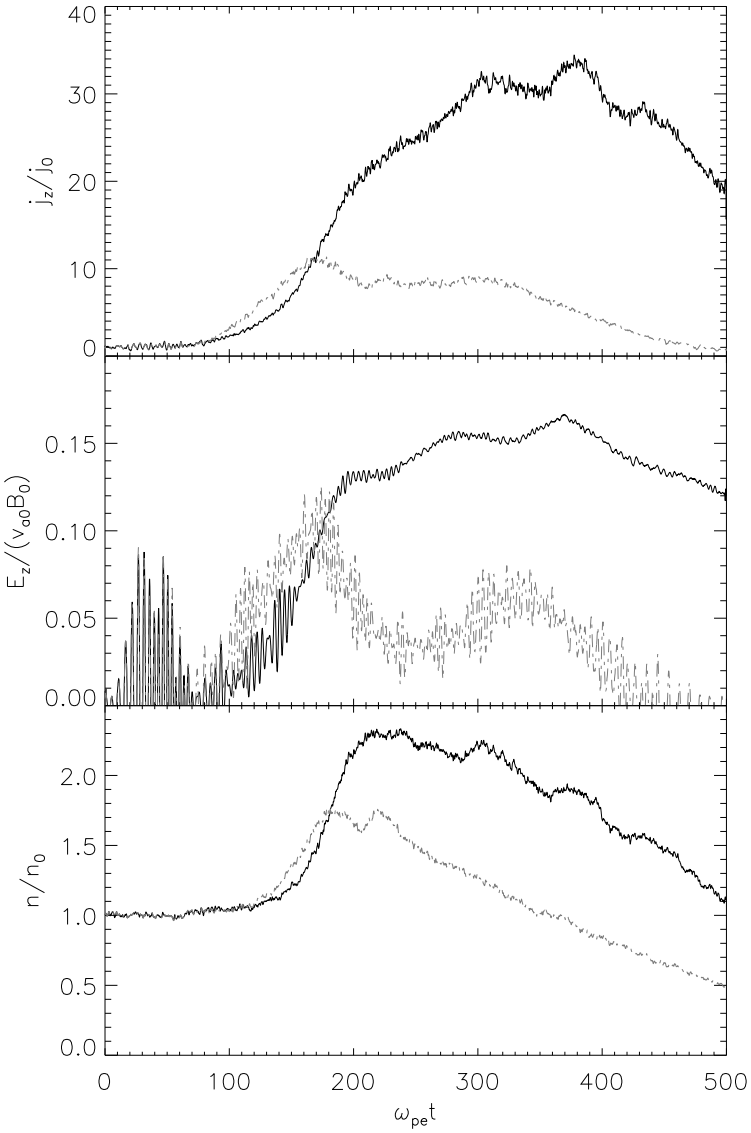

FIGURE 2.3: (top) and (middle) respectively show the reconnection electric field and current at the X-point as a function of time. In black the case for open boundaries is shown, whereas the grey line shows the case for closed boundaries. (Bottom) The particle number density at the X-point, also for both boundary cases. Again, black represents the open boundary case whereas grey represents the closed boundary case.

2.3.2 Effect of Guide-Field

2.3.2.1 Effects on Reconnection Rate and Shape of Current Sheet

The obtained values for reconnection electric field and current for the different strengths of guide-fields as a function of time are shown in Fig. 2.4 for the open boundary case and in Fig. 2.5 for the closed boundary case. In the open boundary case we see a trend of delayed on-set times in the reconnection field. The same is true for the reconnection current, except for $n = 2$ (i.e. $B_{Z0} = 0.2B_P$). In the closed boundary case initial peaks

are reached sooner for greater values of guide-field, but their amplitudes are significantly reduced. Onset times of the secondary peak however are also delayed.

These results are consistent with other reconnection simulations using different set ups, including the 1997 study by Horiuchi and Sato [75]. Here it is argued that the increase in guide-field reduces the orbit associated with the meandering motion of electrons, making them more magnetized and less likely to break the frozen-in condition and thus delaying on-set times. Further, the reduction in reconnection electric field in the closed boundary case is in-line with the findings in Ref. [115], where it is shown that, in the MRX set-up, the reconnection electric field corresponds to that of a Hall MHD simulation and is reduced for greater guide-fields due to a reduction in the Hall-current.

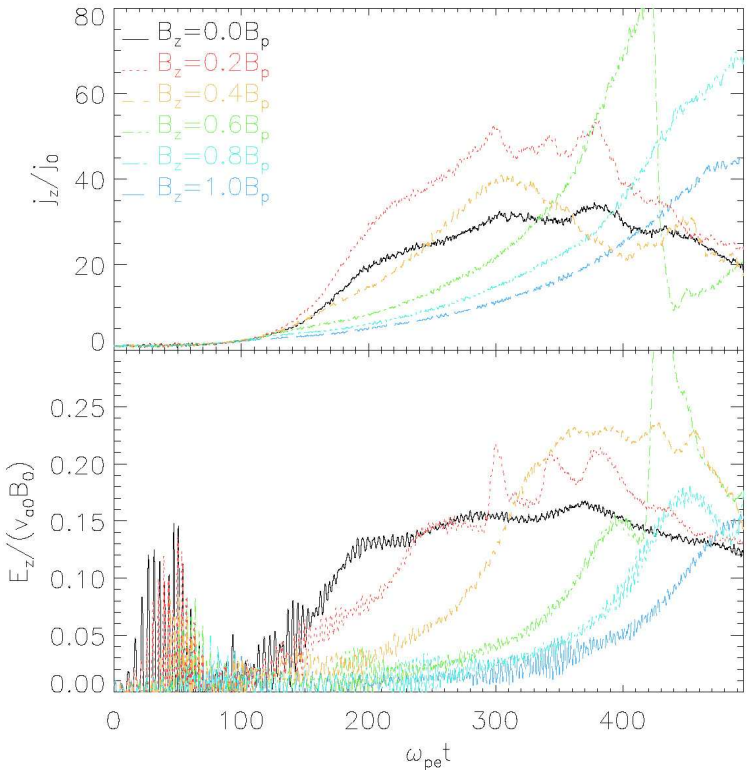

FIGURE 2.4: The reconnection current and electric field over time, for different levels of guide-field as indicated, for open boundary conditions.

At later stages in the open boundary case, the reconnection field for guide-fields of $B_{Z0} = 0.2$ up to $B_{Z0} = 0.6B_P$ tends to significantly exceed that of the zero-guide-field case. Further, we see somewhat chaotic peaks occurring, leading to an exceptionally high peak value at $B_{Z0} = 0.6B_P$. We discuss in section 2.3.2.2 how this particular peak, as well as the peak values for $B_{Z0} = 0.8$ and $B_{Z0} = 1.0B_P$, are linked to the emergence of an electron vortex at the X-point along with a magnetic island. This is of relevance since it has been shown in Ref. [89] that magnetic islands, formed at the X-point, can

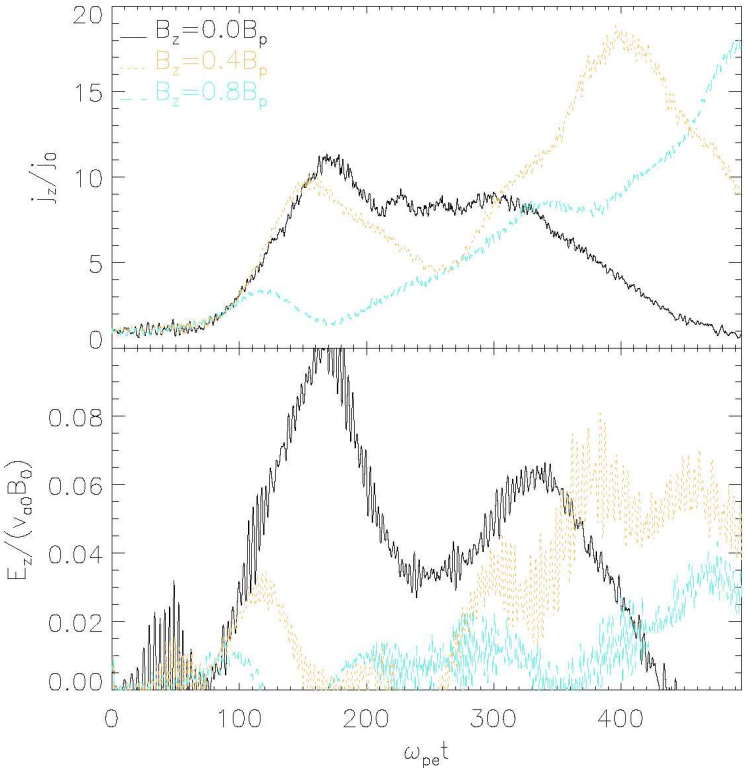

FIGURE 2.5: As in Fig. 2.4 but for the closed boundary case.

have an effect on electron acceleration and lead to an increased out-of-plane current (see specifically the central island in Ref. [89], fig 6(c)).

The increase in reconnection current at $n = 2$ was investigated further by running the simulation with guide-fields ranging from 0 to $0.5B_P$ in steps of $0.05B_P$. It was shown that, for the open boundary case, the initial rate of increase of the reconnection current reached a peak value, giving an "optimal" guide-field strength between $0.1B_P$ and $0.2B_P$. An increase of the reconnection current caused by the introduction of a guide-field, as well as an increase in the current along one pair of separatrix arms, is also observed and discussed in detail in Ref. [74]. It is discussed here how the diversion of particle flows due to the guide-field can result in the confinement of electrons to one of the separatrices, leading to a greater density and thus a greater out-of-plane current.

Fig. 2.6 shows the out-of-plane current in the simulation domain for the open boundary case for three different strengths of guide-field at three different snapshots in time. The plots show that for greater guide-fields onset times are delayed and distinct current sheets take longer to develop (this is shown dynamically in movie 4 in the supplementary material [127]). Also, as discussed in Ref. [74], the introduction of a guide-field appears to lead to the out-of-plane current being intensified along one pair of separatrix arms. At $500.0\omega_{pe}^{-1}$ for $B_{Z0} = 0.8B_P$ a circular area of high out-of-plane current emerges at

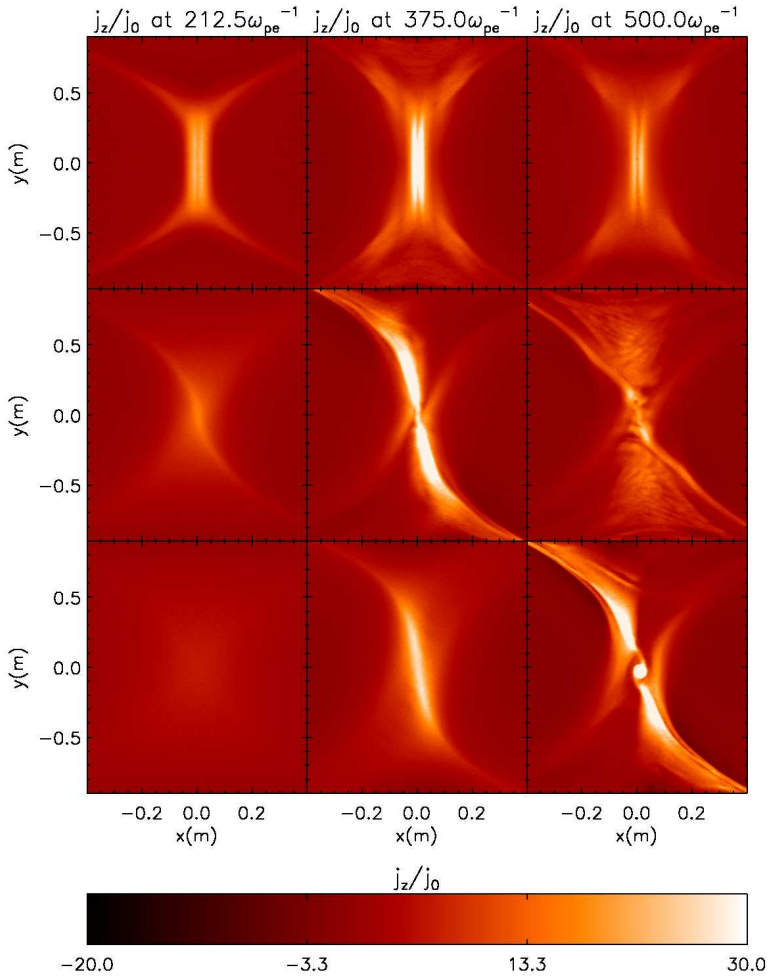

FIGURE 2.6: Out-of-plane current in the open boundary case for different guide-field strengths at different simulation times. The three columns correspond from left to right to simulation times of $212.5\omega_{pe}^{-1}$, $375.0\omega_{pe}^{-1}$ and $500.0\omega_{pe}^{-1}$ respectively. The three rows correspond from top to bottom to guide field strengths of 0.0, $0.4B_P$ and $0.8B_P$ respectively.

the X-point. We show in section 2.3.2.2 that this is correlated with the emergence of a magnetic island, which, as shown in Ref. [89], can cause electron acceleration such that out-of-plane currents are locally increased.

Fig. 2.7 shows the out-of-plane current in the simulation domain for the closed boundary case for the same guide-field strengths, for snapshot times as indicated. While we observe similar results in terms of the strengthening of the current along one pair of separatrix arms and delayed onset-times, there is no indication of spiralling or clustering at the centre of the domain (this is shown dynamically in movie 5 in the supplementary material [127]). Other tests also confirmed that there was no evidence for the formation of vortices within the simulation time. However, for greater strengths of guide-field, the

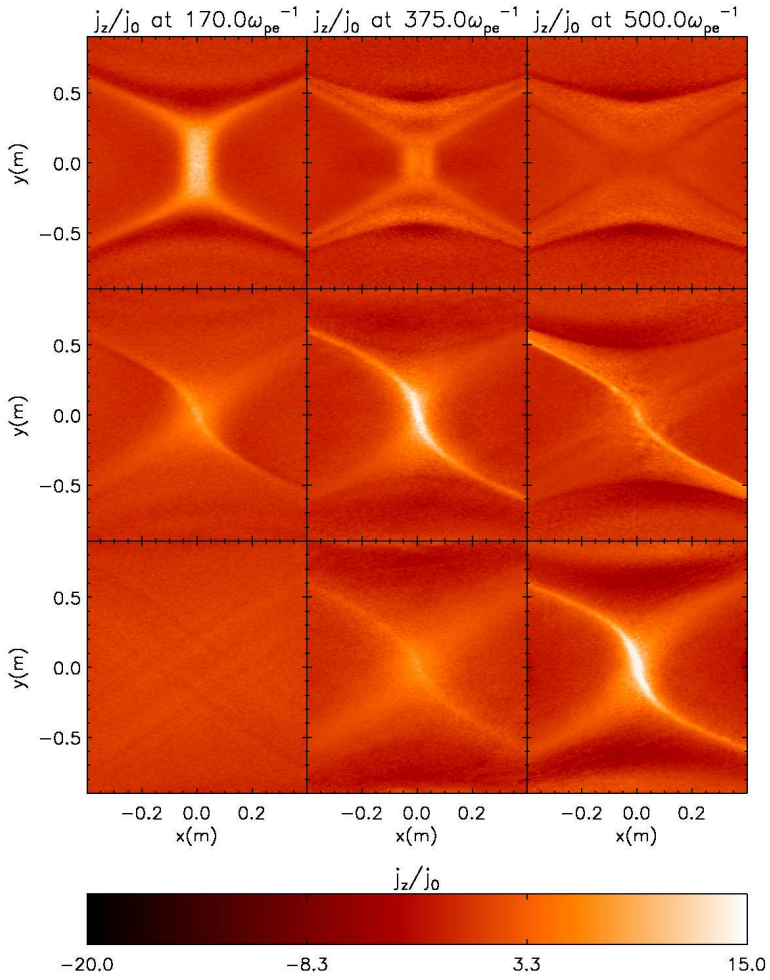

FIGURE 2.7: As in Fig. 2.6 but for closed boundary conditions and with simulation times as stated.

current sheets appeared to be thinning, which is in line with several other reconnection experiments (see Ref. [120] page 96-97).

Further, the introduction of guide-field had a notable effect on the oscillations in the out of-plane-electric field preceding reconnection onset. Fig. 2.8 shows the reconnection electric field for the open boundary case for increasing guide-field strengths, showing a smoothed line to indicate the mean increase of the field. As shown, for greater guide-field, the formation of a wave burst in the initial oscillation is increasingly delayed and the amplitudes reached are increasingly reduced. However, in each case, reconnection onset coincides with the decline of the amplitude of the initial burst. A connection appears to exist between the two events, indicative of the transient nature of reconnection in X-point collapse.

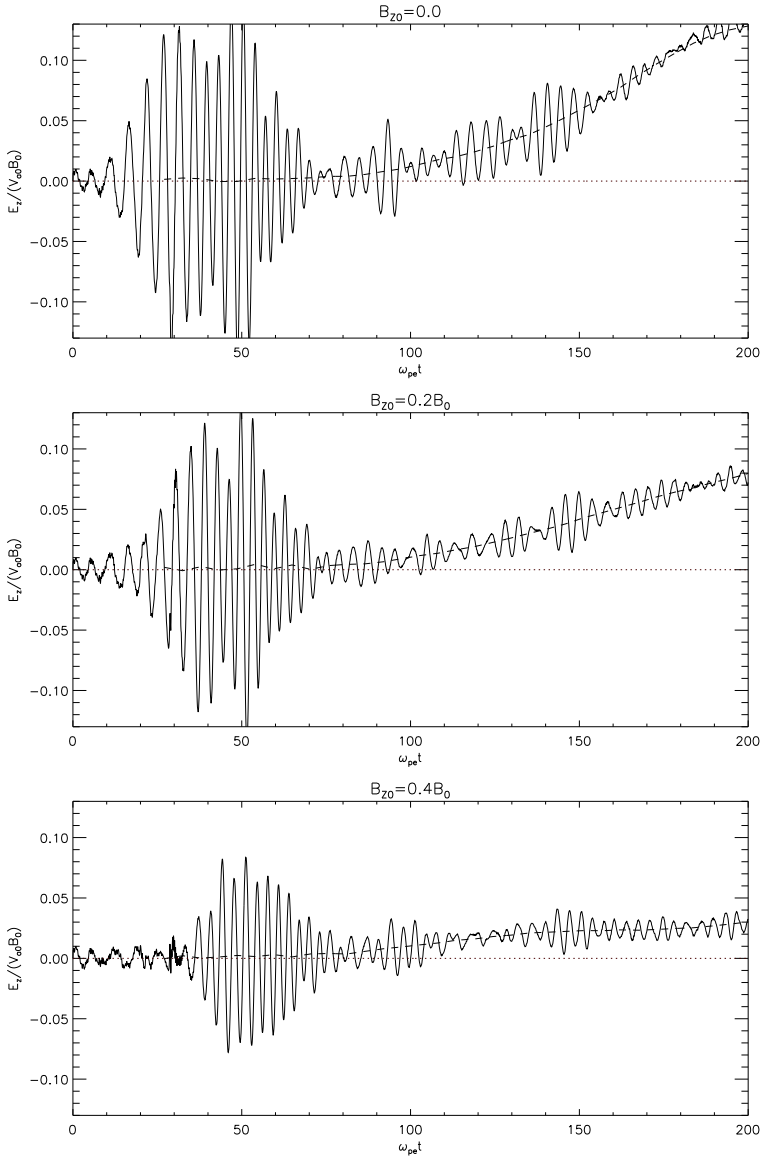

FIGURE 2.8: Out-of-plane electric field at the X-point for guide-fields of 0.0, 0.2 and $0.4B_P$ at the beginning of the simulation in the open boundary case. The dashed line represents the same values, smoothed with a filter width of $30\omega_{pe}^{-1}$, indicating the increase in reconnection electric field following reconnection onset.

2.3.2.2 Vortex generation for high guide-field cases

As pointed out, the anomalous peak in the reconnection electric field and current for a guide-field of $B_{Z0} = 0.6B_P$, as shown in Fig. 2.4, is due to the emergence of vortical motion in the plane of the simulation domain. However, while in this case, the emerging vortex moved along the positive y direction of the domain and dissipated, for the case of $B_{Z0} = 0.8B_P$, the vortex remained more stable and more defined. Fig. 2.9 shows a series of plots relating to the electron vortex that emerges for a guide-field of $B_{Z0} = 0.8B_P$ and that of a case where the guide-field is reversed, i.e. $B_{Z0} = -0.8B_P$, which provides a clue

regarding the nature of the vortex. Further, movie 6 in the supplementary material [127] shows the change in the electron velocity grid for $B_{Z0} = 0.8B_P$, showing the formation of the vortex (note that the film extends further than the end of simulation time used in the previous plots).

Following [120], page 89-92, the quadrupolar structure of the out-of-plane magnetic field that emerges during reconnection of opposing field lines is caused by the decoupled motion of electrons and ions in the dissipation region. This is illustrated in the top panel of Fig. 2.10. Ions (here protons) decouple and cease to move with the field lines sooner than the electrons, leading to current loops which in turn lead to magnetic structures. In a similar fashion, it is argued here that imposing a sufficiently strong guide-field in the diffusion region would impose current loops, which in turn lead to vortical motion of particles.

As discussed in Ref. [120], page 96-101, and shown in Ref. [75] and Ref. [74], the presence of a guide-field in reconnection can lead to a shear flow of electrons along the in-plane magnetic field at the separatrices. This in turn leads to an ion polarization drift across the dissipation region to compensate for the resulting charge imbalance. This was also observed in the results of this study, as demonstrated in the bottom panel of Fig. 2.10. Reversing the guide-field was shown to reverse the motion of electron flow and thus the polarization drift of the protons. Comparing this to the flows in Fig. 2.9 it is clear that the electron flows already undergo the vertical part of the vortex motion. Adding to this the influence of a substantial guide-field, and thus a $j \times B$ force, it is plausible that the guide-field, which is also present at the X-point, becomes a dominant factor in the decoupled motion of the electrons and initiates vortical flows as observed.

An additional consideration is that, as is known for shear flow of plasmas, the Kelvin-Helmholtz instability could play a role in the emergence of the vortex. In Ref. [79] a case is made that current sheets, elongated by the influence of a guide-field, that undergo secondary reconnection are in fact triggered by the Kelvin-Helmholtz instability, and that the emergence of the magnetic islands is due to the emergence of electron vortices. Again, there are significant differences in the simulation set-up used in this study, but it is consistent in the aspect that the vortex observed in this simulation was accompanied by the formation of a magnetic island (see Fig. 2.9). Further, movie 6 in the supplementary materials [127] shows what could be interpreted as secondary vortices, forming after the initial vortex emerged, as would be consistent with Kelvin-Helmholtz vortices.

Further, as described Ref. [128] and demonstrated in Ref. [129], in the 2D electron MHD regime, extended to include pressure effects, vortical flows and corresponding out-of-plane magnetic fields can be induced by localised temperature perturbations. As shown, the growth rate of vorticity in this case corresponds to the electromotive

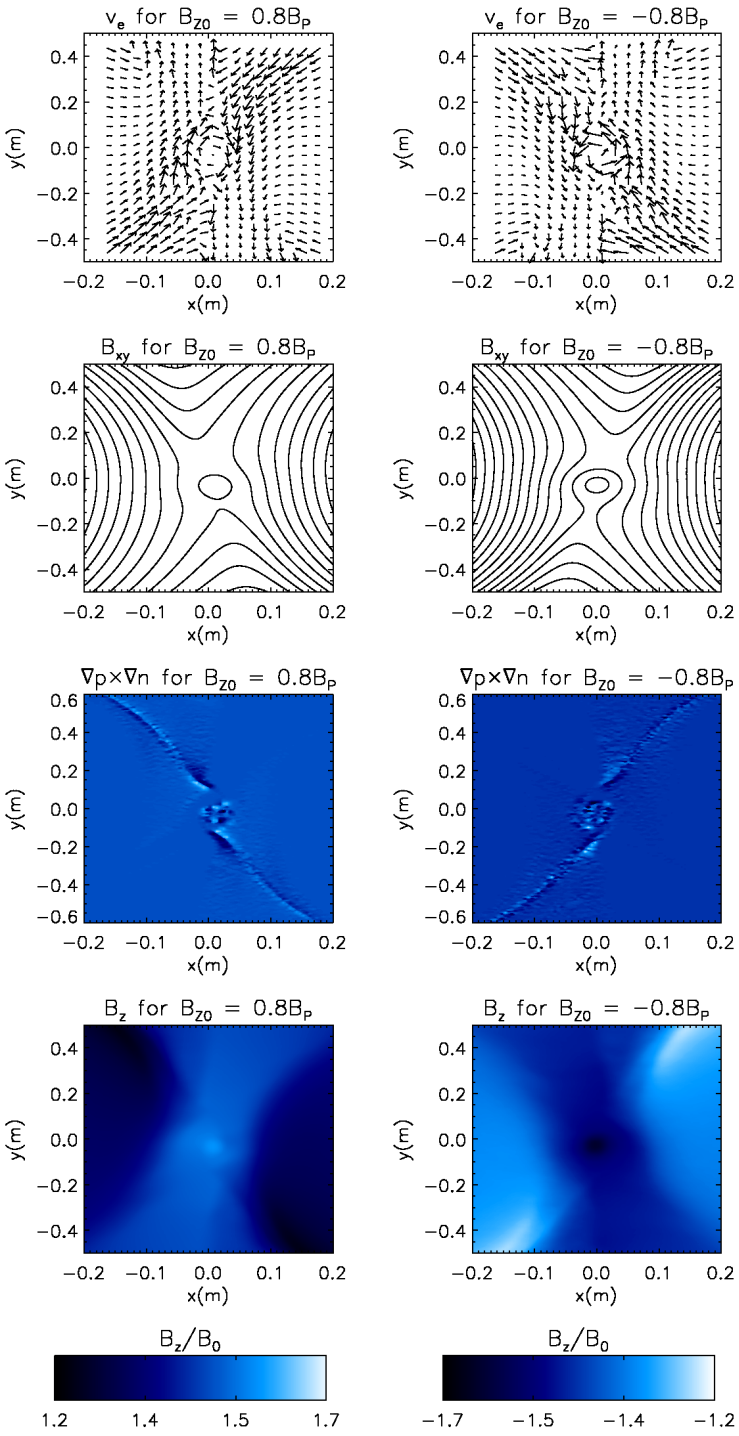

FIGURE 2.9: From top to bottom: in-plane electron velocity, in-plane magnetic field lines (contours of A_z), the value of the $\nabla n \times \nabla p$ term and out-of-plane magnetic field in the vicinity of the vortex for guide-fields of $B_{Z0} = 0.8B_P$ and $B_{Z0} = -0.8B_P$, at $500\omega_{pe}^{-1}$.

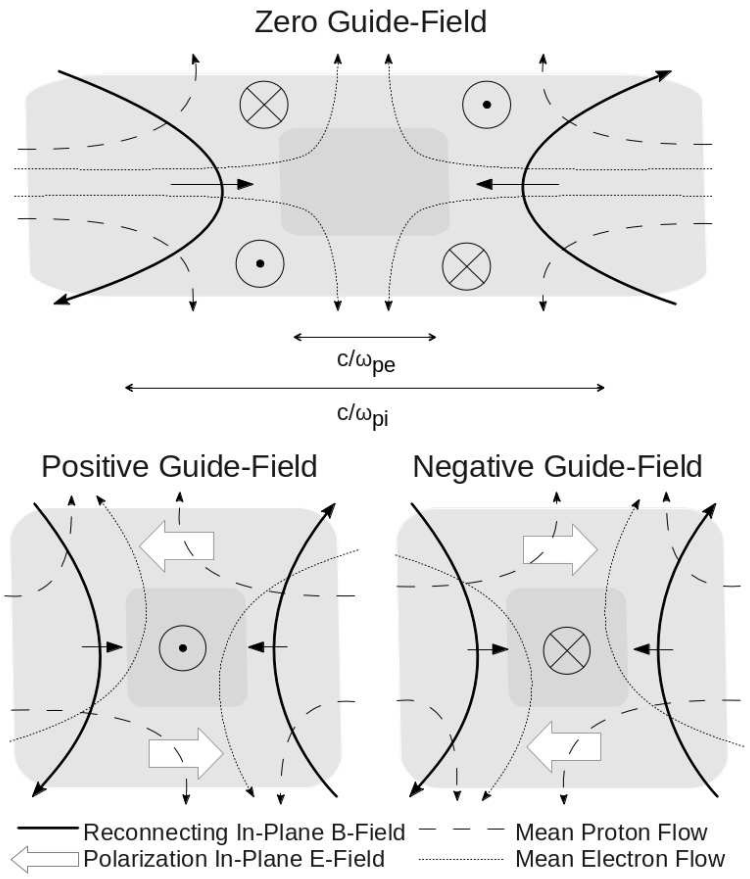

FIGURE 2.10: (Top) Adopted from [120], chapter 3.1.1, showing a schematic of dissipation region for anti-parallel reconnection, indicating the decoupled motion of electrons and protons and how they lead to the quadrupolar out-of-plane magnetic field structure. Lengths of the ion and electron dissipation regions are indicated. (Bottom) Proposed version of the above schematic when modified by a positive or negative out-of-plane magnetic guide-field. As shown in each case, shear electron flows are induced along the field lines (see Ref. [120], page 96-101), leading to a polarisation electric field. This in turn leads to polarisation drift of the protons across the diffusion region.

force term, $\nabla n \times \nabla p$, where n and p are electron number density and scalar pressure respectively. This term was plotted for the simulation domain as shown in Fig. 2.9. As can be seen, there is a correlation between areas of high vorticity and the magnitude of the $\nabla n \times \nabla p$ term. However as shown in the figure, the electromotive force appears to be too sporadic to be solely responsible for the effect, indicating that this approach is likely too simplistic to accurately model electron dynamics in this case.

2.3.3 Initial Oscillation in Reconnection Field

Both in the open and the closed boundary case, as well as for increasing guide-fields (see Fig. 2.8), the simulation exhibited a burst of rapid oscillations in the reconnection field, directly preceding reconnection onset. This oscillation was shown to be part of a

more general wave structure in E_z, spreading over the simulation domain. While this oscillation is present in all cases of guide-field, it appears most dominant in the guide-field-free case and was thus investigated for this case. By decomposing the oscillation at the X-point using a wavelet function, the change in frequency was shown to rise from approximately $1\omega_{pe}$ to $2\omega_{pe}$, as shown in Fig. 2.11.

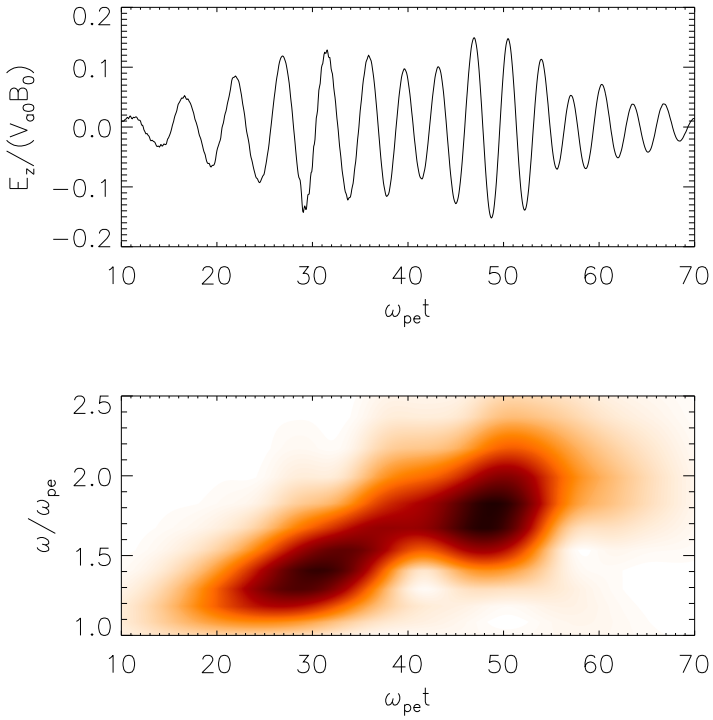

FIGURE 2.11: (Top) The oscillation in E_z at the X-point at the beginning of the simulation. (Bottom) The very same segment of the E_z oscillation, decomposed using a wavelet function, showing the change in frequency over the same time period. The colour intensity in the plot relates to the amplitude of the oscillation.

By taking a horizontal slice through the simulation domain at $y = 0$ and mapping E_z at these locations over time, contours of wave patterns were composed showing the variation of E_z with time and position. These were transformed using a 2D Fourier transform to give a plot representing the dispersion relationships of the waves. To test the consistency of this method, similar tests were carried out for simulation runs with in-plane fields of greater values of B_0, as in (2.1). Resonances seemed to appear, scaling linearly with the field strength (see Fig. 2.12).

The dispersion relationships in Fig. 2.12 were superimposed with the standard dispersion curves for waves in a cold Maxwellian plasma, propagating perpendicularly to a magnetic field, given in Ref. [33], page 45, as

$$c^2k^2 = \omega^2 - \omega_{pe}^2, \tag{2.6}$$

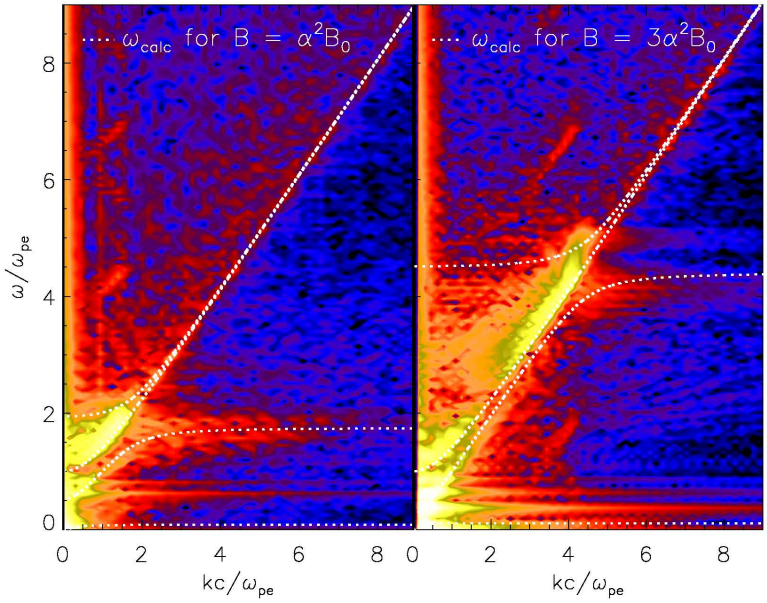

FIGURE 2.12: (left) Dispersion plot generated by sampling E_z over horizontal slice at $y = 0$ over the period in which the initial oscillations occurred, i.e. $100\omega_{pe}^{-1}$, and applying a 2D Fourier transform. (right) Same plot for a three-fold increased in-plane field. Both plots show the logarithm of the respective amplitude and have been superimposed with a simulated dispersion plot for an ideal Maxwellian plasma with identical parameters to the simulation and magnetic field strengths as indicated.

i.e. the normal mode, and

$$c^2k^2 = \frac{(\omega^2 - \omega_1^2)(\omega^2 - \omega_2^2)}{\omega^2 - \omega_{uh}^2}, \tag{2.7}$$

i.e. the extraordinary mode. ω_{uh} represents the upper hybrid frequency, given by $\omega_{uh} = \sqrt{\omega_{pe}^2 + \omega_{ce}^2}$, and ω_1 and ω_2 are given respectively as

$$\omega_1 = (\omega_{uh}^2 - 3\omega_{ce}^2/4)^{1/2} - \omega_{ce}/2 \tag{2.8}$$

and

$$\omega_2 = \frac{\omega_{uh}}{2}\left\{(1 + 3\omega_{pe}^2/\omega_{uh}^2)^{1/2} + (1 - \omega_{pe}^2/\omega_{uh}^2)^{1/2}\right\}. \tag{2.9}$$

The value for ω_{pe} here was set equal to that used in the simulation, while it was found that the value of ω_{ce} that best matches the results is that corresponding to a magnetic field of $\alpha^2 B_0$, which corresponds to the strength of B_y at the x-boundaries of the domain, as given by (2.1). This was shown to hold true for greater values of B_0 as shown in right panel of Fig. 2.12.

From the superimposed dispersion plots in fig. 2.12 it can be seen that the greatest wave amplitudes occur in the ordinary mode. Since these correspond to electromagnetic waves, this occurrence could have observational consequences in the radio wave regime,

potentially solar radio burst fine structure spikes (see Ref. [130]). The frequencies of the waves range approximately from the plasma frequency up to the upper-hybrid frequency, where they reach a maximum. This relates well to [131], where a model of Zebra patterns in superfine solar radio emission is proposed in which plasma oscillations generate wave emissions at the upper-hybrid frequency, propagating perpendicularly to the magnetic field and polarised in the ordinary or extraordinary mode. Observations and further models for the generation of Zebra patterns in superfine solar radio emission, based on plasma mechanisms and also at the upper-hybrid frequency (or multiples thereof), are discussed in Ref. [132]. The same test was carried out by sampling over a vertical slice through the simulation domain at $x = 0$ and plots similar to Fig. 2.12 were generated. However, in this scenario the greatest amplitude seemed to be located in the extraordinary mode, above ω_2.

Furthermore, it was shown directly that the oscillations in the out-of-plane electric field at the X-point correspond to a reversal in the flow of reconnecting magnetic field lines from horizontally inward and vertically outward to vertically inwards and horizontally outward, i.e. oscillatory reconnection occurred (see movie 3 in supplementary material [127]). Oscillatory reconnection in X-point configurations is discussed in detail in Ref. [112] and Ref. [113]. A distinct similarity exists between the results of this study and those of Ref. [113], where, in an MHD based simulation, a magnetic X-point setup in equilibrium is perturbed by a circular, sinusoidal pulse in the plasma velocity perpendicular to the magnetic field. As the pulse impinges on the X-point it similarly induces oscillatory reconnection, and eventually a period of steady reconnection. Similarly to the initial velocity pulse in Ref. [113], the initial compression of the X-point, as well as the corresponding $\mathbf{J} \times \mathbf{B}$ force in the simulation, initiates the initial period of oscillatory reconnection. The corresponding generation of EM waves however is a new finding of this study.

To answer from where the energy of these waves originated, the total energy of the magnetic and electric fields as well as the kinetic energies of electrons and protons (given by summing over the kinetic energies of each particle species, S, by $E_{\mathrm{K,S}} = \Sigma(m_s\gamma c^2 - m_s c^2)$) was investigated in the closed boundary case (as these boundary conditions do not allow any inflows or outflows and thus conserve total energy) for the initial oscillation period, as shown in Fig. 2.13. It is shown that the only decreasing energy component is that of the magnetic field. As the particle kinetic energies also increase it is to be concluded that the wave energy in the electric field also results from the conversion of magnetic energy. It can also be seen that kinetic energy of electrons appears to vary significantly in phase with the electric field energy. This could be linked to the role the electrons play in oscillatory reconnection and the generation of electromagnetic waves. The energy conservation error, $[E(t) - E(0)]/E(0)$, was tested

for these first $100\omega_{pe}^{-1}$ and was found to be 0.0001. For the whole simulation time, i.e. $500\omega_{pe}^{-1}$, this was found to be 0.01.

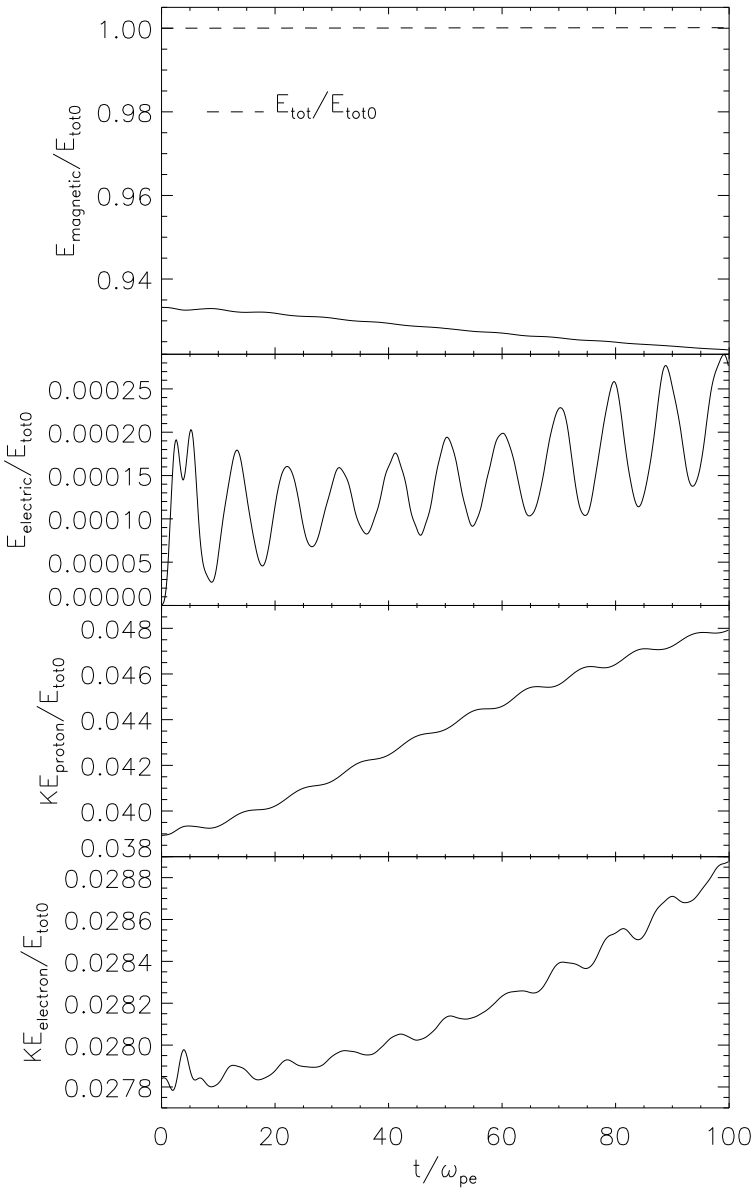

FIGURE 2.13: Showing (from top to bottom) the total magnetic field energy and total electric field energy, integrated over the simulation domain, and the total kinetic energies of protons and electrons, summed over all particles, all for the closed boundary case over the initial period of oscillation. Since energy is conserved in this case (see additional line in total magnetic energy plot) the increase in electric field energy (as well as kinetic energies) must be supplied by the decrease in magnetic field energy.

2.3.4 Octupolar out-of-plane magnetic field structure generation

In the zero guide-field case, an additional discovery was made when analysing the out-of-plane magnetic field during the formation of the quadrupolar field of reconnection:

In the closed boundary case additional regions of magnetic polarity in the out of plane magnetic field emerged near the corners of the domain, each with opposite polarity of the respective region of the quarupolar field at the centre of the domain. In order to make sure that this was not an artefact of the boundary conditions, simulation runs with larger system sizes were conducted, ranging from $4c/\omega_{pi}$ to $16c/\omega_{pi}$, corresponding to 400x400 to 1600x1600 simulation grid cells. The value of B_0 for the different runs was adjusted such that the Alfvén speed at the y-boundary was fixed as $v_a = B_b/\sqrt{\mu_0 \rho} = 0.1c$. As can be immediately seen in Fig. 2.14, for system sizes of $8c/\omega_{pi}$, an octupolar out-of-plane magnetic field emerges both in the closed case after about $400\omega_{pe}^{-1}$ in the open case after and $600\omega_{pe}^{-1}$, prompting further investigation.

In order to determine the strengths of the magnetic field components making up the quadrupole (quadrupolar components) and the additional ones (octupolar components), the bottom left quarter of the simulation domain was isolated and the maximum value of the out-of-plane magnetic field, representative of the quadrupolar field, and the minimum value, representative of the octupolar field components, were plotted (see Fig. 2.15). As shown, for both boundary cases, the octupolar field components reach a peak in field strength only after the peak in the quadrupolar field is reached. Also, it is shown that increasing the domain size leads to an increase in the strength of octupolar field components, indicating that this effect could occur in a wide open system. Excluding the small scale open boundary case, where no significant development was observed, peak field strengths of octupolar components are shown to range from $0.1B_b$ to $0.2B_b$, representing a significant fraction of the quadrupolar field strength in both boundary cases.

It is to be noted that, at the beginning of the simulation, a different type of octupolar magnetic field structure emerges, as shown in panel (a) of Fig. 2.14, where regions of opposite field polarity briefly appear within the quadrupolar structure, at a significantly smaller magnetic field strength. The same effect was demonstrated in Ref. [133] using a hybrid simulation of a tearing instability and was shown to be the result of a competition between initial differential ion flows. It is thus confirmed that this effect occurs both in X-point collapse and tearing-mode reconnection setups.

To determine the cause of the additional magnetic poles in terms of the currents in the simulation, Ampère's law was taken in component form, such that

$$dB_z = \mu_0 j_{x,ion} dy + \mu_0 j_{x,electron} dy + \frac{1}{c^2} \frac{\partial E_x}{\partial t} dy \tag{2.10}$$

and

$$dB_z = -\mu_0 j_{y,ion} dx - \mu_0 j_{y,electron} dx - \frac{1}{c^2} \frac{\partial E_y}{\partial t} dx. \tag{2.11}$$

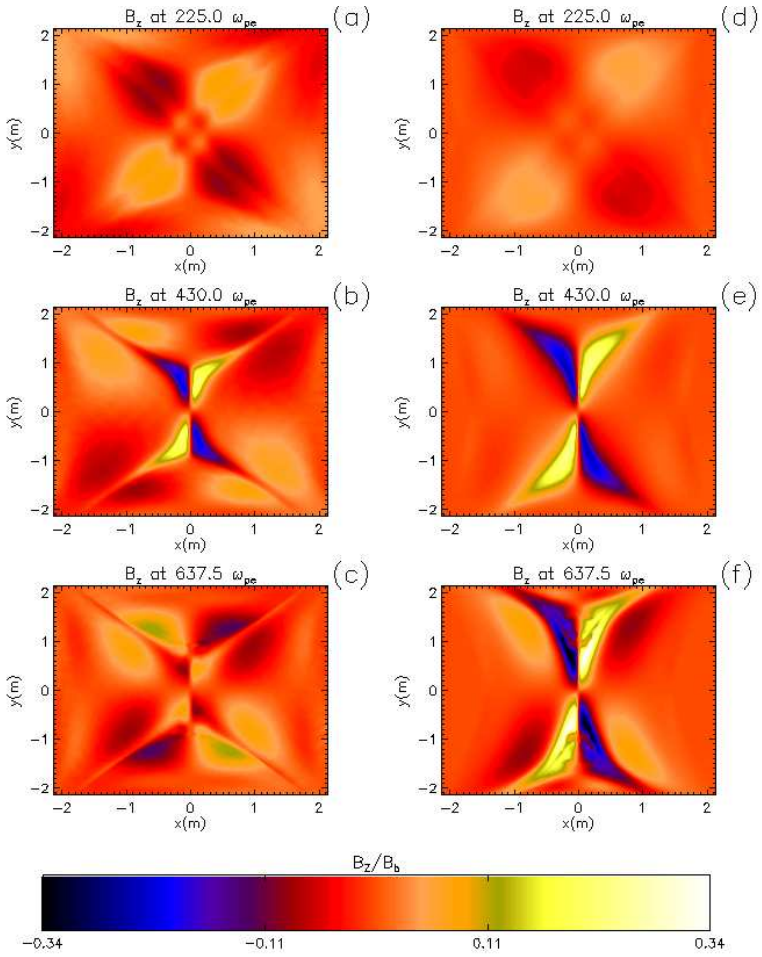

FIGURE 2.14: Vertically from (a) to (c), the out-of-plane magnetic field at 3 consecutive times, for closed boundary conditions for a domain size of $8c/\omega_{pi}$. Note that at the onset of reconnection, in panel (a), an initial octupolar field pattern occurs, similar to the one shown in Fig. 5 in Ref. [133], while later in the simulation a more substantial octupolar field emerges, having opposite polarity to the initial one. Again vertically, panels (d) to (f) similarly show the evolution of the out-of-plane magnetic field for open boundary conditions.

This way an integration could be carried out, allowing for B_z to be derived from the individual currents, allowing contributions from different currents to be established. The individual currents for electrons and ions are calculated by EPOCH on each grid cell and the displacement current was obtained by taking a five-point stencil using electric field values at the same cell, separated over four time steps. As a starting point for the integration the new B_z was set to zero at the centre of the grid, i.e. $B_z(0,0) = 0.0$, as is consistent with it being at the centre of the domain. Thus, it was possible to individually integrate over the simulation grid, using the three different currents, to obtain their individual contributions to B_z. E.g. using Eq. (2.10) one obtains

$$B_{z,ion}(0, L_y) = \int_0^{L_y} j_{x,ion}(0, y)\, \mathrm{d}y \tag{2.12}$$

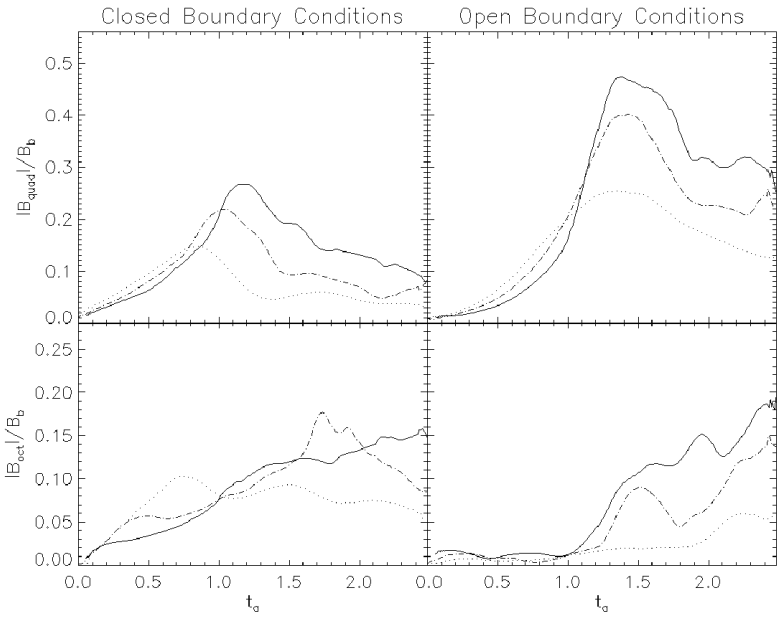

FIGURE 2.15: Showing time dynamics of octupolar and quadrupolar magnetic field component maxima for closed and open boundary conditions. Dotted lines correspond to system sizes of $4c/\omega_{pi}$, dashed lines to system sizes of $8c/\omega_{pi}$ and solid lines to system sizes of $16c/\omega_{pi}$.

followed by (2.11) to get

$$B_{z,ion}(L_x, L_y) = -\int_0^{L_x} j_{y,ion}(x, L_y)\,\mathrm{d}x, \tag{2.13}$$

where (L_x, L_y) represents an arbitrary point on the B_z grid. Carrying out the same integration for all L_x and L_y on the grid also for the electron and the displacement currents, plots shown in Fig. 2.16 are obtained. Only the lower left quarter of the simulation domain is shown due to considerations of symmetry. As expected, based on Hall dynamics, the contribution to the quadrupolar components is provided entirely by the electron currents. As explained in Ref. [134] they are the result of coupled electrons moving to and from the X-point in order to conserve charge neutrality as field lines deform during reconnection. In addition to this, we show that the contribution to the octupolar components is provided by the ion currents. A further observation is that, after being expelled from the X-point, there is an additional flow of electrons towards the horizontal centre of the domain. This is likely also due to electrons moving along the field lines to restore charge neutrality. This current makes up the additional positive contribution to the out-of-plane magnetic field at the bottom of panel (a) in Fig. 2.16 and it is this contribution which leads to the separation of the octupolar components from the simulation boundary (see panel (b) to (c) in Figure 2.14). The contribution of the displacement currents was small in comparison and therefore a dedicated plot is

omitted. By comparing panels (c) and (d) of Fig. 2.16, it can be seen that the calculated field corresponds well with the one obtained directly from the simulation.

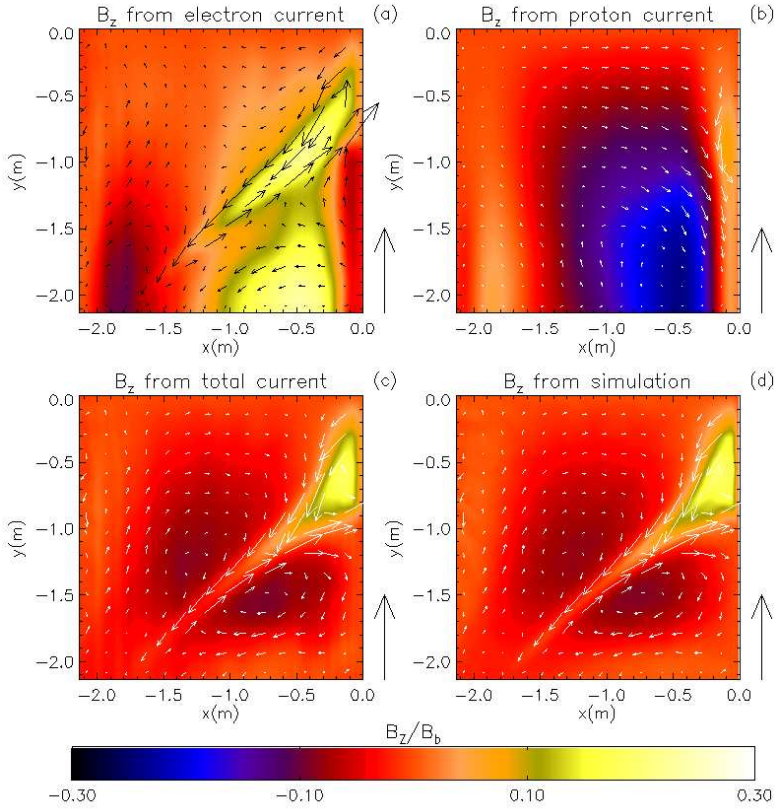

FIGURE 2.16: For closed boundary conditions for a domain size of $8c/\omega_{pi}$ around $430\omega_{pe}^{-1}$ ($1.08t_a$), when octupolar components first emerge, panels (a) and (b) show the out-of-plane magnetic field over the bottom left quadrant of the domain, calculated from electron and ion currents respectively, based on Ampère's law. Panel (c) shows the total of these two contributions as well as the contribution from the displacement current (small). Panel panel (d) shows the full out-of-plane magnetic field obtained directly from the simulation, effectively representing the bottom right quadrant of panel (b) in Figure 2.14. Arrows on panels indicate direction and intensity of the current density at respective grid cells. Arrows beside panels represent the current density for charged particles moving at the Alfvén speed ($v_a = 0.1c$) with a particle density of n_e, i.e. the initial charge density in the simulation domain.

2.4 Summary and Conclusion

Simulations of magnetic reconnection during collisionless, stressed X-point collapse by D. Tsiklauri and T. Haruki [62, 64] were extended by the inclusion of the out-of-plane magnetic guide field and the use of different boundary conditions. A kinetic, 2.5D, fully electromagnetic, relativistic particle-in-cell numerical code was used.

Two cases of boundary conditions for this simulation were defined and investigated i.e. closed boundary conditions, where particles are reflected from the boundary and

magnetic flux is confined, and open boundary conditions, where particles and magnetic flux can escape through boundary. In the zero guide-field case (see Fig. 2.3) it was found that for closed boundary conditions the reconnection electric field at the X-point reached an initial peak at approximately $170\omega_{pe}^{-1}$ and a second peak at approximately $340\omega_{pe}^{-1}$, thus resulting in a very distinct two peak profile. In the open boundary case reconnection onset was slower and a distinct peak in the reconnection field was not reached before $200\omega_{pe}^{-1}$. However, the reconnection rate was also slower to saturate, declining by less than half before the end of the simulation i.e. at $500\omega_{pe}^{-1}$. Further, the peak value of reconnection current at the X-point for open boundary conditions was approximately twice the value in the closed boundary case. In both cases a peak in the particle number density is observed in the proximity of initial peak values.

- Variation in guide-field:

Guide field values were chosen ranging from 0.2 to 1.0 of the in-plane magnetic field, as defined in (2.3). In the closed boundary case (see Fig. 2.5) peak reconnection rates were reached sooner for greater guide-fields, however peak values were greatly reduced. In the open boundary case (see Fig. 2.4) the onset of reconnection was increasingly delayed for greater guide-field, however, reconnection peak rates were shown to be higher for guide-fields up to 0.8 the in-plane field. Reductions in amplitude are also observed in the MRX, as shown in Ref. [115], where this was shown to be due to a reduction in the Hall-current. Delays in on-set times observed are consistent with results in Ref. [75] and may be indicative of more limited meandering motion of electrons. Initial increases in the reconnection current, similar to results in Ref. [74], where studied at low values of guide-field. It was possible to establish an optimal guide-field value for which the initial rate of increase of the current in the open boundary case was maximised, found to be between 0.1 and 0.2 the in-plane field.

An unusually high peak in the out-of-plane current at the X-point was observed in the open-case for a guide-field of 0.6 the value of the in-plane field. Further it is shown in Fig. 2.6 that, towards the end of the simulation for a guide-field of 0.8 the in-plane field, a strong localised current forms at the X-point. Both of these observations are linked to the emergence of an electron vortex alongside a magnetic island at the X-point. It is shown in Ref. [89] that magnetic islands forming at the X-point lead to electron acceleration such that a localised out-of-plane current is produced, consistent with these observations.

- Vortex formation:

The electron vortex that emerged, for guide-fields equal or greater than 0.6 the in-plane field, was shown to reverse vorticity if an oppositely pointing guide-field was

applied (see Fig. 2.9). It was concluded that this could be explained by consideration of the decoupled motion of electrons and protons in the diffusion region (see Ref. [120], chapter 3.1.1). While in the zero guide-field case quadrupolar magnetic fields emerge at the reconnection site due to current loops in the particle flows, imposing a sufficiently strong guide-field not only causes an electron shear flow along the current sheet, but the guide-field appears to impose current loops and thus vortical motion is induced. Also, it was shown that magnetic islands in the in-plane magnetic field emerge at the same location as the vortex. This coincides with the results found by [79], which suggest that magnetic islands in reconnection with a guide-field generally emerge as a result of vortical motion of electrons, triggered by a Kelvin-Helmholtz instability. It was also investigated whether the electro-motive force, as described in Ref. [129], was likely to play a part in the vortex generation. It was shown that the terms responsible for the generation of electro-motive force, i.e. $\nabla n \times \nabla p$, were of greater magnitudes in the simulation domain at greater values of vorticity. This will be further investigated elsewhere.

- Initial oscillations:

The initial oscillations in the out-of-plane electric field were investigated and were shown to be part of a larger wave pattern. By making cuts over the x and y axes of the simulation domain and sampling over time, contours of the wave patterns were obtained and analysed using a 2D Fourier transform (see Fig. 2.12). From this it was possible to conclude that the emerging waves are predominantly in the ordinary mode, in the horizontal direction, and the in the extraordinary mode, in the vertical direction, and thus could be of observational relevance to solar radio burst fine structure spikes. Waves in the ordinary mode were shown to reach frequencies of up to the upper-hybrid frequency, which corresponds well with the model for the generation of Zebra patterns in superfine solar radio emission described in Ref. [131]. The oscillations were also shown to be linked with oscillatory reconnection through the X-point. Further, by plotting the total energy contained in the magnetic and electric field as well as the total kinetic energy of the protons and electrons over the initial period of the oscillation in the closed (i.e. energy conserving) boundary case, it was shown that the energy of the waves must be supplied by the conversion of magnetic field energy (see Fig. 2.13). The exact link between the initial contraction of the X-point and the waveform is still to be investigated.

It is to be stressed that these electric field oscillations are not an artefact of idealised boundary conditions. In the solar atmosphere, the reconnecting magnetic field is anchored to the photosphere, while being able to reconnect and change its configuration in the corona and the chromosphere. In our model, in the closed boundary case, a similar configuration is presented since constant magnetic flux at the boundary mimics partial anchoring of field lines in the photosphere, while X-point collapse occurs as in the corona

or the chromosphere. Moreover, the oscillation also occur in the open boundary case, which is relevant to the coronal heights.

- Octupolar out-of-plane magnetic field:

In addition to the quadrupolar magnetic field, known to emerge in magnetic reconnection, four additional regions of opposite magnetic polarity in the out-of-plane magnetic field were observed in a PIC simulation, using a stressed X-point collapse, for both closed and open boundary conditions. As shown in Fig. 2.14, for each central region of magnetic polarity, an additional region of opposite magnetic polarity emerges. The resulting octupolar structure appeared most prominently in late in the simulation, i.e. after the peak in the quadrupolar field strength was reached. This is consistent with plots obtained from taking the maximum and minimum out-of-plane magnetic field values in the lower left quarter of the domain, representative of the quadrupolar and octupolar field components respectively (see Fig. 2.15). For both boundary conditions, the quadrupolar field components consistently peak and diminish within $2.5t_a$, while on the other hand the octupolar field components remained substantial. Thus, there exists a point when both magnetic fields are approximately equal. An ideal opportunity for observation would thus be at later times, when quadrupolar components subside, while octupolar components persist.

By breaking Ampère's law into components given on the simulation grid and integrating to obtain B_z it was possible to determine contributions to B_z from electron and proton currents separately (see Fig. 2.16). It was shown that the inner quadrupolar structure is linked to the electron motion, as is consistent with Hall dynamics, while the octupolar components are linked to the ion motion. This can be explained by the fact that, while electrons are coupled to field lines shortly after reconnection, their vertical motion away from the X-point thus determined by the outflow speed of the field lines, ions travel a greater distance before recoupling to the field. As shown in panel (a) of Fig. 2.16, electrons move along the field lines through the X-point and no significant motion perpendicular to the field lines occurs (note that current direction is opposite to electron flow direction). Panel (b) on the other hand shows ions moving across the field lines towards and away from the X-point, thus resulting in the current making up the octupolar field components. As the reconnection rate, and thus the velocity of out-flowing field lines decreases, a point is reached where contributions from the ion current become dominant.

Since the magnetic quadrupole serves as a marker of Hall reconnection it would be reasonable to investigate if the magnetic octupolar structure presented here could also be observed in a laboratory or in space-craft missions. It is to be stressed that, as shown in Fig. 2.15, the magnetic components making up the octupolar field become more

significant after the inner quadrupolar field has peaked. Initial testing with greater ion to electron mass ratios further indicate that the latter is the case and will be reported elsewhere. We also stress that open boundary conditions are applicable to geomagnetic tail reconnection. In fact, while this was studied with focus on tearing mode, Dungey's first model was based on X-point collapse. Thus we believe that observing octupolar structure in the geomagnetic tail could be a distinguishing factor between tearing mode and X-point collapse reconnection models.

Chapter 3

The effects of ion mass variation and domain size on octupolar out-of-plane magnetic field generation in collisionless magnetic reconnection

In section 2.3.4 it was established that the generation of octupolar out-of-plane magnetic field structure in a stressed X-point collapse is due to ion currents. The field has a central region, comprising of the well-known qaudrupolar field (quadrupolar components), as well as four additional poles of reversed polarity closer to the corners of the domain (octupolar components). In this chapter, the dependence of the octupolar structure on domain size and ion mass variation is investigated. Simulations show that the strength and spatial structure of the generated octupolar magnetic field is independent of ion to electron mass ratio, thus showing that ion currents play a significant role in out-of-plane magnetic structure generation in physically realistic scenarios. Simulations of different system sizes show that the width of the octupolar structure remains the same and has a spatial extent of the order of the ion inertial length. The width of the structure thus appears to be independent on boundary condition effects. The length of the octupolar structure, however, increases for greater domain sizes, prescribed by the external system size. This was found to be a consequence of the structure of the in-plane magnetic field in the outflow region halting the particle flow and thus terminating the in-plane currents that generate the out-of-plane field. The generation of octupolar magnetic field structure is also established in a tearing-mode reconnection scenario. The differences

in the generation of the octupolar field and resulting qualitative differences between X-point collapse and tearing-mode are discussed.

3.1 Introduction

Magnetic Hall reconnection, first proposed by B. Sonnerup [51], is a mode of reconnection relying on the decoupling of ions and electrons in a diffusion region and is of great interest in the study of magnetic reconnection. It presents an alternative to the Petschek model, which relies on an anomalous resistivity [46]. Even in setups suitable for Petschek reconnection, contributions of Hall effects need to be considered. A recent analytical result, corroborated by a numerical study, shows that the transition from Petschek to Hall reconnection occurs when the half-length of the current sheet reaches the ion inertial length [135]. This was shown to be a direct consequence of a generalised scaling law, relating the reconnection rate to the distance between the X-point and the start of slow mode shocks.

An observational consequence of Hall reconnection is the generated quadrupolar out-of-plane magnetic field, induced by currents resulting from the decoupling of electrons from ions i.e. the Hall currents, first demonstrated in a study by Teresawa [136]. The effect was further shown to occur in numerical Hybrid simulations [63, 137, 138] and later in a full Particle In Cell (PIC) numerical simulation [61]. However, as shown in Ref. [133], kinetic simulations of magnetic reconnection, where the Hall term was excluded, can also lead to quadrupolar magnetic field structure generation, due to ion diamagnetic drifts driven by an anisotropic ion stress tensor. By being an observational signature of magnetic reconnection, the quadrupolar field has thus been of great interest in recent spacecraft missions, including Polar [66] and Cluster [67]. Both missions observed individual magnetic poles in the magneto-tail of the Earth. Subsequently, a full quadrupolar pattern was observed in a multi-spacecraft Cluster mission [32]. The experimental evidence of the full quadrupolar structure was also found at the MRX facility [65]. It was shown in Ref. [139] that inhomogeneous ion flow and pre-existing out-of-plane magnetic fields, can lead to the generation of quadrupolar out-of-plane magnetic field structure without the Hall term. Thus, the generation of a quadrupolar magnetic field is not necessarily a tell-tale sign of Hall-mediated magnetic reconnection.

Ref. [134] proposes an analytical model, explaining the Hall out-of-plane quadrupolar magnetic field near an X-point as the result of electron motion towards and away from the X-point, as field lines reconnect. A spatially uniform ion distribution was assumed. Since ions decouple from the magnetic field sooner than electrons, they move independently of field lines near the X-point. On the other hand, electrons are assumed to be

coupled to the field lines and thus only move with the field and along the field lines. Since the spacing of field lines increases as they approach the X-point, the electron density decreases. Thus, due to the uniform ion density, this results in a net positive charge. Electrons in the inflow region therefore move along the field lines to towards the X-point to restore charge neutrality and then move away from the X-point in the out flow region, leading to a quadrupolar pattern.

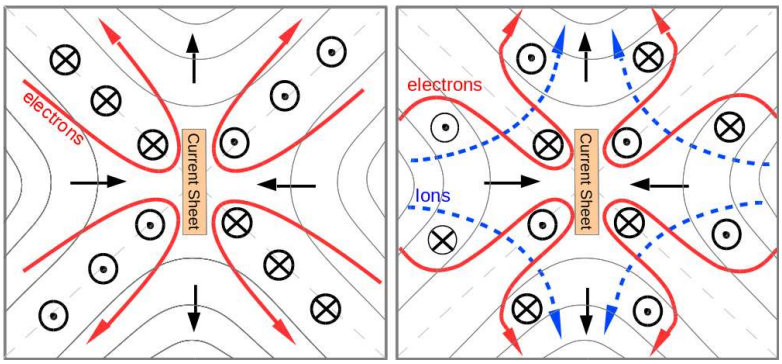

FIGURE 3.1: (Left) Reconnection at an X-point superimposed with electron motion (as indicated by the labelled track) and the resulting out-of-plane magnetic field structure, as given by the analytical model in Ref. [134]. Black arrows on field lines signify inflow and outflow regions. Ions here are assumed to be decoupled and uniformly distributed. As the spacing of field lines increases at the X-point, coupled electrons in the inflow region move towards the X-point to restore charge balance. Similarly, the electrons in the outflow region move outwards along the field lines and the characteristic quadrupolar out-of-plane magnetic field structure is generated. Due to the non-inclusion of ions, the out-of-plane magnetic structure is not localised and extends along the seperatrices. (Right) The setup and resulting current and out-of-plane magnetic field generation for X-point collapse, from simulations in chapter 2. It is shown that, as in-plane field lines reconnect, electrons move towards and then away from the X-point, generating quadrupolar structure as described in Ref. [134]. Away from the X-point, ions move independently from the field (see dashed tracks), generating a magnetic field of opposite polarity to that of the quadrupole, thus generating an overall octupolar structure. Electrons at the edge of the ion diffusion region move such that they cancel the out-of-plane field, thus making it *localised*.

While this theoretical model describes the generation of the quadrupolar field, it is pointed out that it is limited by the non-inclusion of ion currents, resulting in a quadrupolar field that stretches along separatrix arms indefinitely. In Section 2.3.4 it was shown that, in an X-point collapse scenario, ion currents not only provide a cut-off to the quadrupolar field, but contribute to the out-of-plane magnetic structure themselves. The out-of-plane magnetic field that emerged in Section 2.3.4 was shown to have the well-known quadrupolar field at the centre, generated by electron currents, and four regions of opposite magnetic polarity on the outside, resulting from ion currents, as illustrated in Fig. 3.1. The overall field appears to have an octupolar structure (we shall refer to the inner magnetic quadrupolar field as quadrupolar components and the outer field of opposite polarity as the octupolar components).

At the beginning of the simulation, a different type of octupolar magnetic field, with smaller field strength ($\approx 3\%$ of external in-plane field), emerges. The same effect was demonstrated in Ref. [133] (see their Fig. 5) using a hybrid simulation. However, the present study focusses on the larger field structure ($\approx 15\%$ of external in-plane field), emerging *later* in the simulation. Further, octupolar signatures have been observed in tearing-mode reconnection scenarios with multiple islands as shown in Ref. [140], Fig. 4, and in Ref. [141]), Fig. 3. The emergence octupolar structure in these scenarios is linked to the island coalescence and is beyond the scope of this thesis.

Here, we extend works presented in section 2.3.4 by investigating the dependence of the octupolar field on variation of electron to ion mass ratio and the domain size. It is established that the generation of octupolar field is neither the result of unphysical boundary conditions nor unrealistic mass ratios. Thus we show that the results are relevant for real laboratory experiments and spacecraft observations. Further, by simulating a tearing-mode set-up, as previously studied in Ref. [61], it is shown that a similar type of octupolar structure can also be found in reconnection scenarios other than X-point collapse, where their emergence have been previously overlooked.

3.1.1 Simulation Setup

The simulation setup and PIC code are the same as described in section 2.2, with the exception that no magnetic guide-fields are applied and the system size and electron to ion mass ratio are varied. For greater system sizes, B_0 in Eqn. 2.1 was reduced such that the Alfvén speed at the y-boundary remained approximately $V_a = 0.1c$ in all runs. This further assured that the parameters in the simulation were adjusted to assure that the electron plasma frequency at the boundary was equal to the electron cyclotron frequency at the boundary, i.e. $\omega_{pe} = \omega_{ce}$. Also, the number of grid-cells was increased such that their length and width remained the Debye length. The boundary conditions in these simulation runs were set as closed (see section 2.2.3) since the a more distinct octupolar field was observed in this case (see section 2.3.4). Further an additional setup was considered based on Ref. [61] to compare the results to a tearing-mode type reconnection run.

3.2 Octupolar structure for different domain sizes

While having the advantage of simulating a self-contained, energy conserving system, flux conserving boundary conditions naturally have a limiting effect on the movement of field lines, especially closer to the edge of the domain. In order to diminish this effect

and allow natural reconnection dynamics to occur, different system sizes were used for the square simulation domain, ranging from $4c/\omega_{pi}$ to $32c/\omega_{pi}$. The effective grid sizes used ranged from $2L = 2.14$ m to $2L = 17.12$ m. For most of the runs, simulation grid cells were set to the Debye length (λ_D), thus leading to grids ranging from 400x400 to 1600x1600 grid cells. However, for the case of a system size of $32c/\omega_{pi}$ this was not computationally possible. An under-resolved simulation run, using 1600x1600 grid cells and thus cell size of $2\lambda_D$, however proved consistent and was shown to be energy conserving despite possible numerical heating and is thus included here. The ion mass was set to 100 times the electron mass, i.e. $m_i = 100m_e$, to speed up the code. The value of B_0 for the different runs was adjusted such that the Alfvén speed at the y-boundary was fixed as $v_a = B_b/\sqrt{\mu_0 m_i n_i} = 0.1c$, where B_b represents the strength of the magnetic field at $(x_{max}, 0)$. For meaningful comparison between the runs, the x-axes of plots showing time dynamics use Alfvén time,

$$t_a = L/v_a, \tag{3.1}$$

where L denotes the half-length of the system size.

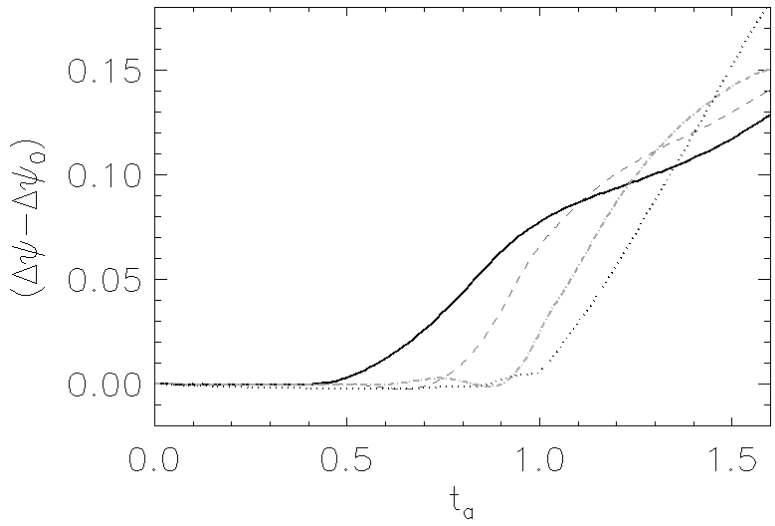

FIGURE 3.2: The reconnected flux for simulation runs of different domain sizes, given by the difference between magnetic flux at X-points and O-points, indicative of the reconnection rate (shown for different electron to ion mass ratios in Fig. 2 of Ref. [62]). The solid, dashed, dash-dotted and dotted curves show the reconnection rate for domain sizes of $4c/\omega_{pi}$, $8c/\omega_{pi}$, $16c/\omega_{pi}$ and $32c/\omega_{pi}$ respectively. The reconnected flux is normalised by $B_b c/\omega_{pi}$. For all system sizes a similar amount of reconnected flux is reached within $1.5t_a$. Note that, for each case, initial reconnection rate maxima are reached also within this period.

By plotting the reconnected in-plane magnetic flux over time for runs with different system sizes (see Fig. 3.2), it was determined that in all runs, a similar amount of flux is reconnected within $1.5t_a$. For all cases an instant of maximum reconnection rate is

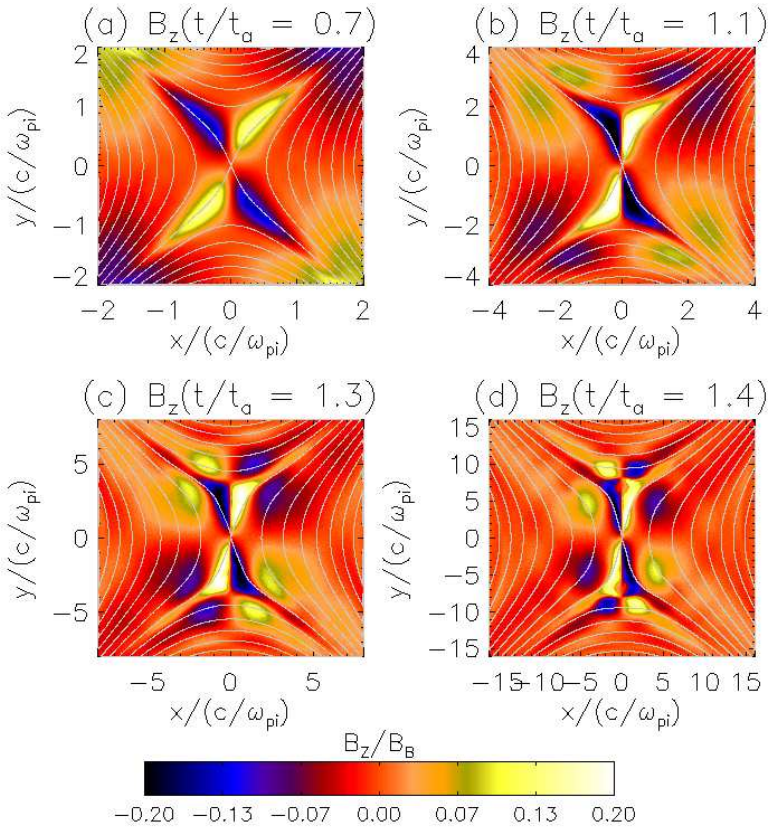

FIGURE 3.3: The magnetic out-of-plane field for simulation runs with different domain sizes at peak reconnection rate, as indicated in Fig. 3.2. Panels (a) to (d) show runs using system sizes of $4c/\omega_{pi}$, $8c/\omega_{pi}$, $16c/\omega_{pi}$ and $32c/\omega_{pi}$ respectively. White lines superimposed on plots show the in-plane magnetic field at the same time. Different times correspond to time instants when maximum reconnection rate is reached.

reached within $1.5t_a$, which occurs at progressively later times for greater system sizes (note that time normalisation is as stated in Eq. (3.1)). This can be understood as a result of the increasing difference in length between the system size and the diffusion region. I.e. while the system size increases, the width of the diffusion region remains the same and field lines have to travel a greater distance before undergoing reconnection. For a system size of $2L = 4c/\omega_{pi}$ the peak reconnection rate is lower than for the other cases, for which the peak reconnection rate is approximately equal. In this case, the closeness of the boundary to the diffusion region is limiting the reconnection.

The out-of-plane magnetic field for different system sizes at peak reconnection rates is plotted in Fig. 3.3. The width of the out-of-plane magnetic structure does not change with the size of the domain. For system sizes of $8c/\omega_{pi}$, and greater, it can be seen that the horizontal extent of the out-of-plane field is approximately contained within $-4c/\omega_{pi}$ to $+4c/\omega_{pi}$. Since the particle density and mass ratios are fixed for the different runs, the width of ion diffusion region, $\sim c/\omega_{pi}$, is also fixed. Since ions and electrons only move independently within the ion diffusion region, which allows for in-plane currents

and thus out-of-plane magnetic fields to be generated, it is evident that the emergence of octupolar structure is an aspect of ion diffusion region physics.

The vertical extent of the out-of-plane magnetic field however does increase for greater system sizes. This shows that the generation of in-plane currents occurs at a vertical distance determined by the strength of the in-plane magnetic field, which has equal strengths on relative positions on the domain. The in-plane field lines in Fig. 3.3 show that the value of B_x in the outflow region is fixed at approximately halfway between the X-point and the system boundary, for all simulation runs. Since flux cannot escape from the boundary, this shows that the movement of field lines is halted at the same relative position on the domain for all system sizes. Thus, the motion of electrons must also be halted at this point since they recouple to the field shortly after reconnection. However, ions are still decoupled at this point and over-shoot, thus creating in-plane currents and charge separation. In response, electrons move along the field-lines to restore charge neutrality, resulting in the current loops and out-of-plane magnetic field as illustrated in Fig. 3.1 (right). In panel (a) of Fig. 3.3 we see that for a case of a simulation size of $2L = 4c/\omega_{pi}$, the octupolar components are not contained within the domain. It is thus clear that a simulation size of at least $8c/\omega_{pi}$ is required to comprehensively model the dynamics within the ion diffusion region, without spurious influence from the boundary condition.

3.3 The octupolar field structure for different ion masses

In order to determine that the results relating to octupolar structure hold true for realistic electron-to-ion mass ratios, the relationship between the strength of the octupolar and quadrupolar components and the mass ratio was investigated. In these simulation runs, the mass of electrons was fixed as their physical mass, m_e, and ion masses were varied from $m_i = 50m_e$ to $m_i = 400m_e$. In order to simulate comparable effects, runs with different ion masses were adjusted in scale, such that the domain size remained the same in number of ion inertial lengths, $c/\omega_{pi} = c\sqrt{m_i\epsilon_0/n_ie^2}$. Thus, for greater ion masses, the domain size was increased accordingly (see other findings relating to these setups in Ref. [62]). Further, as before, the Alfvén speed at the boundary was fixed ($v_a = B_b/\sqrt{\mu_0 m_i n_i} = 0.1c$), which means that B_b was adjusted accordingly, while B_0 remained fixed. For meaningful comparison between the runs, time normalisations as in Eq. (3.1) are applied.

By running the simulations described above, for a system size of $4c/\omega_{pi}$, plots in Fig. 3.4 were obtained. Here, the strength of the qudarupolar components was determined as the maximum field strength of the quadrupolar field at each time step, and similarly for the

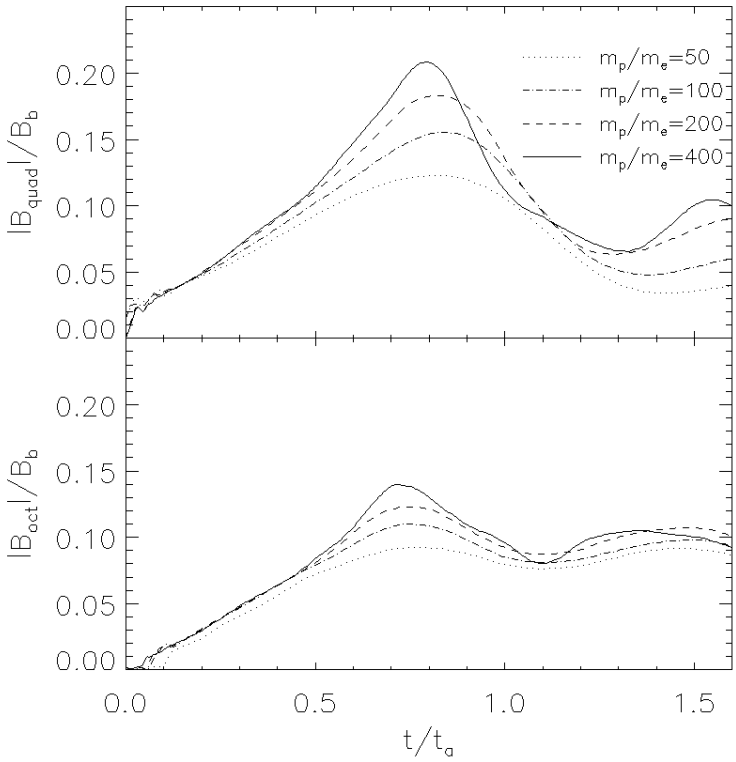

FIGURE 3.4: (Top) The strength of the quadrupolar field components for runs of different ion masses, and corresponding setups as described in the text. Different line styles correspond to different mass ratios as indicated. (Bottom) as above, showing the strength of octupolar field components.

octupolar components, i.e. $\max(|B_{z,quad}(x,y)|)$ and $\max(|B_{z,oct}(x,y)|)$ respectively. We gather from Fig. 3.4 that increasing the ion mass results in a minor increase in the peak strength of the quadrupolar and octupolar field components. In all cases, the octupolar components constitute a significant fraction (i.e. $10-15\%$) of the in-plane magnetic field at the boundary and should therefore be of significance for observations in laboratory plasma experiments and spacecraft observations.

3.4 Octupolar structure for tearing-mode and X-point collapse

The primary factor in the emergence of octupolar structure in X-point collapse is the role of ion dynamics. Due to the large mass of ions compared to electrons, their contribution to the out-of-plane field has generally been considered negligible. However, by revisiting tearing-mode reconnection studies, exhibiting quadrupolar structure, it was possible for us to show that a similar octupolar structure is also present in these scenarios. Using the reconnection setup from a kinetic simulation by Pritchett [61] using tearing-mode

reconnection and carefully investigating the out-of-plane magnetic field structure, it was shown that octupolar components also emerge here (see Fig. 3.5).

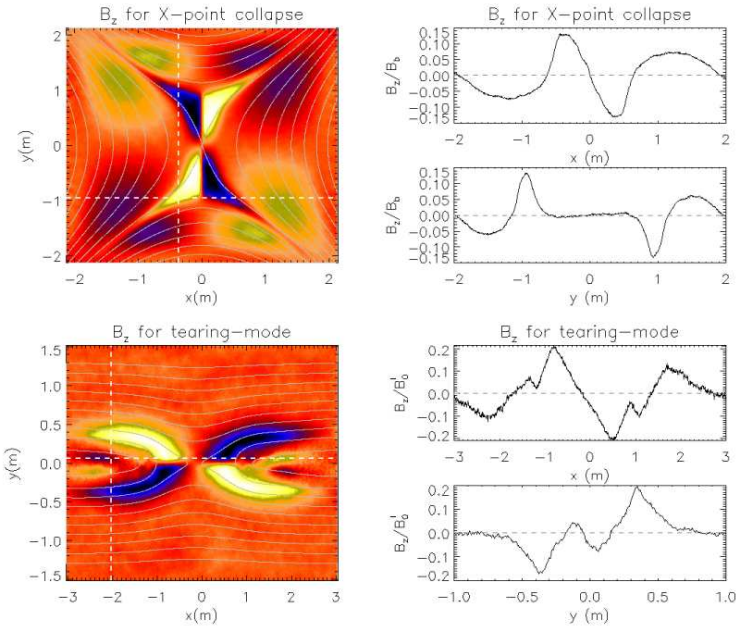

FIGURE 3.5: (Left) The out-of-plane magnetic field structure at peak reconnection for X-point collapse ($t/t_a = 1.1$) and tearing mode ($t\omega'_{ci} = 20$), after Ref. [61]. In both cases, elements of opposite polarity can be seen next to the inner quadrupolar structure, making an overall octupolar field. (Right) The line-profile of the out-of-plane magnetic field at the dotted tracks shown in both contour plots. These profiles effectively represent possible observations by a spacecraft mission, passing though reconnection regions of X-point collapse or tearing-mode type.

The initial reconnection magnetic field used in this simulation is a Harris neutral sheet configuration, given by

$$B_x = B'_0 \tanh(y/\omega), \tag{3.2}$$

together with ion and electron density profiles of

$$n_{e,i} = n'_0 \operatorname{sech}^2(y/\omega) + n_b, \tag{3.3}$$

where B'_0 is determined by the Alfvén speed, which is set as $v_a = c/20$. The initial half-thickness of the current sheet, ω, is set to $0.5c/\omega_{pi}$, n_0 is determined by the equilibrium condition for the neutral sheet and n_b is a constant background density of $0.2n'_0$. The mass of ions in the simulation is set as $m_i = 25m_e$. By introducing an initial flux perturbation, a magnetic island with a transverse size comparable to ω is generated, leading to a reconnection region comparable to the size of the domain.

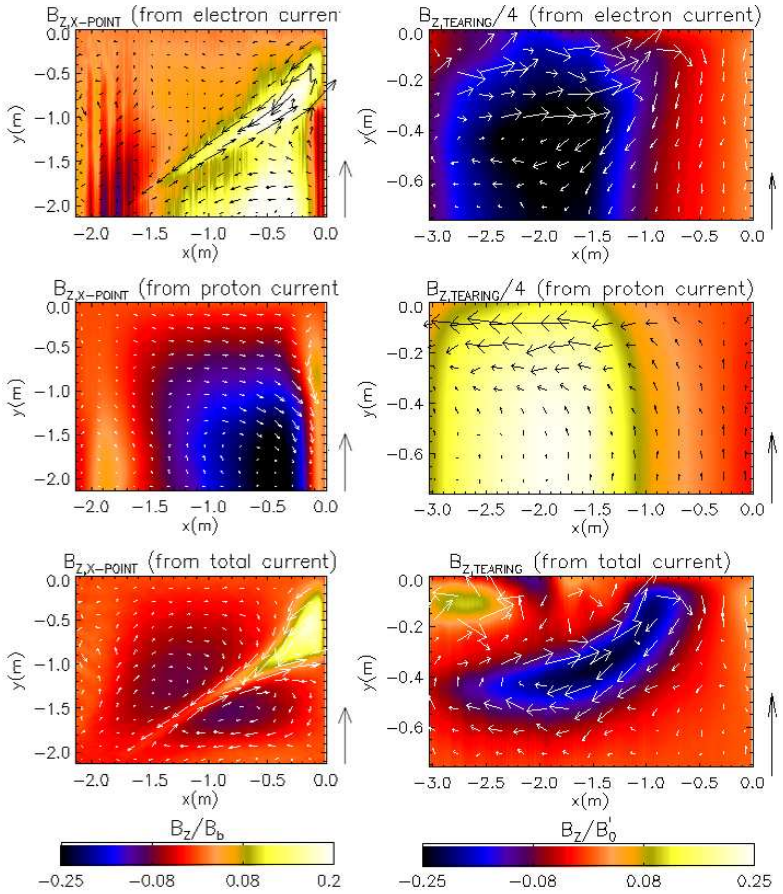

FIGURE 3.6: (Left) The electron and ion current contributions to the out-of-plane magnetic field for an X-point collapse scenario with a domain size of $8c/\omega_{pi}$ at peak reconnection rate ($t/t_a = 1.1$), calculated from electron and ion currents respectively, based on Ampère's law. Superimposed arrows indicate the strength and direction of currents in the domain. Arrows next to plots show current strengths corresponding to charged particles of the characteristic density, moving at the Alfvén speed. (Right) The same for the tearing-mode setup ($t\omega'_{ci} = 20$) according to Ref. [61]. Since ion and electron contributions strongly cancel, i.e. were much greater than the resulting field, different scales are used as indicated.

As shown in Fig. 3.5, there are distinct differences in the out-of-plane magnetic field structure for the two reconnection setups, which could lead to different observational signatures. In X-point collapse, the quadrupolar field emerges in the centre of the domain and two sets of octupolar field components emerge in each of the *outflow and inflow* regions. However, in the tearing-mode case, a quadrupolar field forms at the centre, but octupolar components emerge in the *outflow region only*. Using line plots, the out-of-plane magnetic field along tracks through the octupolar magnetic field structure of the X-point collapse and tearing-mode scenarios is shown. The selected tracks, in all cases, show two consecutive troughs and peaks in the out-of-plane field. In X-point collapse, for both the horizontal and vertical track, the initial through and the final peak have a smaller field strength than the intermediate ones. This is the result of the track starting and ending in the outer region of the domain, where octupolar

components, which are lower in field strength, dominate. In the inner region, the out-of-plane magnetic field is dominated by the quadrupolar components and greater field strengths are observed. For the tearing-mode case, for the horizontal track, this trend is also observed, but for the vertical track it is reversed, i.e. the initial trough and the final peak have a greater field strength than the intermediate ones. This can also be shown to be the result of the order in which the track passes quadrupolar and octupolar field components. In the latter case, the track passes through the quadrupolar components before and after the octupolar components, thus leading to lower field strength in the middle of the track. If a spacecraft mission, such as that discussed in Ref. [32], were to pass through a reconnection region and observe one of these line profiles, it would be possible to distinguish between the possible reconnection setups accordingly.

As in section 2.3.4, to determine the causes of the observed magnetic poles in terms of the currents in the simulation, Ampère's law was taken in component form, such that

$$dB_z = \mu_0 j_{x,ion} dy + \mu_0 j_{x,electron} dy + \frac{1}{c^2}\frac{\partial E_x}{\partial t} dy \tag{3.4}$$

and

$$dB_z = -\mu_0 j_{y,ion} dx - \mu_0 j_{y,electron} dx - \frac{1}{c^2}\frac{\partial E_y}{\partial t} dx. \tag{3.5}$$

By integrating over the domain for these terms, contributions to B_z from individual currents, i.e. electron, ion and displacement current, can be calculated. The individual currents for electrons and ions are provided by the simulation at each grid cell and the displacement current was obtained by taking a five-point stencil using electric field values at the same cell, separated over four time steps. As a starting point for the integration a neutral point in B_z had to be chosen. For X-point collapse, the most logical point was the centre of the domain, since here $B_z(0,0) = 0.0$. For the tearing-mode case, any point far out in the inflow region was suitable, as these regions are shown to be far and disconnected from the diffusion region (i.e. field lines from outside the diffusion region here do not enter the diffusion region) and thus lacking out-of-plane magnetic structure. Thus, it was possible to individually integrate over the simulation grid, using the three different currents, to obtain their individual contributions to B_z. E.g. using Eq. (3.4) one obtains

$$B_{z,ion}(0, L_y) = \int_0^{L_y} j_{x,ion}(0, y)\, \mathrm{d}y \tag{3.6}$$

followed by (3.5) to get

$$B_{z,ion}(L_x, L_y) = B_{z,ion}(0, L_y) - \int_0^{L_x} j_{y,ion}(x, L_y)\, \mathrm{d}x, \tag{3.7}$$

where (L_x, L_y) represents an arbitrary point on the B_z grid.

Carrying out this integration for all L_x and L_y on the grid for all current contributions for both X-point collapse and tearing mode, plots shown in Fig. 3.6 are obtained. For considerations of symmetry, only the lower left quarter of the simulation domain is shown (also note that, since X-point collapse, by convention, has inflow regions along the horizontal axis and tearing-mode along the vertical axis, the sign of the quadrupolar and octupolar field structure is reversed). Top and middle panels show ion and electron current contributions to the out-of-plane magnetic field and the bottom panel the combined contributions, which lead to an out-of plane field as shown in Fig. 3.5. As expected, based on Hall dynamics, the contribution to the quadrupolar components is provided entirely by the electron currents in both reconnection scenarios. Also, as established in Section 2.3.4, the octupolar components are the result of ion currents. However, unlike in X-point collapse, in the tearing mode scenario, octupolar components only emerge in the out-flow region. Furthermore, in the tearing mode case, due to a lack of asymmetry in the inflow region, there are two large contributions from both the ion and electron currents, which cancel to give a neutral field at the edge of the domain.

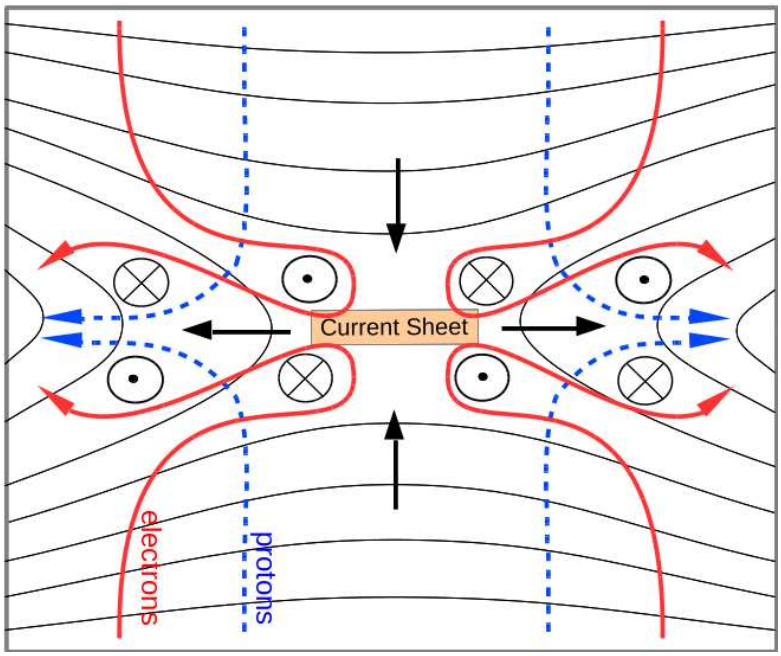

FIGURE 3.7: The setup and observed resulting current and out-of-plane magnetic field generation for a tearing-mode reconnection scenario. As in Fig. 3.1 labelled tracks illustrate the motion of electrons and ions, generating the out-of-plane magnetic field, and black arrows on field lines indicate the inflow and outflow directions.

Ref. [42], chapter 5, gives a detailed analysis of the differences in reconnection setups with almost uniform, i.e. straight inflowing field lines, and non-uniform, i.e. curved field lines, reconnection scenarios. From the results shown in this study, we find that differences in these scenarios can be extended to out-of-plane magnetic field structure.

From Fig. 3.6 it can be seen that, for the tearing-mode scenario, there is a uniform current inflow of both ions and electrons in the inflow region, which means is the reason no out-of-plane magnetic structure is generated in this region. This uniformity in particle inflow is a direct consequence of the lack of curvature of the inflowing field lines. In contrast to this, in X-point collapse, the curvature in the field-lines means that paths of ions and electrons greatly diverge when ions decouple and thus currents and out-of-plane fields, as shown Fig. 3.1, are generated. Further, from Fig. 3.6, we can see that electrons in the tearing-mode scenario exhibit the same Hall-dynamics and flow along the field-lines towards and away from the X-point when entering the diffusion region. However, the field-lines in the outflow region are no longer straight and electrons move in a curved path, away from the X-line, while decoupled ions move in a straight horizontal path away from the X-point. It is this divergence in ion and electron flows which leads to the current loops that generate the octupolar components in the out-of-plane magnetic field structure in the tearing-mode case. The difference of this generation mechanism to that shown for X-point collapse (see Fig. 3.1) can be seen in Fig. 3.7.

3.5 Conclusions

Results relating to the generation of out-of-plane octupolar structure in collisionless reconnection in an X-point collapse were extended by the investigation of the effect of changing domain size and ion masses. It was established that, when fixing the Alfvén speed at the boundary and increasing the size of the domain, the horizontal extent of the octupolar region remains approximately the same (see Fig. 3.3). This was found to be consistent with previous findings since octupolar structure was shown to be the result of in-plane ion currents. As ion currents can only contribute to the out-of-plane magnetic field within the ion diffusion region and, since c/ω_{pi} remained fixed for different system sizes, the width of the octupolar region remained fixed as well. The length of the octupolar structure however increased for greater system sizes. From the in-plane field in Fig. 3.3 it was possible to see that the outward motion of field lines in the outflow region diminishes at the same relative position on the domain for all system sizes. As ions remain decoupled at this point, they over-shoot, causing in-plane currents. Further, electrons compensate for this by moving along the field lines, thus resulting in the current loops and out-of plane magnetic field as shown in Fig. 3.1.

By varying the electron to ion mass ratio and adjusting the simulation domain size to keep the same number of ion inertial lengths, it was shown that octupolar field strength was not significantly affected by the electron to ion mass ratio variation and consistently remained a significant fraction of the in-plane field, i.e. between 10% and 15% (see

Fig. 3.4). Hence, octupolar structure in an X-point collapse would also be generated in plasmas with realistic mass-ratios.

Further, the discovery of octupolar structure in a tearing-mode scenario is presented and the differences in the generation process are analysed. It is found that, due to the uniform nature (i. e. straightness of field lines) of tearing-mode collapse, significant octupolar structure is only generated in the outflow region (see Fig. 3.6). Here, ions flow out along the centre of the diffusion region, while electrons follow a curved path along the field lines (as shown in Fig. 3.7) and thus in-plane currents and out-of-plane fields are formed. Further, by analysing the line profiles of the out-of-plane magnetic field along potential tracks through the reconnection region, distinctly different profiles were obtained which could have relevance to the identification of magnetic structures found by spacecraft missions (see Fig. 3.5).

It is shown in Ref. [142], Fig. 7, that plasma flow along the current sheet can induce streaming sausage and kink modes that generate out-of-plane magnetic fields resembling the one discussed here. Further, in Ref. [143] it is shown that collisionless reconnection in a tearing-mode scenario can be interpreted as dissipation generated by Alfvén eigenmodes, confined by the current sheet in the same way that quantum mechanical waves are confined by a potential. It was shown that for the $n = 1$ mode that this frame work provides analytical predictions for the Hall fields, which are in good agreement with observed magnetic fields. In higher wave modes this framework returns a higher order structure in the Hall fields which could potentially be the cause of octupolar structure in the out-of-plane magnetic field observed in this study. The application of this framework in the X-point collapse case is currently under investigation and will be reported elsewhere.

Chapter 4

The role of electron inertia and reconnection dynamics in a stressed X-point collapse with a guide-field

In previous simulations of collisionless 2D magnetic reconnection it was consistently found that the term in the generalised Ohm's law that breaks the frozen-in condition is the divergence of the non-gyrotropic components of the electron pressure tensor. In this chapter it is shown that, in an X-point collapse with a guide-field close to the strength of the in-plane field, the increased induced shear flows along the diffusion region lead to a new reconnection regime in which electron inertial terms play a dominant role at the X-point. This transition is coupled with the emergence of a magnetic island, and hence a second reconnection site, as well as electron flow vortices, moving along the current sheet. The reconnection rate at the X-point is shown to exceed all lower guide-field cases for a brief period, indicating a strong burst in reconnection. By extending the simulation to three dimensions it is shown that the locations of vortices along the current sheet (visualised by their Q-value) vary in the out-of-plane direction, making up slanted vortex tubes. Vortex tubes on opposite sides of the current sheet are slanted in opposite directions, leading to an overall criss-cross pattern

4.1 Introduction

Dungey's original analysis of magnetic energy conversion in the Earth's magnetosphere describes a reconnection model now known as X-point collapse. Following reconnection

models proposed by Sweet and Parker [40], and later Petschek [43], reconnection setups of sheared magnetic fields, relying on the tearing-mode, became the dominant setup in computational studies of magnetic reconnection. As established in Ref. [62, 64] particle in cell simulations of X-point collapse in the collisionless regime exhibit many of the established features of tearing-mode magnetic reconnection, e.g. the formation of a current sheet, magnetic Hall field generation and independence on system size. However, simulations of X-point collapse have also uncovered several new features, such as initial oscillatory reconnection and vortex formation in the high guide-field regime [144] and a distinct octupolar out-of-plane magnetic field [145, 146], which makes this setup a useful device for the ongoing study of magnetic reconnection. In this chapter we extend the results of Ref. [144], where collisionless X-point collapse with a magnetic guide-field was investigated in a 2.5 PIC (Particle in Cell) simulation. In particular, this chapter analyses the reconnection mechanism (i.e. the term breaking the frozen-in condition) and relevant plasma dynamics for increasing guide-fields.

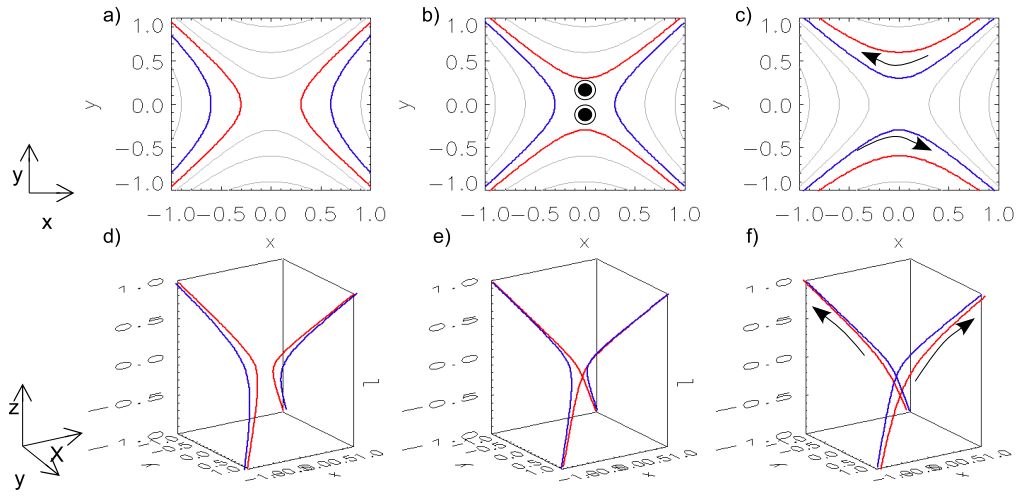

FIGURE 4.1: A visual representation of reconnection at an X-point in a 3D domain, showing the motion of two sets of magnetic field-lines. The perspectives on the simulation domain are indicated for each row. In panel b) the direction of the reconnection electric field induced as the field-lines pass the X-point is indicated. Thin arrows on panels c) and f) indicate the direction of the electron current generated by the reconnection electric field. As shown, the shape of the field-lines guides the accelerated particles such that there is a shear-flow in the xy plane.

The reconnection rate in a 2D reconnection setup can be defined as the out-of-plane electric field where magnetic separatrices meet, i.e. at the X-point. The movement of magnetic field-lines (representative of flux-tubes in 3D) in the xy-plane corresponds to changes in the z-component of the magnetic vector potential, A_z, for a set gauge. Integrating out the in-plane magnetic field components B_x and B_y over a given area allows values of A_z to be determined. The equipotential lines on a contour plot of A_z represent the in-plane magnetic field-lines, as for example in panels a) to c) of Fig. 4.1.

When the magnetic field is frozen into the plasma then

$$\frac{\partial A_z}{\partial t} = |\mathbf{V} \times \mathbf{B}|_z, \tag{4.1}$$

where $\mathbf{V}$ represents the plasma velocity and $\mathbf{B}$ is the magnetic field. Thus, changes in the magnetic field are facilitated entirely by advection rather than diffusion. In the case of magnetic reconnection, the frozen-in-condition is broken and changes in A_z by definition result in the generation of an electric field, according to

$$E_z = -\frac{\partial A_z}{\partial t}. \tag{4.2}$$

Since the topology of field-lines in 2D must change for reconnection to occur, field-lines must pass through a null-point, thus making the out-of-plane electric field at the X-point a reliable measure of the reconnection rate. This process is shown in panels a) to c) in Figure 4.1, where panel b) shows the electric field generated as field-lines break and change topology.

In the collisionless regime, the diffusion region is dominated by electron dynamics. Therefore, a means of identifying the reconnection mechanism in collisionless 2.5D simulations is to identify the terms in the generalised electron Ohm's law that sustain the out-of-plane electric field at the X-point, i.e.

$$\mathbf{E} = -\langle \mathbf{v_e} \rangle \times \mathbf{B} - \frac{\nabla \cdot \mathbf{P_e}}{n_e e} - \frac{m_e}{e}\frac{\partial \langle \mathbf{v_e} \rangle}{\partial t} - \frac{m_e}{e}(\langle \mathbf{v_e} \rangle \cdot \nabla)\langle \mathbf{v_e} \rangle, \tag{4.3}$$

where the terms on the right hand side are, from left to right, the advection term, the divergence of the electron pressure tensor, the time derivative of the electron bulk inertia and the convective inertia (i.e. spatial derivative) term, and where $\langle \mathbf{v_e} \rangle$ represents the mean electron particle velocity at the X-point. As shown in Ref. [82] a relativistic version of this equation can be derived from the relativistic Vlasov equation and is given by

$$\mathbf{E} = -\langle \mathbf{v_e} \rangle \times \mathbf{B} - \frac{\nabla \cdot \mathbf{P'_e}}{n_e e} - \frac{m_e}{e}\frac{\partial \langle \mathbf{u_e} \rangle}{\partial t} - \frac{m_e}{e}(\langle \mathbf{v_e} \rangle \cdot \nabla)\langle \mathbf{u_e} \rangle, \tag{4.4}$$

where $\mathbf{P'_e} = \int du_e((\mathbf{u_e}\mathbf{u_e}/\gamma)f - n_e\langle \mathbf{u_e}/\gamma \rangle \langle \mathbf{u_e} \rangle)$ and $\mathbf{u_e} = \gamma \mathbf{v_e}$, where γ is the Lorentz factor and f the electron velocity distribution function at the X-point. The reconnection mechanism in tearing-mode reconnection setups has been investigated in many computational studies [61, 75, 77, 147, 148] and was consistently found to be the divergence of the electron pressure tensor. A recent exception to this trend is found in Ref. [83], where it was shown that for tearing-mode reconnection in relativistic conditions (i.e. where inflow magnetic energy exceeds plasma rest mass energy), convective inertia can make an approximately equal contribution to the reconnection electric field as the pressure tensor divergence. A further exception is found in Ref. [82], where a sheared magnetic

field setup was modelled with a relativistic electron-positron plasma, and contributions from the time derivative of the electron bulk inertia were observed. In Ref. [77, 78] it is shown that for increasing values of guide-field in a tearing-mode setup, the convective inertial (spatial derivative) terms start to make an increasingly large contribution to the out-of-plane electric field adjacent to the current sheet. However, the contribution to the reconnection electric field at the X-point remained the divergence of the electron pressure tensor. In this chapter it is shown that similar results emerge in an open-boundary X-point collapse setup, with the notable difference that, for high enough guide fields, the convective inertial terms can become asymmetric across the current sheet and shift to the X-point, becoming the dominant contribution to the reconnection electric field.

A 3D representation of reconnection at an X-point with an out-of-plane magnetic guide-field is shown in panels d), e) and f) in Figure 4.1. As shown, reconnecting magnetic field-lines now carry a vertical magnetic field component. As explained in Ref. [96, 149], flux-tubes in 3D do not necessarily have to pass through an X-point/X-line in order to undergo reconnection. In 2.5D simulations however, all reconnecting field-lines must meet at the X-point, making this a representative model of the relevant dynamics. As the vertical components of the magnetic field are carried into the X-point, shown in panels d), e) and f) in Figure 4.1, the out-of-plane electric field at the X-point is now partially parallel to the magnetic field (see panel b)) and thus accelerated electrons are "guided" along the field-lines. Panels c) and f) of Figure 4.1 show the resulting electron current. As shown in panel c) this electron current represents a shear flow in the xy-plane. Ref. [150] discusses this effect and the resulting density asymmetry along the across the current sheet.

An alternative possible modification to a 2D tearing-mode reconnection setup is the addition of a shear flow parallel or anti-parallel to the in-plane magnetic field. This reconnection setup has been studied by several authors [38, 80, 81, 151] and is considered to be representative of reconnection and vortex formation in the magneto-sheath [152]. For shear flows where the shear velocity is below the Alfvén speed, the reconnection rate is shown to be to be inhibited by greater shear flows [80, 151]. However, for shear speeds greater than the Alfvén speed it has been shown that the reconnection dynamics can be altered and reconnection rate increased. 2D simulation results in Ref. [38] show that for large enough shear flows, tearing-mode reconnection can be coupled with vortex reconnection, and in Ref. [81] the parameters necessary for the mixing of these two reconnection modes are mathematically established.

In this chapter it is shown that for an open-boundary X-point collapse setup with a guide-field close to the strength of the in-plane field, electron shear flows are generated that are strong enough to change the reconnection dynamics and alter the term that

breaks the frozen-in condition. It was previously demonstrated that a large enough guide-field can lead to vortical electron flows and island formation in both tearing-mode reconnection [79] and in X-point collapse [144]. Here it is demonstrated how these results can be enabled by the shear flow and the resulting convectional inertia contribution to the reconnection electric field, generated through guide-field reconnection. Further, by exploring the same reconnection setup extended into the third dimension, it is investigated how electron and vortex dynamics proceed in 3D. While there is no generally accepted method of identifying vortices in a fluid [153], for this particular type of investigation we promote the use of the Q-value. The Q-value represents a Galilean-transformation invariant measure of vortical flow [154–156], defined as the second invariant of the velocity gradient tensor, $\nabla\mathbf{v}$, given by

$$\begin{aligned} Q =& (tr(\nabla\mathbf{v})^2 - tr(\nabla\mathbf{v}^2))/2 \\ =& \frac{\partial v_x}{\partial x}\frac{\partial v_z}{\partial z} + \frac{\partial v_x}{\partial x}\frac{\partial v_y}{\partial y} + \frac{\partial v_z}{\partial z}\frac{\partial v_y}{\partial y} \\ &- \frac{\partial v_x}{\partial y}\frac{\partial v_y}{\partial x} - \frac{\partial v_x}{\partial z}\frac{\partial v_z}{dx} - \frac{\partial v_y}{\partial z}\frac{\partial v_z}{\partial y}. \end{aligned} \tag{4.5}$$

When positive at a given point in a domain it indicates the presence of a vortical flow at that location or, as originally stated in Ref. [156], in "eddy zones" more than about 3/4 of the area has Q-values greater than 1. In this chapter the Q-value is used to show that vortical flows in 2.5D simulations correspond to three-dimensional vortex tubes with structures that are not apparent from the 2.5D simulations.

An additional possible feature, unique to 3D reconnection with a guide-field, is the generation of oblique modes as demonstrated in Ref. [103, 157, 158]. In 2.5D simulations of magnetic reconnection, reconnection must occur at a magnetic X-point, where it is possible for field-lines to change in topology. In a symmetric setup, this means reconnection occurs at the centre of the diffusion region (here along the x=0 line). However, in 3D reconnection with a guide-field, a more generic requirement for reconnection applies: reconnection occurs on surfaces where $\mathbf{k}\cdot\mathbf{B} = 0$, where k represents the wave vector of a perturbation associated with reconnection and B the magnetic field. In the case of a sheared magnetic field with a guide-field, extended over a 3D domain, this implies that reconnection sites may exist adjacent to the midplane of the diffusion region, generating current sheets at oblique angles, relative to the z-direction, of

$$\theta = \pm\arctan(k_z/k_y) = \pm\arctan(B_y/B_z). \tag{4.6}$$

The angle θ does thus correspond to the inclination of the out-of-plane magnetic field. In a sheared magnetic field reconnection setup the strength of B_y increases with distance from the midplane of the diffusion region, meaning that reconnection sites further from

the centre should lead to greater obliqueness. While the generation of oblique current sheets and flux-tubes has been demonstrated in 3D Particle in Cell simulations with tearing-mode setups Ref. [103, 158], this chapter similarly demonstrates the oblique nature of vortex dynamics in 3D reconnection in an alternative reconnection setup, i.e. X-point collapse.

4.2 Simulation model

alues of current, density and magnetic field do not vary with z.

As described in section 2.2 the set-up of the in-plane magnetic field used here in known as X-point collapse. Following Chapters 2 and 3, this chapter continues the investigation of X-point collapse using a relativistic and fully electromagnetic Particle In Cell (PIC) code. However, while in previous chapters simulation runs were limited to 2.5D, here results were extended into 3D. The PIC code used was EPOCH, as described in Section 2.2.2. Being a kinetic and relativistic code, all the relevant physical quantities are represented, allowing for the calculation of all the terms in the generalised Ohm's law (see Eqn. 4.4).

As in previous simulations (see section 2.2), in the 2.5D case, lengths of grid cells were set as the Debye length, i.e. $\Delta x = \Delta y = \lambda_D$, over a grid of 400×400 cells, amounting to a system length of approximately four ion inertial lengths, i.e. $L = 4c/\omega_{pi}$. While the system size does not extend to characteristic coronal lengths scales, it is large enough to capture both particle species dynamics. 500 pseudo particles per cell were used which was shown to be a suitable number in convergence tests. When extended into 3D, the height of the simulation box was set to half the simulation width, i.e. $L_z = 0.5L$. The size of grid cells was set to 2 Debye lengths, i.e. $\Delta x = \Delta y = \Delta z = 2\lambda_D$, making up a grid of $200 \times 200 \times 100$ cells, using 200 particles per species per cell. While this is less computationally reliable than the 2.5D simulation runs, it will be shown that a strong correspondence exist between both setups.

The choice of boundary conditions in a pure X-point collapse configuration is not trivial. Unlike in tearing-mode type reconnection, it is not possible to apply periodic boundary conditions, since field-lines at opposite boundaries are not equidirectional. In Chapter 2, two types of boundary conditions, open and closed, were used and compared. In the open case it was demonstrated that the system allowed for greater reconnection rates and for a smoother system evolution when guide-fields were applied. Further, in the open case, for guide-field strengths close to the in-plane field, the reconnection dynamics significantly changed. Magnetic islands and electron flow vortices start to emerge. For these reasons the open boundary case was chosen for this investigation.

When extending the 2D simulation into 3D, the previously ignorable direction (z) now requires well defined boundaries. These were set as periodic.

4.3 Reconnection mechanism and dynamics for varying strengths of guide-field in 2.5D

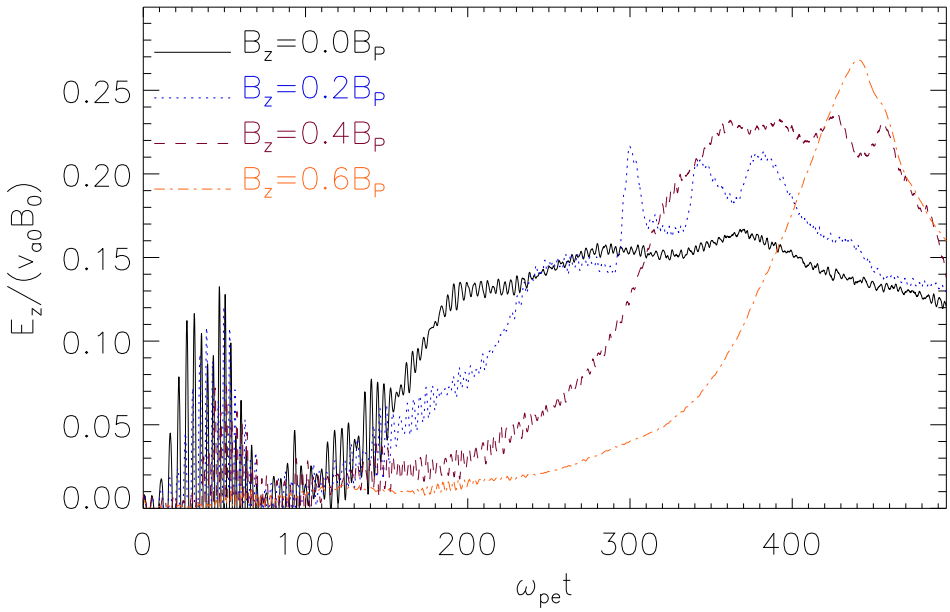

FIGURE 4.2: The reconnection electric field at the X-point for 2.5D simulation runs, with guide-field strengths as indicated.

Reconnection setups for guide-field strengths of up $0.6B_P$ were run until $500\omega_{pe}$. In Ref. [144] it was shown that peak reconnection was reached for all guide-field cases within this time. Figure 4.2 shows the out-of-plane electric field (E_z) at the X-point for 2.5D runs with different values of guide-field, representing the reconnection rate according to Eqn. (4.2). As discussed in the previous work, a greater guide-field leads to increasingly delayed onsets of reconnection. Ref. [144] also addresses the initial periods of intense high-frequency oscillations, linked to oscillatory reconnection. In the $0.6B_P$ guide-field case, a magnetic island, and thus a secondary X-point, emerges. Rather than plotting both reconnection rates, E_z from the X-point with the greater reconnection rate is used. As shown, the reconnection rate in the $0.6B_P$ briefly exceeds the reconnection rate in all other cases. This occurred shortly after the emergence of the second X-point. It is to be noted that the locations of the X-point here were tracked and E_z was sampled at those locations, whereas in Fig. 2.4 E_z was simply sampled at the centre of the simulation

domain. Since the X-point starts to move for $B_{z0} = 0.6B_P$, tracking of the X-point location becomes necessary to accurately measure the reconnection rate.

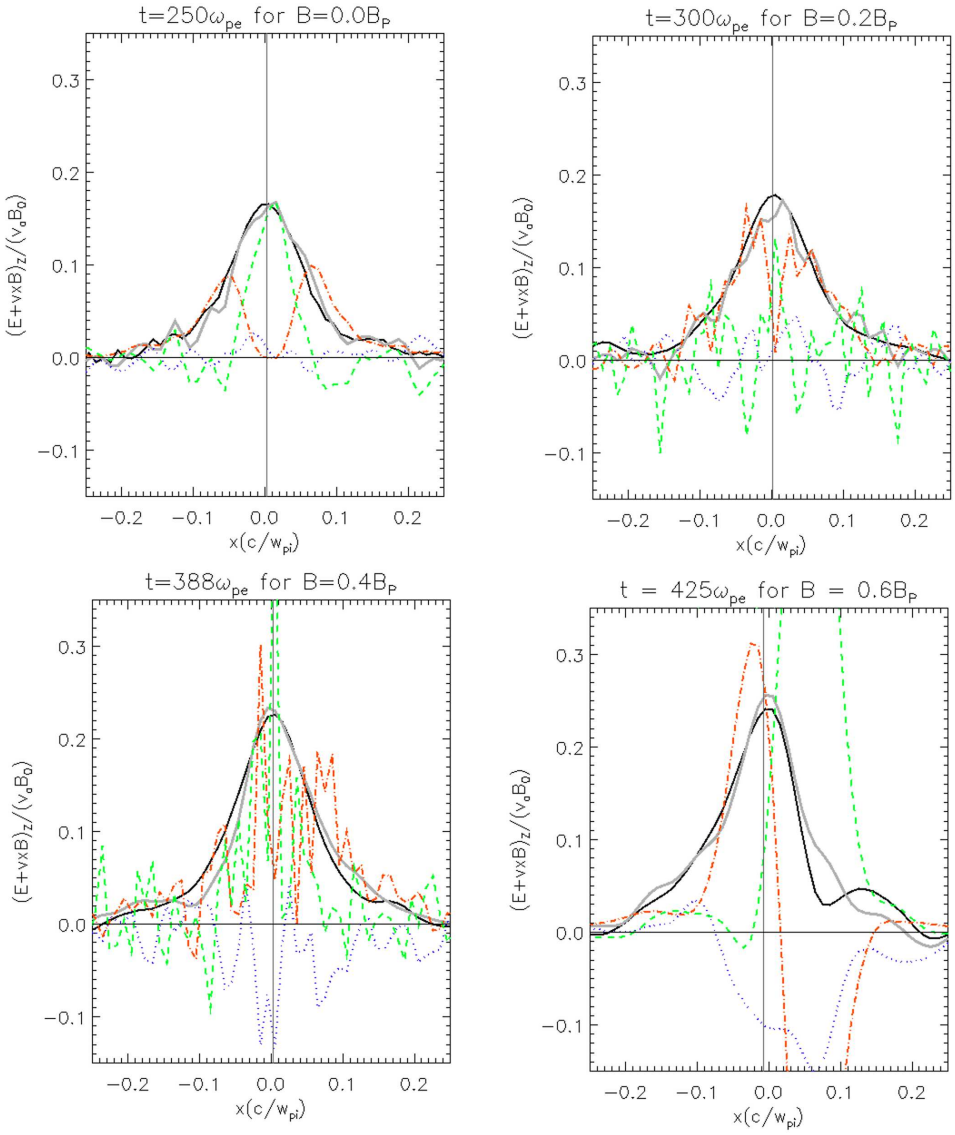

FIGURE 4.3: Plots of the contributions of different terms in the generalised Ohm's law to the out-of-plane electric field along cuts through the current sheet along the x-axis through X-point. The vertical line in each plot marks the horizontal position of the X-point, as determined by tracking the magnetic null. Solid black lines show the out-of-plane electric field (not including the advective electric field component), green dashed lines show the contribution of the divergence of the pressure tensor, red dashed-dotted lines show the contribution of the convective inertia, and blue dotted lines show the contribution from the rate of change of bulk inertia. Solid grey lines represents a summation of the contributing terms.

Changes in the shape of the current sheet and reconnection region with increasing guide-field in X-point collapse are discussed in Ref. [144]. However, it was not investigated how these changes affected the reconnection mechanism, which is one of the goals of this investigation. Similarly to Ref. [77], cuts were made through the widths of the current

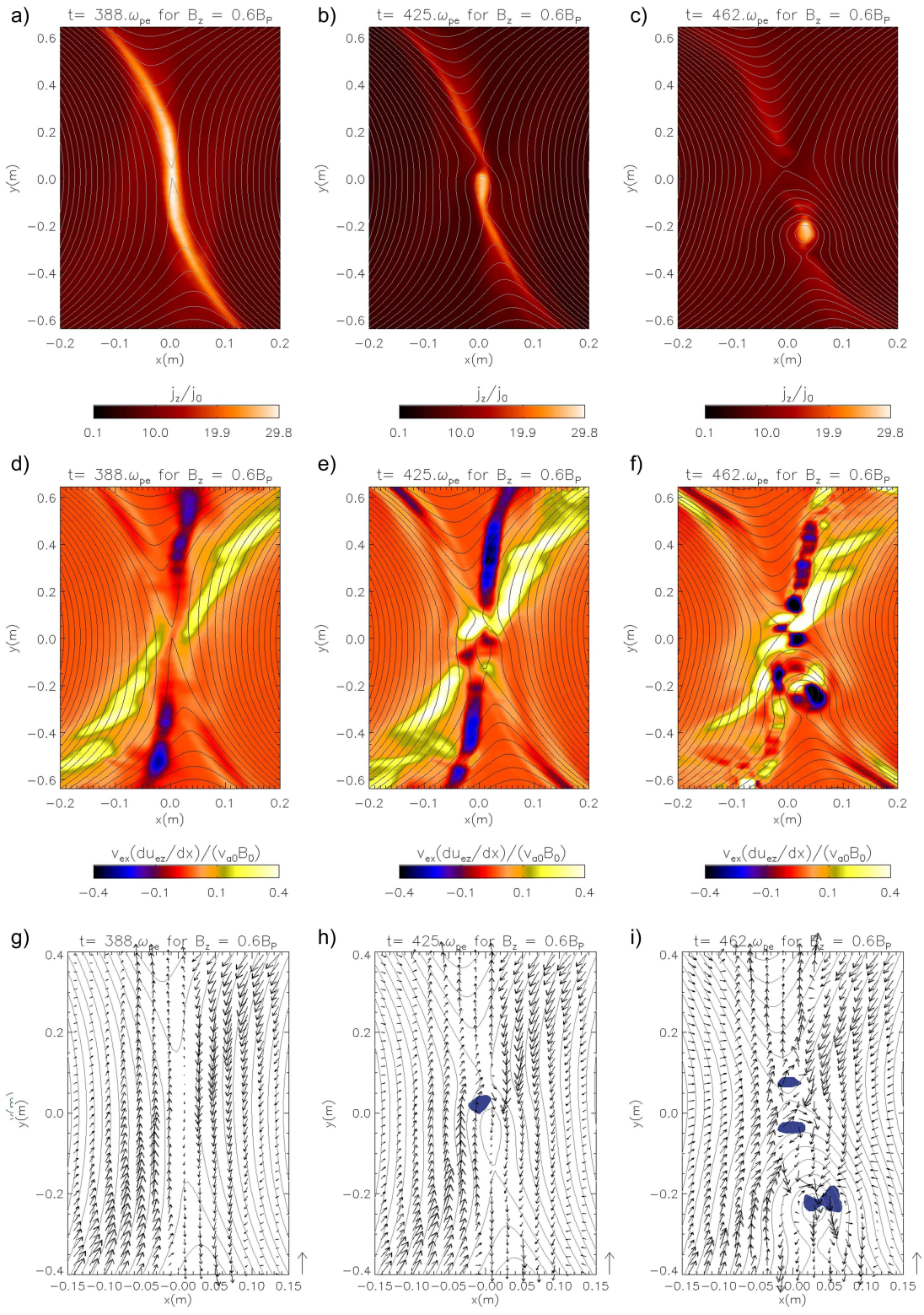

FIGURE 4.4: The three consecutive rows of plots show the time progression the current density, the dominant component of the convective inertia, $v_{ex}\frac{du_{ez}}{dx}$, and the Q-value respectively. Superimposed on all plots is the in-plane magnetic field, and panel g), h) and i) also show electron velocities as well as coloured areas where the Q-value is greater than zero, indicating the existence of a vortex. The lengths of the arrows next to the plots represent the greatest speeds reached, in each panel approximately 0.22c, i.e. $2.2v_{ae0}$. The simulation times, indicated on top of individual panels, were chosen around the occurrence of island and vortex formation.

sheet, at the X-point, to show E_z at locations along the reconnection region. The terms in the generalised Ohm's law contributing to E_z were calculated. Since for greater guide field cases, electron speeds in the simulation reached increasingly relativistic speeds (see section 4.5), the modified Ohm's law (see Eqn. (4.4) was used. For each guide-field case, cuts were taken when peak reconnection was reached, as shown in Fig. 4.3. This progression of plots shows that, for greater guide-fields, the convective inertial contributions become increasingly asymmetrically distributed relative to the X-point. This can be interpreted as shear-flows tilting the flow across the diffusion region but not quite forming a vortex. The pressure tensor terms remain the dominant contribution at the X-point up to guide-field strengths of $0.4B_P$, but their area of influence gets increasingly narrow. This can be understood in terms of the increased shear flow: As the electron flow speed along the current sheet increases, electrons that normally would have been undergoing meandering motion in the diffusion region (i.e. adding to the pressure-tensor tensor contribution) are now accelerated outwards and thus contribute to the convective inertial term instead. This is in line with the theoretical prediction stated in Eqn. 4 in Ref. [48].

In the case of a guide-field of $0.6B_P$, a shift in the previously observed dynamics occurs. After the formation of a magnetic island, and thus a secondary X-point, a significant contribution to the reconnection electric field is made up by the convective inertia term. As shown in the final panel of Fig. 4.3, both the pressure tensor and convective inertia contributions to the electric field are now highly asymmetric across the current sheet along the lower X-point (interestingly this asymmetry is reversed at the upper X-point). This change in dynamics is coupled with the emergence of an electron flow vortex in the proximity of the X-point. Fig. 4.4 shows the time evolution of the relevant quantities during this shift of dynamics. Closer analysis shows that the convective inertial contribution to the reconnection electric field at the X-point is mainly provided by the component $v_{ex}\frac{du_{ez}}{dx}$. Panels d), e) and f) of Fig. 4.4 show the evolution of this term superimposed on the in-plane magnetic field. As shown in panel d), which corresponds to a time shortly before the reconnection peak, this contribution initially plays a role only adjacent to the current sheet, similar to the contributions of the convective inertia in panels a), b) and c) in Fig. 4.3. However, as shown in panel e) of Fig. 4.4, this contribution shifts to the location of the X-point and also the location where the secondary X-point is formed, thus playing a role at both reconnection sites.

Fig. 4.4 panels a), b) and c) shows the evolution of the out-of-plane electron current density (j_z) and the in-plane magnetic field. As shown, after the formation of the magnetic island, a strong current starts to develop at its centre. This can be attributed to the compression of the magnetic field, and thus increased curl of the magnetic field, due to the continued reconnection at the two X-points, as explained in Ref. [159]. Further,

in panels g), h) and i) of Fig. 4.4 the electron motion at the same time steps is shown, as contour plot of the Q-value. This value represents a Galilean-transformation invariant measure of vortical flow [154–156], defined as the second invariant of the velocity gradient tensor, $\nabla \mathbf{v}$, given by equation 4.5. When greater than zero, the Q-value indicates the existence of a vortex. While in panel g) there exist only a shear flow, as predicted by the nature of guide-field reconnection, in panel e) it can clearly be seen that a vortical flow emerges in the vicinity of the X-point. The vortex visible in the velocity field and the Q-value show good correspondence. Thus, panels b), e) and h) demonstrate that in this reconnection simulation, an increased reconnection rate, and the emergence of a secondary X-point, is brought on by a convective inertial contribution to the reconnection electric field, which is coupled to the emergence of an electron flow vortex. This strongly suggests that the vortex reconnection mode, as described in Ref. [38, 81], rather than only X-point collapse, facilitates the reconnection process. As shown by the arrows on the panels, electron flow speeds exceed the electron Alfvén speed (0.1c), as is required for an increase in reconnection rate due to vortex interaction to occur [80, 151]. Panel f) and i) show the state of the convective inertia contribution and electron motion shortly after peak reconnection. As shown, multiple vortices have formed spreading in a somewhat chaotic fashion along the current sheet. The 3D equivalent of this outcome is investigated in section 4.4.

4.4 Reconnection Dynamics in 3D

As described in the previous section, the reconnection dynamics of a standard X-point collapse simulation are significantly altered by the inclusion of an out-of-plane guide-field of a strength close to the in-plane field, i.e. $B_z = 0.6B_P$. While the formation of a vortex and magnetic island occurred in a straight-forward fashion when the system reached peak reconnection rate, shortly after the system developed into a chaotic state. To see what these dynamics may correspond to in a real reconnection event, the ignorable direction z was extended out-of-plane to make a 3D reconnection setup. While an analysis of the term breaking the frozen-in condition was not possible here, because no universally agreed definition of 3D reconnection rate exists, finding similar dynamics to the 2.5D case would represent strong evidence that a similar shift from X-point collapse to vortex induced reconnection occurred.

Fig. 4.5 shows the time progression of electron current density and the Q-value, representing electron flow vortices. The snapshots for the panels in Fig. 4.5 were taken to show the progression of island and vortex formation, which occurred slightly earlier than in the 2.5D case. The electron current density is represented by an isosurface (i.e.

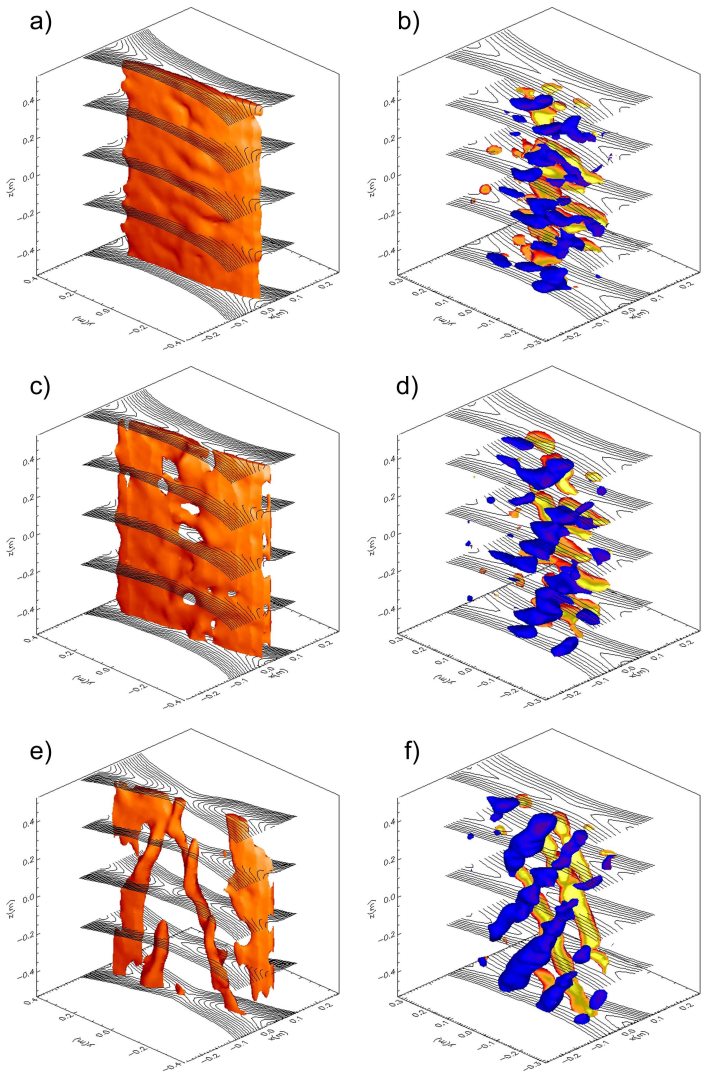

FIGURE 4.5: In the vertical direction, panels a), c) and e) show the time evolution the 3D out-of-plane current density (j_{ez}) at $t = 337\omega_{pe}, t = 362\omega_{pe}$ and $t = 387\omega_{pe}$. Current density is represented as an isosurface of 2/3 the maximum current density at the respective time. Again, in the vertical direction, panels b), d) and f) show isosurfaces of the Q-value (see Eqn. (4.5)) at the same times in the simulation. For clarity, isosurfaces left of the current sheet are coloured in blue and isosurfaces right of the current sheet are coloured in yellow. In all panels, in-plane magnetic field-lines are superimposed on flux-tubes, showing the magnetic field at several horizontal slices through the simulation box. The simulation times shown were chosen around the time of island/vortex formation, which occurred slightly earlier in the 3D case.

a surface of a where the current density is of a constant value) of values approximately two-thirds of the maximum current density at each snapshot. As shown in panel a), at first the current density has the shape of standard current sheet, as would be the case for zero guide-field. However, in panel c) the current sheet starts to fragment, eventually leading to a tubular structure as shown in panel e). Similarly to the 2D case, the locations of elevated current density correspond to the centre of a flux-tube, which have been shown to be the 3D equivalent of magnetic islands [160], where magnetic fields are compressed and currents are increased [159]. Interestingly, while the initial fragmentation in panel c) appears to be random, the final isosurface shows a distinct tubular structure. Further, rather than connecting back on itself, as would be the 3D equivalent of panel c) in Fig. 4.5, the current density is tilted along the y-axis, similarly to studies of 3D reconnection with a guide-field in a tearing-mode setup [103].

A further difference in the 3D results can be seen in the evolution of the Q-value, as shown in Fig. 4.5, panels b), d) and f). Each snap-shot shows two isosurfaces where the Q-value exceeds zero. Yellow shows the isosurfaces for positive Q-value on the right hand side of the diffusion region (i.e. right of the x=0 line), while the blue isosurfaces correspond to positive Q-values on the left hand side of the diffusion region. This distinct colour scheme was chosen to clearly represent the arrangement of vortical flows throughout the simulation domain. Panel b) represents the initial instance of vorticity, and, as for the current density, there initially appears to be no distinct structure. However, as seen in panel f), eventually two sets of distinct vortex tubes emerge on each side of the diffusion region, tilted in opposite directions. Again, this represents a structure that could not be adequately represented in a 2.5D simulation, and only the 3D simulation reveals the orderly, realistic dynamics. This gives new insight into panel i) of Fig. 4.4, as this apparently disordered arrangement of vortical flows actually corresponds to well-defined structure in 3D. The motion of the vortex tubes in the plane appears to be in the opposite direction of the in-plane shear flow along the current sheet, which seems to contradict basic theoretical considerations of the motions of vortex tubes in shear flows [161]. However, this is in fact a misconception as the vortex tubes move downwards, along with the bulk electron current flow. Due to their inclination relative to the z-axis the illusion of motion in the xy-plane is created.

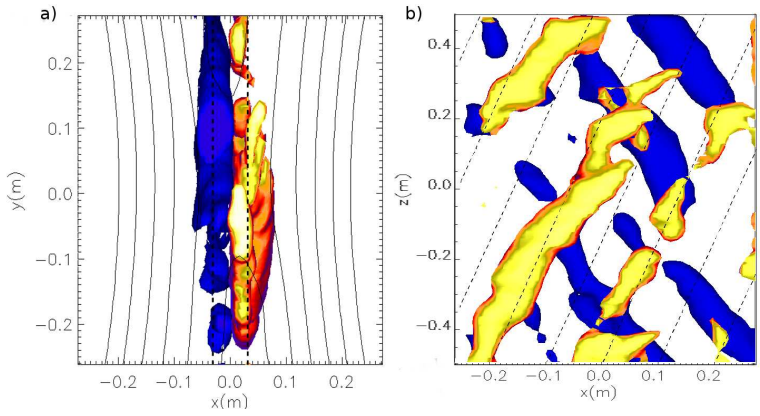

FIGURE 4.6: As in Fig. 4.5 panel f), showing vortical flows in 3D simulation runs with a guide field of $0.6B_P$ according to the Q-value at $t = 387\omega_{pe}$. Panels use perspectives as indicated by axes. In panel a), the dashed lines signify the distance of vortex tubes from the centre of the domain and thus from the centre of the diffusion region. Dashed lines in panel b) are inclined at the calculated value of θ, based on Eqn. 4.6, and show a strong correspondence with the inclination of vortex tubes.

Following the analysis of tilted (oblique) current sheets in Ref. [157], panel a) of Fig. 4.6 shows vortex tubes as they appear in the xz-plane. Dashed lines on plots signify the locations of vortex tubes, which are shown to be left and right of the centre of the domain. By taking the mean value of the strengths of the sheared magnetic field, B_y, and the magnetic guide-field, B_z, at these locations, a prediction for the angle of the

oblique modes, according to Eqn. 4.6, is found to be $\theta = \pm 16°$. Panel b) of Fig. 4.6 shows vortex tubes, as they appear in the yz-plane. Here, dashed lines in the plot are inclined at the calculated value of θ, effectively representing the inclination of the out-of-plane magnetic field. As shown, there exists a clear correspondence between the tilt of the vortex tubes and θ. Unlike in Ref. [103, 157, 158], where a tearing-mode setup is used, it is not possible in X-point collapse to relate the locations of oblique structures to initial simulation parameters since X-point collpase is inherently time dependent and the width and shape of the diffusion region is not fixed by the setup. Further, as there is no asymptotic magnetic field, there is no limit on the angle of obliqueness. However, by taking the B_y profile across the diffusion region during vortex formation to be of the form $B_0' x/\lambda$, where λ is the half-width of the diffusion region, and noting that B_z across the diffusion region is approximately constant, while $B_y \approx B_z$ at the diffusion region edge, we arrive at a distance relation similar to Ref. [157], given by $x_s = \lambda \tan(\theta)$. This gives the distance of the oblique vortex tubes from the centre of the domain as $x_s = \pm 0.3\lambda$. In physical distance, this equates to approximately $x_s = \pm 0.03m$, based on the measured width of the diffusion region, and is a good match as shown in panel a) of Fig. 4.6.

4.5 Particle distribution function dynamics

Fig. 4.7 shows the distribution functions for electron particle velocities in the 2.5D simulation runs for different guide-field cases. Electrons and ions initially have opposite velocities in the z direction and are oppositely accelerated by the reconnection electric field. In each case, the three lines on the plot show velocity distributions at the start of the simulation, velocity distributions at peak reconnection and at the end of the simulation.

It can be seen that for greater guide-field cases, increased out-of-plane electron acceleration is observed. In the $0.6B_P$ guide-field case a bump-on-tail distribution in v_{ez} emerged at peak reconnection, stretching into the relativistic regime, and subsequently flattened out again. A similar effect was observed in simulations in Ref. [62], Fig. 6, when an increased stress parameter of $\alpha = 2.24$, was used in a 2.5D simulation of closed boundary X-point collapse. This indicates that there is an equivalence to using greater initial guide-fields and greater initial stress in the in-plane magnetic field.

While electrons in the zero guide-field case experience lesser acceleration in the z-direction, the acceleration of ions is in fact greater, leading to a slight bump in v_{iz}. However, the acceleration of ions in the y-direction in the $0.6B_P$ guide-field case greatly exceeds that in the zero guide-field case. This implies that ions are moved out of the

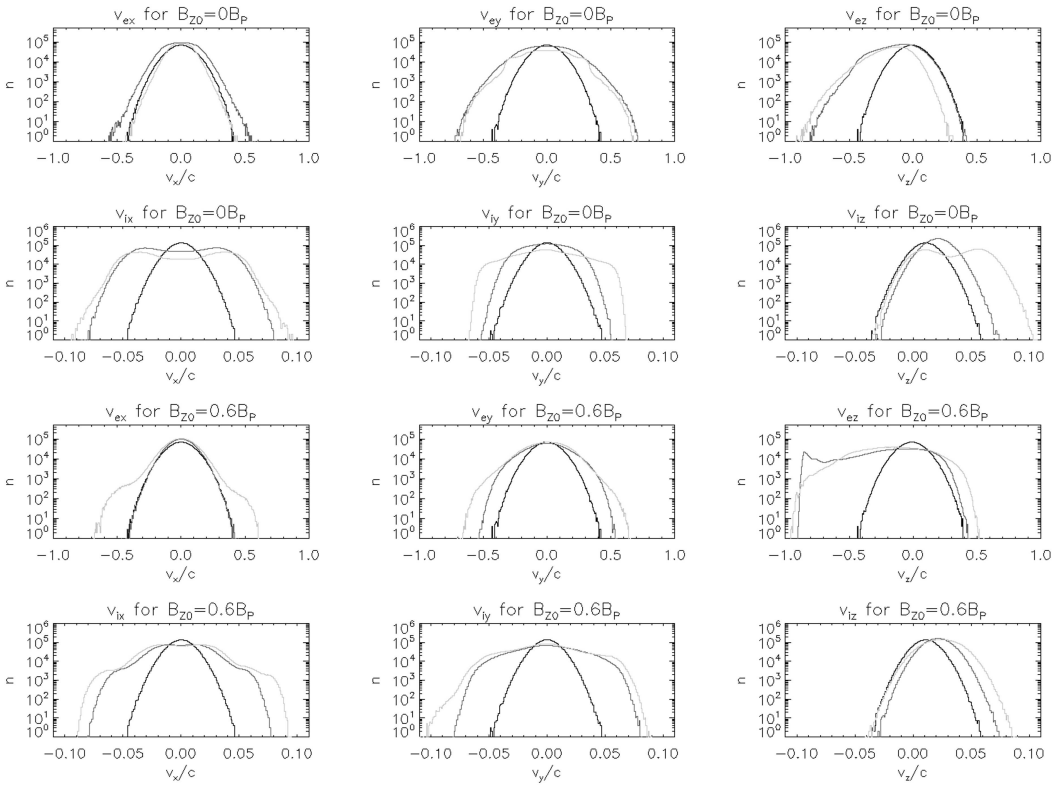

FIGURE 4.7: Panels show as indicated the electron and ion particle velocity distribution functions for guide-field cases of $0B_P$ and $0.6B_P$ in the 2.5D simulation runs. Black lines show the distribution functions at the beginning of the respective simulation. Dark grey lines show the distribution functions at peak reconnection, i.e. $t = 250/\omega_{pe}$ for zero guide-field and $425/\omega_{pe}$ for the $0.6B_P$ guide-field case. Light grey lines show distribution functions at the end of the simulation, i.e. $t = 500/\omega_{pe}$. Particles included in the plots were chosen from an area around the diffusion region, i.e. $(-2c/\omega_{pe}) < x < (2c/\omega_{pe})$ and $(-8c/\omega_{pe}) < y < (8c/\omega_{pe})$.

diffusion region faster in the $0.6B_P$ guide-field case and thus experience less out-of-plane acceleration by the reconnection electric field, which explains the reduced acceleration in the z-direction.

Equivalent results for 3D simulation runs are shown in Fig. 4.8. While it was not possible to determine the time of peak reconnection in this case, intermediate time steps for the distribution function were chosen to be the points when the reconnection current reached a peak value, which was shown to approximately correspond to peak reconnection rates in 2.5D simulations of X-point collapse [144]. For high guide-fields, peak current was reached sooner in the 3D case than in the 2.5D case, as is consistent with the earlier onset of vortex formation. Although time-scales of processes were affected, the resulting distribution functions are notably similar, including features such as the bump-on-tail distribution in the out-of-plane electron velocity in the high guide-field case. This result shows that, while different dynamical features can emerge in the 3D case, a high degree of correspondence exists in the bulk particle acceleration.

While there are some differences in the plots, these appear to be the result of a mismatch in the simulation times of snapshots considered. For example, v_{iz} in the low guide-field case and v_{ez} in the high guide-field case seem to vary only in the intermediate distribution function, while the initial and final distributions take on mostly the same shape. They thus show the same progression shifted in time. For v_{ex} in the high guide-field case two distinct bumps appear in the final snapshot of the 2.5D simulation, while in the 3D case they have already thermalised by the time of the final snapshot, again showing that reconnection proceeds slightly faster in 3D.

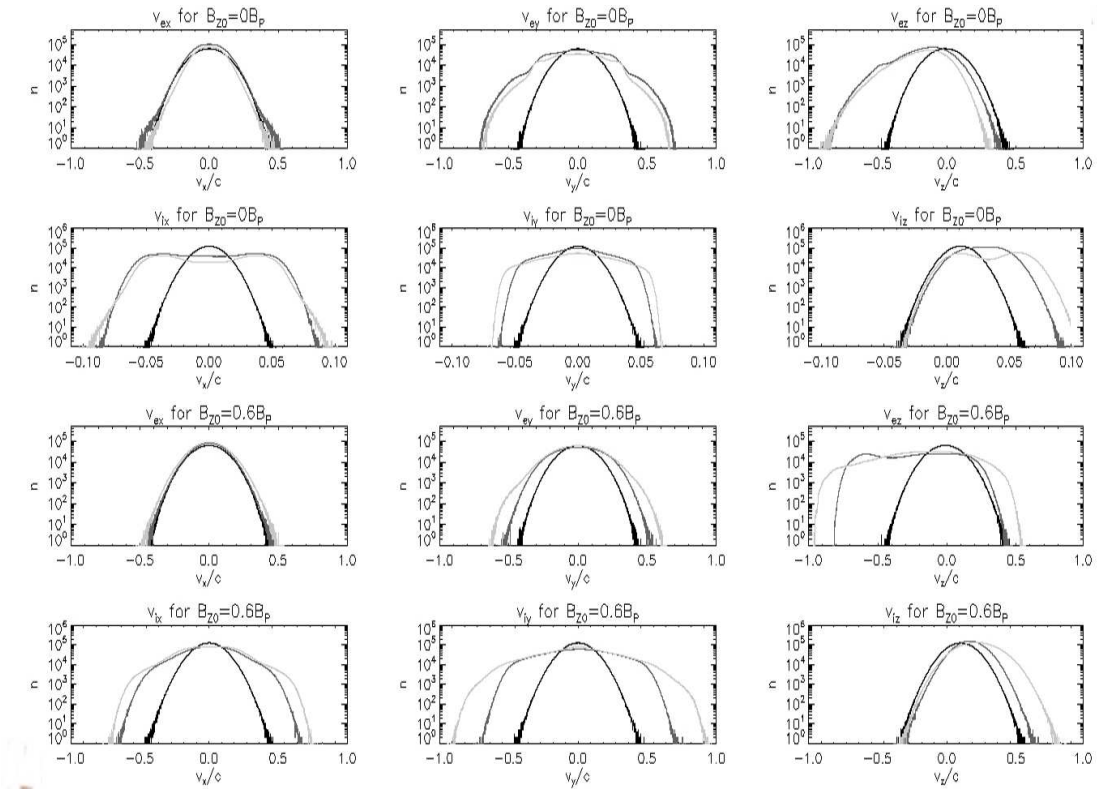

FIGURE 4.8: Panels show as indicated the electron and ion particle velocity distribution functions for guide-field cases of $0B_P$ and $0.6B_P$ in the 3D simulation runs. Black lines show the distribution functions at the beginning of the respective simulation. Dark grey lines show the distribution functions when peak reconnection currents were reached, which occurred in both guide-field cases at around $t = 375/\omega_{pe}$. Light grey lines show distribution functions at the end of the simulation, i.e. $t = 500/\omega_{pe}$. Particles included in the plots were chosen from an area around the diffusion region, i.e. $(-2c/\omega_{pe}) < x < (2c/\omega_{pe})$ and $(-8c/\omega_{pe}) < y < (8c/\omega_{pe})$.

4.6 Conclusions

By studying X-point collapse with open boundary conditions and an out-of-plane guide-field close to the strength of the in-plane field, new insights have been gained into the

specifics of reconnection dynamics. Using 2.5D simulations it was shown that reconnection dynamics were significantly altered due to the increased induced shear flow. It was shown that, while the increased guide-field initially suppressed the reconnection rate, later in the simulation a brief period of peak reconnection was attained where the reconnection electric field exceeded that of lower guide-field cases. The reconnection electric field at this point was substantially supported by the convective inertia term in the generalised Ohm's law, rather than the divergence of the pressure tensor (see Fig. 4.3). This stands in stark contrast to previous studies of tearing-mode reconnection with a guide-field, where no change in the reconnection mechanism was observed. The shift in reconnection mechanism during peak reconnection coincided with the formation of a secondary X-point, as well as an electron flow vortex (see Fig. 4.4). It is concluded that, due to the induced shear-flow along the current sheet, vortex-induced reconnection takes effect, allowing for the change in reconnection dynamics.

While particle velocity distribution functions show that bulk particle acceleration proceeds in a similar fashion in 2.5D and 3D simulations (see Section 4.5), in the high guide-field case 3D structures emerged that are not present in the 2.5 simulation. At later simulation times in the 2.5D simulation the vortical flows took on an apparently chaotic shape. However, when the simulation setup was extended into 3D geometry, vortical flows where shown to self-assemble into oblique 3D tubes, taking on a distinct structure that cannot be represented in a 2.5D simulation (see panel (f) of Fig. 4.5). Similarly, magnetic flux-tubes (i.e. magnetic islands in 2D) and tubular regions of elevated current density appeared to be sheared along the z-direction. It was shown that the tilt angles of the vortex tubes correspond well with predictions for tilts due to oblique modes, as discussed in Ref. [103] (see Fig. 4.6). As oblique modes are suppressed in 2.5D simulations, this further shows that the emergent structure observed is unique to the 3D case.

Since purely 2D reconnection setups are an unlikely occurrence in nature, guide-field reconnection setups, and their induced shear flows, are important aspects of the study of magnetic reconnection and are likely to be needed to accurately model reconnection scenarios in the solar corona and the Earth's magnetosphere. As discussed in Ref. [152], vortex formation due to shear flow have already been observed in the Earth's magnetosheath. We hope the results of this study may further the progress in this field and other studies of reconnection where guide-fields could lead to large shear flows. We hope to inspire the further investigation of vortical flows in in-situ observations to see if there may be correspondence to the 3D structures found in this investigation.

Chapter 5

Summary and Conclusions

5.1 The observational features of X-point collapse and tearing-mode reconnection in 2.5D

Since Sonnerup's initial formulation of the quadrupolar field of magnetic reconnection there has been no attempt to extend upon this out-of-plane magnetic signature of magnetic reconnection. In the works presented in this thesis it was shown that a great wealth of additional magnetic field structure can be exhibited in certain simulation setups. Particularly in closed-boundary X-point collapse it was demonstrated that, instead of a quadrupole, an octupolar out-of-plane magnetic field emerges in the diffusion region, where the outermost components correspond to the ion currents. Despite two orders of magnitude in difference of electron and ion masses, the out-of-plane magnetic field components generated by ion flows are of the same order as those by electrons, regardless of simulation size, and scale with the ion diffusion region size. This indicates that this effect is likely to occur in real plasma under a comparable setup.

Further, by applying the same analysis to a tearing-mode reconnection setup, it was shown that the effect was not limited to X-point collapse, but to regions on reconnection sites where the trajectories of ions are strongly curved. For a purely sheared magnetic field, it was shown that, due to geometric considerations, additional out-of plane magnetic structure was only generated in the out-flow region, where ion motion was more strongly diverted. However, in both field configurations it was shown that the detection of additional magnetic out-of-plane structure is detectable by a satellite mission and should accordingly be accounted for in data analysis.

A further observational signature that appears to be unique to X-point collapse is the generation of high frequency out-of-plane electric field oscillation at the X-point and

EM wave generation, prior to reconnection onset. This appears to be caused by a brief period of oscillatory reconnection before the formation of the current sheet. Oscillations shift from the plasma frequency to the upper-hybrid frequency and correspond to the ordinary and the extraordinary mode on the plasma wave dispersion relation diagram. A similar type of emission has been observed in radio waves in solar radio burst fine structure spikes. The exact nature of the generation of this emission and its relevance to natural sources is to be a matter of further investigation.

5.2 Effects of boundary conditions and guide-field on X-point collapse reconnection dynamics in 2.5D

Two methods of maintaining a X-point collapse configuration in collisionless PIC simulation were explored by means of the two different sets of boundary conditions: firstly a closed system was used, where super-particles and electromagnetic radiation are prevented from escaping. This was accomplished by reflecting super-particles reaching the boundary, and by imposing zero-gradient boundary conditions on both the electric and magnetic fields in the x- and y-directions and forcing the tangential component of electric field to zero, while the normal component of the magnetic field was kept constant. This setup further determined that the points where magnetic field-lines meet the boundary (i.e. foot points of flux-tubes in 3D) are fixed and thus restrain the geometry of the reconnection region. In the second setup open boundary conditions were used, allowing electromagnetic radiation and super-particles reaching the boundary to escape for the system. In order to accomplish this super-particles reaching the boundary were removed form the system and an algorithm was applied to cancel out electromagnetic field oscillations at the boundary. A further effect of these boundary conditions is that the initial magnetic field strength parallel to the edges of the simulation domain was maintained, such that the saddle configuration of the magnetic vector potential was maintained throughout the simulation, imposing an X-point like field configuration.

In the absence of a guide-field, both cases behave relatively similarly, although the closed case is shown to exhibit a faster onset of reconnection, as well as a more dynamic reconnection rate. That is to say, after reaching a peak value, the reconnection rate in the open case went on steadily, whereas the one in the closed case it dropped and rose again. This evolution underlines the fundamental difference between the boundary cases: one allowing free magnetic field evolution while the other limits the amount of reconnected flux. Both boundary type simulations exhibited many of the established features of 2.5D reconnection observed in tearing-mode setups, including the formation of current sheets, a quadrupolar out-of-plane magnetic field, and it was shown that the

term in the generalised Ohm's law, providing the reconnection electric field was the divergence of the electron pressure tensor.

When employing out-of-plane guide fields it was shown that for the closed boundary case, reconnection was greatly inhibited and sporadic, even for small guide-fields. In the open case, changes in reconnection rate remained smooth and increasing values of guide-field lead to increasingly delayed onsets of reconnection and shear flows along the current sheet developed, as has been demonstrated in tearing-mode reconnection. For a guide-field close to the strength of the in-plane field however, a transition in the reconnection dynamics occurred. A second X-point emerged, creating a magnetic island between it and the original X-point, as well in-plane vortical electron flows, which were studied using their Q-value. Further, the component supporting the reconnection electric field shifted to the spatially dependant inertial term, marking distinct transition in the reconnection physics. It is concluded that the increased shear flow due to the guide-field, which was now significantly in the relativistic regime, resulted in the onset of vorticity induced reconnection, causing the observed changes in dynamics.

5.3 The 3D structure of the X-point diffusion region

By extending the open boundary case into the third spatial dimension, for both zero and the high guide-field case, a clearer understanding of the true reconnection dynamics was gained and non-trivial changes were demonstrated in the high guide-field case. While the zero guide-field case exhibited no significant structural changes, the vortices that emerged in the high guide-field case in 2.5D now took the form of vortex tubes at oblique angles, parallel to the magnetic field. The vortex dynamics, which appeared chaotic in the 2.5D case now took and orderly shape in the form of two tubes at opposite sites of the current sheet, tilted in opposite directions. It is concluded that this 3D structure is of a similar nature to oblique current-sheets, generated by oblique tearing-modes in 3D Harris-current sheet type setups. Nevertheless, velocity distribution functions compare well, between the 2.5D and the 3D case, showing that bulk dynamics is mostly the same.

Chapter 6

Discussion

The works in this thesis are based on a vast body of theoretical and numerical modelling of efforts of magnetic reconnection, as well as observation of relevant physical effects in nature and laboratory experiment. The goal was to both extend and complete the existing framework by studying a regime that had previously been overlooked, i.e. X-point collapse. During this process, a number remarkable new physical features were discovered, as well as many similarities to previous simulations using different setups.

While the work presented in this thesis is both original and unique, it effectively represents a piece in the puzzle of complete understanding of the reconnection process in nature and its role in the dynamics of the solar atmosphere. However, several conclusions can be drawn about that have general implication to the field of solar coronal physics:

- X-point collapse was shown to be a viable mode of fast reconnection with unique features. As such interpretation of physical reconnection events should not be limited to comparisons with tearing-mode reconnection simulations, which has been a common practice up to date.
- New observational signatures of reconnection have been discovered, adding to the means by which reconnection can be identified in nature, such as in the Earth's magnetotail, and it is important that those working in observation and data analysis are aware of them.
- It was concluded in previous studies that the effect of guide-field on magnetic reconnection does not have an effect on which term in the generalise Ohm's law is sustaining the reconnection electric field. This conclusion has been challenged here, as it was shown that a sufficiently large guide field can drastically alter the reconnection process. This effect should be accounted for by the solar physics

community when planning further simulations, and more importantly when interpreting observational or experimental data. Further, the relevance of this effect in solar-flare triggers is to be considered.

- Several numerical and analytical tools have been used in this study, which are uncommon in the field of solar physics. With the works presented here, it is hoped that the the use of flux-conserving boundary conditions, as well as the use of the Q-value for vortex detection, borrowed from fluid dynamics, will become more common within numerical works in the solar community.

There are a number of ways in which this investigation could be extended. Future works on this subject may include:

- X-point collapse in this study was modelled in a purely symmetric setup. Several studies of tearing-mode reconnection have demonstrated the importance of initial asymmetric particle densities across the current-sheet (e.g. [162, 163]). Simulations could be extended to investigate these effects.

- The discovery of electromagnetic wave generation preceding the onset of quasi-steady reconnection in X-point collapse, as discovered in the simulations presented, could be of importance to observable reconnection signatures, and should be studied in greater detail, establishing clearly their connection to the initial compression of the X-point and the period of oscillatory reconnection.

- The octupolar out-of-plane magnetic field structure discovered in the simulations has not been officially observed, but could be present in the existing data taken in fly-by Cluster missions, similarly to the quadruplolar field (see Ref. [32]). A thorough analysis of the Cluster data should be conducted to determine if equivalent evidence for the octupolar field also exists.

- While the generating currents of the octupolar out-of-plane magnetic field have been determined and a parametric study was conducted on system size and mass-ratios of electrons and ions, the effect still lacks a purely theoretical framework. Dai's model of the quadrupolar magnetic field as an Alfvén resonance eigenmode (see Ref. [136]) lends it self to a multipolar extension when higher modes are included. Work has been done in comparing the results of this model to simulation results but no conclusions have been derived yet.

- Allowing for the system to evolve in the out-of-plane dimension lead to new results relating to X-point collapse (as discussed in Chapter 3), but due to computational limitations these results are still in their infancy and should undergo more extensive, parametric studies and analysis.

Appendix A

Explicit and Implicit PIC solvers

As discussed in Ref. [52] there are two types of field/particle solvers. In explicit solvers, such as the leap-frog scheme, the electric and magnetic fields defined on grid points from the previous time step are used to determine the acceleration of particles and accordingly to update particle positions on the simulation grid. This can be illustrated by the following one-dimensional formulation for a single super-particle:

$$\begin{aligned} a_i &= F(x_i)/m, \\ v_{i+1/2} &= v_{i-1/2} + a_i\,\Delta t, \\ x_i &= x_{i-1} + v_{i-1/2}\,\Delta t, \end{aligned} \tag{A.1}$$

where the index i denotes the number of the time-step and $F(x_i)$ the force experienced by the particle at location x_i. Solvers of this type however contain an inherent inaccuracy since the forces used correspond to a previous point in time and thus the size of the time-step used is of crucial importance. In order to compute all the relevant physics, the simulation time-step, Δt, is set to be sufficiently small to resolve electromagnetic and plasma waves, i. e. $c\Delta t < \Delta l$ and $\omega_{pe}\Delta t < 2$, where Δl represents the length of a simulation grid cell. It is to be noted that the accuracy also depends on the solver itself, which in the case of a leap-frog algorithm is to second order. However, for certain plasma modelling approaches, such as the Vlasov-Darwin model, the use of explicit time integration unconditionally results in the instability of the code (see Ref. [164]), thus creating a need for more accurate solvers.

In an implicit solver the forces used in the particle pusher correspond to the same time-step, leading to a more accurate representation of the particle motion and stability in a greater range of plasma calculation methods. Thus, generally a smaller time-step is required for particle dynamics and energy to be conserved. However, implicit solvers

are generally also more computationally demanding, often relying on root-finding algorithms rather than mere equation solving. Therefore there can be a computational trade-off in using an explicit solver, despite the greater number of time steps. However, improvements to implicit solvers is an active field of research, including improved analytical solutions and efficiency (for examples see Refs. [164, 165]).

Bibliography

[1] J. W. Dungey. Conditions for the occurence of electrical discharges in astrophysical systems. *Phil. Mag.*, 44:725–738, 1953.

[2] M.J. Aschwanden. *Physics of the Solar Corona*. Chichester: Praxis Publishing Ltd, 2005.

[3] M. Vogel. Physics of the Sun: A First Course, by D.J. Mullan. Scope: monograph. Level: undergraduates. *Contemporary Physics*, 52:254–254, May 2011. doi: 10.1080/00107514.2010.546886.

[4] B. W. Carroll and D. A. Ostlie. *An introduction to modern astrophysics and cosmology*. July 2006.

[5] P. A. Gilman. The tachocline and the solar dynamo. *Astronomische Nachrichten*, 326:208–217, April 2005. doi: 10.1002/asna.200410378.

[6] M. S. Miesch, M. K. Browning, A. S. Brun, J. Toomre, and B. P. Brown. Three-Dimensional Simulations of Solar and Stellar Dynamos: The Influence of a Tachocline. In M. Dikpati, T. Arentoft, I. González Hernández, C. Lindsey, and F. Hill, editors, *Solar-Stellar Dynamos as Revealed by Helio- and Asteroseismology: GONG 2008/SOHO 21*, volume 416 of *Astronomical Society of the Pacific Conference Series*, page 443, December 2009.

[7] F. G. Fuchs. Simulating waves in the solar atmosphere with mhd, 2009. URL `http://www.math.sciences.univ-nantes.fr/~berthon/conferences/castro_2009/talks/contributed/fuchs.pdf`.

[8] A. G. Kosovichev and V. V. Zharkova. X-ray flare sparks quake inside Sun. *Nature*, 393:317–318, May 1998. doi: 10.1038/30629.

[9] H. W. Babcock. The Topology of the Sun's Magnetic Field and the 22-YEAR Cycle. *ApJ*, 133:572, March 1961. doi: 10.1086/147060.

[10] UCAR. The sun-earth connection - understanding the turbulent star next door, 2006. URL `http://www.ucar.edu/news/features/solarupdate/`.

[11] P. F. Chen. Coronal mass ejections: Models and their observational basis. *Living Reviews in Solar Physics*, 8(1), 2011. doi: 10.1007/lrsp-2011-1. URL `http://www.livingreviews.org/lrsp-2011-1`.

[12] H. S. Hudson and E. W. Cliver. Observing coronal mass ejections without coronagraphs. *Journal of Geophysical Research: Space Physics*, 106(A11):25199–25213, 2001. ISSN 2156-2202. doi: 10.1029/2000JA904026. URL `http://dx.doi.org/10.1029/2000JA904026`.

[13] T. Hirayama. Theoretical Model of Flares and Prominences. I: Evaporating Flare Model. *Sol. Phys.*, 34:323–338, February 1974. doi: 10.1007/BF00153671.

[14] N. F. LOUREIRO. An introduction to magnetic reconnection, 2013. URL `http://userpages.irap.omp.eu/~frincon/houches/Loureiro.pdf`.

[15] Kazunari Shibata and Tetsuya Magara. Solar flares: Magnetohydrodynamic processes. *Living Reviews in Solar Physics*, 8(6), 2011. doi: 10.1007/lrsp-2011-6. URL `http://www.livingreviews.org/lrsp-2011-6`.

[16] C. Jiang, S. T. Wu, X. Feng, and Q. Hu. Data-driven magnetohydrodynamic modelling of a flux-emerging active region leading to solar eruption. *Nature Communications*, 7:11522, May 2016. doi: 10.1038/ncomms11522.

[17] M. Tomczak and E. Chmielewska. A Catalog of Solar X-Ray Plasma Ejections Observed by the Soft X-Ray Telescope on Board Yohkoh. *Astrophysical Journal, Supplement*, 199:10, March 2012. doi: 10.1088/0067-0049/199/1/10.

[18] K. Shibata and T. Yokoyama. Origin of the Universal Correlation between the Flare Temperature and the Emission Measure for Solar and Stellar Flares. *Astrophysical Journal, Letters*, 526:L49–L52, November 1999. doi: 10.1086/312354.

[19] H. Maehara, T. Shibayama, S. Notsu, Y. Notsu, T. Nagao, S. Kusaba, S. Honda, D. Nogami, and K. Shibata. Superflares on solar-type stars. *Nature*, 485:478–481, May 2012. doi: 10.1038/nature11063.

[20] P. A. Sturrock and Y. Uchida. Coronal heating by stochastic magnetic pumping. *ApJ*, 246:331–336, May 1981. doi: 10.1086/158926.

[21] A. A. van Ballegooijen. Cascade model of coronal heating. In A. I. Poland, editor, *NASA Conference Publication*, volume 2442 of *NASA Conference Publication*, December 1986.

[22] J. Heyvaerts, E. R. Priest, and D. M. Rust. An emerging flux model for the solar flare phenomenon. *ApJ*, 216:123–137, August 1977. doi: 10.1086/155453.

[23] J. V. Hollweg. Alfvenic heating of the chromosphere and corona. In B. W. Lites, editor, *Chromospheric Diagnostics and Modelling*, pages 235–251, 1985.

[24] C. E. Parnell and I. De Moortel. A contemporary view of coronal heating. *Philosophical Transactions of the Royal Society of London Series A*, 370:3217–3240, July 2012. doi: 10.1098/rsta.2012.0113.

[25] Eckart Marsch. Kinetic physics of the solar corona and solar wind. *Living Reviews in Solar Physics*, 3(1), 2006. doi: 10.1007/lrsp-2006-1. URL `http://www.livingreviews.org/lrsp-2006-1`.

[26] L. Ofman, S. P. Gary, and A. ViñAs. Resonant heating and acceleration of ions in coronal holes driven by cyclotron resonant spectra. *Journal of Geophysical Research (Space Physics)*, 107:1461, December 2002. doi: 10.1029/2002JA009432.

[27] M. Owens. The solar wind (in 90 minutes), 2013. URL `https://www.ucl.ac.uk/mssl/solar/summerschool13/lectures/OwensSTFCsummerSchool2013.pdf`.

[28] Mathew J. Owens and Robert J. Forsyth. The heliospheric magnetic field. *Living Reviews in Solar Physics*, 10(5), 2013. doi: 10.1007/lrsp-2013-5. URL `http://www.livingreviews.org/lrsp-2013-5`.

[29] J. T. Gosling, S. Eriksson, T. D. Phan, D. E. Larson, R. M. Skoug, and D. J. McComas. Direct evidence for prolonged magnetic reconnection at a continuous x-line within the heliospheric current sheet. , 34:L06102, March 2007. doi: 10.1029/2006GL029033.

[30] NASA. Unlocking the secrets of the electron diffusion region, 2016. URL `http://mms.gsfc.nasa.gov/science.html`.

[31] L. Trenchi, M. F. Marcucci, and R. C. Fear. The effect of diamagnetic drift on motion of the dayside magnetopause reconnection line. *Geophysics Research Letters*, 42:6129–6136, August 2015. doi: 10.1002/2015GL065213.

[32] J. P. Eastwood, T.-D. Phan, F. S. Mozer, M. A. Shay, M. Fujimoto, A. Retinò, M. Hesse, A. Balogh, E. A. Lucek, and I. Dandouras. Multi-point observations of the Hall electromagnetic field and secondary island formation during magnetic reconnection. *J. Geophys. Res. (Space Physics)*, 112:A06235, June 2007. doi: 10.1029/2006JA012158.

[33] R.O. Dendy. *Plasma Dynamics*. Clarendon Press, Oxford, UK, 1990.

[34] R. Fitzpatrick. *Plasma Physics: An Introduction*. CRC Press, Taylor Francis Group, 2014.

[35] Burgess, D. Schwartz, S. J., Owen, C. J. Introduction to particle-in-cell methods in plasma simulations, 2014. URL `http://www.sp.ph.imperial.ac.uk/~sjs/APmaster.pdf`.

[36] Ferdinand F. Cap. In *Handbook on Plasma Instabilities*. Academic Press, 1976.

[37] H. P. Furth, J. Killeen, and M. N. Rosenbluth. Finite-Resistivity Instabilities of a Sheet Pinch. *Physics of Fluids*, 6:459–484, April 1963. doi: 10.1063/1.1706761.

[38] T. K. M. Nakamura, M. Fujimoto, and A. Otto. Structure of an MHD-scale Kelvin-Helmholtz vortex: Two-dimensional two-fluid simulations including finite electron inertial effects. *Journal of Geophysical Research (Space Physics)*, 113: A09204, September 2008. doi: 10.1029/2007JA012803.

[39] P. A. Sweet. The Neutral Point Theory of Solar Flares. In B. Lehnert, editor, *Electromagnetic Phenomena in Cosmical Physics*, volume 6 of *IAU Symposium*, page 123, 1958.

[40] E. N. Parker. Sweet's Mechanism for Merging Magnetic Fields in Conducting Fluids. *Journal of Geophysical Research*, 62:509–520, December 1957. doi: 10.1029/JZ062i004p00509.

[41] E. R Priest. MHD reconnection. 6(2):2371, 2011. revision 136731.

[42] E. Priest and T. Forbes. *Magnetic reconnection: MHD theory and applications*. Cambridge University Press, 2000.

[43] H. E. Petschek. Magnetic Field Annihilation. *NASA Special Publication*, 50:425, 1964.

[44] Uzdensky, D. A. Collisional and collisionless magnetic reconnection: a review, 2009. URL `https://www-thphys.physics.ox.ac.uk/people/AlexanderSchekochihin/wpi/workshop4_pdfs/uzdensky.pdf`.

[45] D. Biskamp. Magnetic reconnection via current sheets. *Physics of Fluids*, 29: 1520–1531, May 1986. doi: 10.1063/1.865670.

[46] N. V. Erkaev, V. S. Semenov, and F. Jamitzky. Reconnection Rate for the Inhomogeneous Resistivity Petschek Model. *Phys. Rev. Lett.*, 84:1455–1458, February 2000. doi: 10.1103/PhysRevLett.84.1455.

[47] A. Otto. Geospace Environment Modeling (GEM) magnetic reconnection challenge: MHD and Hall MHD-constant and current dependent resistivity models. *Journal of Geophysics Research*, 106:3751–3758, March 2001. doi: 10.1029/1999JA001005.

[48] M. Tanaka. The origins of electrical resistivity in magnetic reconnection: Studies by 2D and 3D macro particle simulations. *Earth, Planets, and Space*, 53:463–472, June 2001. doi: 10.1186/BF03353257.

[49] D. A. Uzdensky. Petschek-like Reconnection with Current-driven Anomalous Resistivity and Its Application to Solar Flares. *Astrophysical Journal*, 587:450–457, April 2003. doi: 10.1086/368075.

[50] V. M. Vasyliunas. Theoretical models of magnetic field line merging. I. *Reviews of Geophysics and Space Physics*, 13:303–336, February 1975. doi: 10.1029/RG013i001p00303.

[51] B. U. Ö. Sonnerup. Magnetic Field Reconnection. In *Space Plasma Physics: The Study of Solar-System Plasmas. Volume 2*, page 879, 1979.

[52] Chuang Ren. Particle in cell method - a brief description of the pic method, 2013. URL `https://perswww.kuleuven.be/~u0052182/weather/pic.pdf`.

[53] F. H. Harlow. The particle-in-cell computing method for fluid dynamics. *Methods in Computational Physics*, 3:319–343, 1964.

[54] Ren, C. Introduction to particle-in-cell methods in plasma simulations, 2016. URL `http://hedpschool.lle.rochester.edu/2011SummerSchool/lectures/Ren.pdf`.

[55] D. Sydora. Low-noise electromagnetic and relativistic particle-in-cell plasma simulation models. *Journal of Computational and Applied Mathematics*, 109:243–259, September 1999.

[56] Hideo Okuda. Nonphysical noises and instabilities in plasma simulation due to a spatial grid. *Journal of Computational Physics*, 10, 1972. doi: 10.1016/0021-9991(72)90048-4.

[57] A. B. Langdon. Effects of the Spatial Grid in Simulation Plasmas. *Journal of Computational Physics*, 6:247–267, October 1970. doi: 10.1016/0021-9991(70)90024-0.

[58] J. Birn, J. F. Drake, M. A. Shay, B. N. Rogers, R. E. Denton, M. Hesse, M. Kuznetsova, Z. W. Ma, A. Bhattacharjee, A. Otto, and P. L. Pritchett. Geospace Environmental Modeling (GEM) magnetic reconnection challenge. *Journal of Geophysical Research*, 106:3715–3720, March 2001. doi: 10.1029/1999JA900449.

[59] M. A. Shay, J. F. Drake, B. N. Rogers, and R. E. Denton. Alfvénic collisionless magnetic reconnection and the Hall term. *Journal of Geophysics Research*, 106: 3759–3772, March 2001. doi: 10.1029/1999JA001007.

[60] M. M. Kuznetsova, M. Hesse, and D. Winske. Collisionless reconnection supported by nongyrotropic pressure effects in hybrid and particle simulations. *Journal of Geophysics Research*, 106:3799–3810, March 2001. doi: 10.1029/1999JA001003.

[61] P. L. Pritchett. Geospace Environment Modeling magnetic reconnection challenge: Simulations with a full particle electromagnetic code. *Journal of Geophysics Research*, 106:3783–3798, March 2001. doi: 10.1029/1999JA001006.

[62] D. Tsiklauri and T. Haruki. Physics of collisionless reconnection in a stressed X-point collapse. *Physics of Plasmas*, 15(10):102902, October 2008. doi: 10.1063/1.2999532.

[63] M. E. Mandt, R. E. Denton, and J. F. Drake. Transition to whistler mediated magnetic reconnection. *Geophys. Res. Lett.*, 21:73–76, January 1994. doi: 10.1029/93GL03382.

[64] D. Tsiklauri and T. Haruki. Magnetic reconnection during collisionless, stressed, X-point collapse using particle-in-cell simulation. *Physics of Plasmas*, 14(11): 112905, November 2007. doi: 10.1063/1.2800854.

[65] Y. Ren, M. Yamada, S. Gerhardt, H. Ji, R. Kulsrud, and A. Kuritsyn. Experimental Verification of the Hall Effect during Magnetic Reconnection in a Laboratory Plasma. *Phys. Rev. Lett.*, 95(5):055003, July 2005. doi: 10.1103/PhysRevLett.95.055003.

[66] F. S. Mozer, S. D. Bale, and T. D. Phan. Evidence of Diffusion Regions at a Subsolar Magnetopause Crossing. *Phys. Rev. Lett.*, 89(1):015002, June 2002. doi: 10.1103/PhysRevLett.89.015002.

[67] A. L. Borg, M. Øieroset, T. D. Phan, F. S. Mozer, A. Pedersen, C. Mouikis, J. P. McFadden, C. Twitty, A. Balogh, and H. Rème. Cluster encounter of a magnetic reconnection diffusion region in the near-Earth magnetotail on September 19, 2003. *Geophys. Res. Lett.*, 32:L19105, October 2005. doi: 10.1029/2005GL023794.

[68] M. A. Shay, J. F. Drake, and M. Swisdak. Two-Scale Structure of the Electron Dissipation Region during Collisionless Magnetic Reconnection. *Physical Review Letters*, 99(15):155002, October 2007. doi: 10.1103/PhysRevLett.99.155002.

[69] B. P. Sullivan, A. Bhattacharjee, and Y.-M. Huang. Extension of the electron dissipation region in collisionless Hall magnetohydrodynamics reconnection. *Physics of Plasmas*, 16(10):102111, October 2009. doi: 10.1063/1.3251423.

[70] P. A. Cassak and M. A. Shay. Magnetic Reconnection for Coronal Conditions: Reconnection Rates, Secondary Islands and Onset. , 172:283–302, November 2012. doi: 10.1007/s11214-011-9755-2.

[71] H. Ji, Y. Ren, M. Yamada, S. Dorfman, W. Daughton, and S. P. Gerhardt. New insights into dissipation in the electron layer during magnetic reconnection. , 35: L13106, July 2008. doi: 10.1029/2008GL034538.

[72] D. Tsiklauri. A new fast reconnection model in a collisionless regime. *Physics of Plasmas*, 15(11):112903–112903, November 2008. doi: 10.1063/1.3029737.

[73] T. Nakamura, R. Nakamura, and H. Haseagwa. Spatial dimensions of the electron diffusion region in anti-parallel magnetic reconnection. *Annales Geophysicae*, 34: 357–367, March 2016. doi: 10.5194/angeo-34-357-2016.

[74] P. L. Pritchett and F. V. Coroniti. Three-dimensional collisionless magnetic reconnection in the presence of a guide field. *Journal of Geophysical Research (Space Physics)*, 109:A01220, January 2004. doi: 10.1029/2003JA009999.

[75] R. Horiuchi and T. Sato. Particle simulation study of collisionless driven reconnection in a sheared magnetic field. *J. Plasma Phys.*, 4:277, 1997.

[76] T. D. Tharp, M. Yamada, H. Ji, E. Lawrence, S. Dorfman, C. E. Myers, and J. Yoo. Quantitative Study of Guide-Field Effects on Hall Reconnection in a Laboratory Plasma. *Physical Review Letters*, 109(16):165002, October 2012. doi: 10.1103/PhysRevLett.109.165002.

[77] M. Swisdak, J. F. Drake, M. A. Shay, and J. G. McIlhargey. Transition from antiparallel to component magnetic reconnection. *Journal of Geophysical Research (Space Physics)*, 110:A05210, May 2005. doi: 10.1029/2004JA010748.

[78] M. Hesse, M. Kuznetsova, and M. Hoshino. The structure of the dissipation region for component reconnection: Particle simulations. *Geophys. Res. Lett.*, 29:1563, June 2002. doi: 10.1029/2001GL014714.

[79] R. L. Fermo, J. F. Drake, and M. Swisdak. Secondary Magnetic Islands Generated by the Kelvin-Helmholtz Instability in a Reconnecting Current Sheet. *Physical Review Letters*, 108(25):255005, June 2012. doi: 10.1103/PhysRevLett.108.255005.

[80] P. A. Cassak and A. Otto. Scaling of the magnetic reconnection rate with symmetric shear flow. *Physics of Plasmas*, 18(7):074501, July 2011. doi: 10.1063/1.3609771.

[81] L. Chacón, D. A. Knoll, and J. M. Finn. Hall MHD effects on the 2D Kelvin-Helmholtz/tearing instability. *Physics Letters A*, 308:187–197, February 2003. doi: 10.1016/S0375-9601(02)01807-8.

[82] M. Hesse and S. Zenitani. Dissipation in relativistic pair-plasma reconnection. *Physics of Plasmas*, 14(11):112102, November 2007. doi: 10.1063/1.2801482.

[83] M. Melzani, R. Walder, D. Folini, C. Winisdoerffer, and J. M. Favre. Relativistic magnetic reconnection in collisionless ion-electron plasmas explored with particle-in-cell simulations. *Astronomy & Astrophysics*, 570:A111, October 2014. doi: 10.1051/0004-6361/201424083.

[84] P. A. Cassak and M. A. Shay. Scaling of asymmetric magnetic reconnection: General theory and collisional simulations. *Physics of Plasmas*, 14(10):102114, October 2007. doi: 10.1063/1.2795630.

[85] K. Malakit, M. A. Shay, P. A. Cassak, and D. Ruffolo. New Electric Field in Asymmetric Magnetic Reconnection. *Physical Review Letters*, 111(13):135001, September 2013. doi: 10.1103/PhysRevLett.111.135001.

[86] S. Markidis, P. Henri, G. Lapenta, A. Divin, M. V. Goldman, D. Newman, and S. Eriksson. Collisionless magnetic reconnection in a plasmoid chain. *Nonlinear Processes in Geophysics*, 19:145–153, February 2012. doi: 10.5194/npg-19-145-2012.

[87] P. L. Pritchett. Energetic electron acceleration during multi-island coalescence. *Physics of Plasmas*, 15(10):102105, October 2008. doi: 10.1063/1.2996321.

[88] M. Oka, T. Phan, S. Krucker, M. Fujimoto, and I. Shinohara. Electron Acceleration by Multi-Island Coalescence. *AGU Fall Meeting Abstracts*, December 2010.

[89] C. Huang, Q. Lu, M. Wu, S. Lu, and S. Wang. Out-of-plane electron currents in magnetic islands formed during collisionless magnetic reconnection. *Journal of Geophysical Research (Space Physics)*, 118:991–996, March 2013. doi: 10.1002/jgra.50185.

[90] J. F. Drake, M. Swisdak, H. Che, and M. A. Shay. Electron acceleration from contracting magnetic islands during reconnection. , 443:553–556, October 2006. doi: 10.1038/nature05116.

[91] K. Shibata and S. Tanuma. Plasmoid-induced-reconnection and fractal reconnection. *Earth, Planets, and Space*, 53:473–482, June 2001. doi: 10.1186/BF03353258.

[92] K. Shibata and S. Takasao. Fractal Reconnection in Solar and Stellar Environments. In W. Gonzalez and E. Parker, editors, *Astrophysics and Space Science Library*, volume 427 of *Astrophysics and Space Science Library*, page 373, 2016. doi: 10.1007/978-3-319-26432-5_10.

[93] Y.-M. Huang and A. Bhattacharjee. Plasmoid instability in high-Lundquist-number magnetic reconnectiona). *Physics of Plasmas*, 20(5):055702, May 2013. doi: 10.1063/1.4802941.

[94] N. F. Loureiro and D. A. Uzdensky. Magnetic reconnection: from the SweetParker model to stochastic plasmoid chains. *Plasma Physics and Controlled Fusion*, 58 (1):014021, January 2016. doi: 10.1088/0741-3335/58/1/014021.

[95] P. Priest, E. R.; Dmoulin. Three-dimensional magnetic reconnection without null points: 1. basic theory of magnetic flipping. *Journal of Geophysical Research*, 100, 1995. doi: 10.1029/95ja02740.

[96] E. R. Priest, G. Hornig, and D. I. Pontin. On the nature of three-dimensional magnetic reconnection. *Journal of Geophysical Research (Space Physics)*, 108: 1285, July 2003. doi: 10.1029/2002JA009812.

[97] P. Wyper and R. Jain. Torsional magnetic reconnection at three dimensional null points: A phenomenological study. *Physics of Plasmas*, 17(9):092902, September 2010. doi: 10.1063/1.3480639.

[98] P. F. Wyper, R. Jain, and D. I. Pontin. Spine-fan reconnection. The influence of temporal and spatial variation in the driver. *Astronomy & Astrophysics*, 545:A78, September 2012. doi: 10.1051/0004-6361/201219281.

[99] J. Threlfall, J. E. H. Stevenson, C. E. Parnell, and T. Neukirch. Particle acceleration at reconnecting separator current layers. *Astronomy & Astrophysics*, 585: A95, January 2016. doi: 10.1051/0004-6361/201527381.

[100] M. Gordovskyy, P. K. Browning, E. P. Kontar, and N. H. Bian. Particle acceleration and transport in reconnecting twisted loops in a stratified atmosphere. *Astro. Astrophys.*, 561:A72, January 2014. doi: 10.1051/0004-6361/201321715.

[101] P. L. Pritchett. Collisionless magnetic reconnection in a three-dimensional open system. *Journal of Geophysics Research*, 106:25961–25978, November 2001. doi: 10.1029/2001JA000016.

[102] H. Karimabadi, V. Roytershteyn, W. Daughton, and Y.-H. Liu. *Recent Evolution in the Theory of Magnetic Reconnection and Its Connection with Turbulence*, page 231. 2014. doi: 10.1007/978-1-4899-7413-6_9.

[103] Y.-H. Liu, W. Daughton, H. Karimabadi, H. Li, and V. Roytershteyn. Bifurcated Structure of the Electron Diffusion Region in Three-Dimensional Magnetic Reconnection. *Physical Review Letters*, 110(26):265004, June 2013. doi: 10.1103/PhysRevLett.110.265004.

[104] J. T. Dahlin, J. F. Drake, and M. Swisdak. Electron acceleration in three-dimensional magnetic reconnection with a guide field. *Physics of Plasmas*, 22 (10):100704, October 2015. doi: 10.1063/1.4933212.

[105] K. Fujimoto. Dissipation mechanism in 3D collisionless magnetic reconnection. *Journal of Physics Conference Series*, 511(1):012012, May 2014. doi: 10.1088/1742-6596/511/1/012012.

[106] S. Chapman and P. C. Kendall. Liquid Instability and Energy Transformation Near a Magnetic Neutral Line: A Soluble Non-Linear Hydromagnetic Problem. *Proceedings of the Royal Society of London Series A*, 271:435–448, February 1963. doi: 10.1098/rspa.1963.0028.

[107] V. S. Imshennik and S. I. Syrovatskiĭ. Two-dimensional Flow of an Ideally Conducting Gas in the Vicinity of the Zero Line of a Magnetic Field. *Soviet Journal of Experimental and Theoretical Physics*, 25:656, October 1967.

[108] S. I. Syrovatskiĭ. Formation of Current Sheets in a Plasma with a Frozen-in Strong Magnetic Field. *Soviet Journal of Experimental and Theoretical Physics*, 33:933, 1971.

[109] R. M. Green. Modes of annihilation and reconnection of magnetic fields. In R. Lust, editor, *Stellar and Solar Magnetic Fields*, volume 22 of *IAU Symposium*, page 398, 1965.

[110] B. V. Somov and S. I. Syrovatskii. Flare-induced physical processes in the solar atmosphere. *Uspekhi Fizicheskikh Nauk*, 120:217–257, October 1976.

[111] K. Bajer. *Flow Kinematics and Magnetic Equilibri*. PhD thesis, Cambridge Univ., Cambridge, 1990.

[112] I. J. D. Craig and A. N. McClymont. Dynamic magnetic reconnection at an X-type neutral point. *Astrophysical Journal, Letters*, 371:L41–L44, April 1991. doi: 10.1086/185997.

[113] J. A. McLaughlin, I. De Moortel, A. W. Hood, and C. S. Brady. Nonlinear fast magnetoacoustic wave propagation in the neighbourhood of a 2D magnetic X-point: oscillatory reconnection. *Astronomy & Astrophysics*, 493:227–240, January 2009. doi: 10.1051/0004-6361:200810465.

[114] P. L. Prittchet. Geospace Environment Modeling magnetic reconnection challenge: Simulations with a full particle electromagnetic code. *Journal of Geophysical Research*, 106:3783–3798, March 2001. doi: 10.1029/1999JA001006.

[115] T. D. Tharp, M. Yamada, H. Ji, E. Lawrence, S. Dorfman, C. Myers, J. Yoo, Y.-M. Huang, and A. Bhattacharjee. Study of the effects of guide field on Hall reconnection. *Physics of Plasmas*, 20(5):055705, May 2013. doi: 10.1063/1.4805244.

[116] A. S. Sharma, R. Nakamura, A. Runov, E. E. Grigorenko, H. Hasegawa, M. Hoshino, P. Louarn, C. J. Owen, A. Petrukovich, J.-A. Sauvaud, V. S. Semenov, V. A. Sergeev, J. A. Slavin, B. U. Ã-. Sonnerup, L. M. Zelenyi, G. Fruit, S. Haaland, H. Malova, and K. Snekvik. Transient and localized processes in the magnetotail: a review. *Annales Geophysicae*, 26:955–1006, May 2008. doi: 10.5194/angeo-26-955-2008.

[117] P. L. Pritchett and F. S. Mozer. Asymmetric magnetic reconnection in the presence of a guide field. *Journal of Geophysical Research (Space Physics)*, 114:A11210, November 2009. doi: 10.1029/2009JA014343.

[118] N. Singh. Propagation and dispersion of whistler waves generated by fast reconnection onset. *Physics of Plasmas*, 20(2):022106, February 2013. doi: 10.1063/1.4791650.

[119] W. Fox, M. Porkolab, J. Egedal, N. Katz, and A. Le. Observations of electron phase-space holes driven during magnetic reconnection in a laboratory plasma. *Physics of Plasmas*, 19(3):032118, March 2012. doi: 10.1063/1.3692224.

[120] J. Birn and E. R. Priest. *Reconnection of magnetic fields: magnetohydrodynamics and collisionless theory and observations*. Cambridge University Press, 2007.

[121] B. N. Rogers, R. E. Denton, J. F. Drake, and M. A. Shay. Role of Dispersive Waves in Collisionless Magnetic Reconnection. *Physical Review Letters*, 87(19): 195004, November 2001. doi: 10.1103/PhysRevLett.87.195004.

[122] A. Klassen, H. Aurass, K.-L. Klein, A. Hofmann, and G. Mann. Radio evidence on shock wave formation in the solar corona. *Astronomy and Astrophysics*, 343: 287–296, March 1999.

[123] T D Arber, K Bennett, C S Brady, A Lawrence-Douglas, M G Ramsay, N J Sircombe, P Gillies, R G Evans, H Schmitz, A R Bell, and C P Ridgers. Contemporary particle-in-cell approach to laser-plasma modelling. *Plasma Physics and Controlled Fusion*, 57(11):1–26, November 2015.

[124] H. Ruhl. *Introduction to Computational Methods in Many Body Physics*. Rinton Press, 2006.

[125] J. Villasenor and O. Buneman. Rigorous charge conservation for local electromagnetic field solvers. *Computer Physics Communications*, 69:306–316, 1992.

[126] Y. Ono, H. Tanabe, T. Yamada, M. Inomoto, I. T, S. Inoue, K. Gi, T. Watanabe, M. Gryaznevich, R. Scannell, C. Michael, and C. Z. Cheng. Ion and electron heating characteristics of magnetic reconnection in tokamak plasma merging experiments. *Plasma Physics and Controlled Fusion*, 54(12):124039, December 2012. doi: 10.1088/0741-3335/54/12/124039.

[127] O. Supplementary Material. *See supplementary material at* `ftp://ftp.aip.org/epaps/phys_plasmas/E-PHPAEN-21-028401` *for movie 1 and 2 that show the magnetic field lines (i.e. contours of the magnetic flux function) over the whole domain for the full simulation period for open and closed boundary conditions respectively, for zero guide-field; movie 3 that shows the magnetic field lines during the period of initial oscillation for the open boundary case for zero guide-field, zoomed in on the X-point; movie 4 that shows the time evolution of* $j_z(x, y)$ *in the open boundary case for guide-fields of* 0, $4B_P$ *and* $8B_P$*; movie 5 that is as movie 4 in the closed boundary case; and movie 6 that shows the time evolution of the velocity grid in the open boundary case for* $B_{Z0} = 0.8B_P$ *and thus the emergence of the electron vortex.*

[128] V. P. Pavlenko and L. Uby. Hamiltonian description and stability of magnetic electron vortices. *Physics of Fluids B*, 5:1980–1985, July 1993. doi: 10.1063/1.860786.

[129] T. M. Abdalla, B. N. Kuvshinov, T. J. Schep, and E. Westerhof. Electron vortex generation by strong, localized plasma heating. *Physics of Plasmas*, 8:3957–3966, September 2001. doi: 10.1063/1.1389299.

[130] G. P. Chernov. Morphological characteristics of solar radio bursts of the 'spike' type. *Soviet Astronomy*, 21:612–625, October 1977.

[131] A. A. Kuznetsov. Superfine Temporal Structure of the Microwave Burst on 21 April 2002: What Can We Learn about the Emission Mechanism? *Sol. Phys.*, 253:103–116, December 2008. doi: 10.1007/s11207-008-9179-7.

[132] G. P. Chernov. Solar Radio Bursts with Drifting Stripes in Emission and Absorption. *Space Science Reviews*, 127:195–326, December 2006. doi: 10.1007/s11214-006-9141-7.

[133] H. Karimabadi, J. D. Huba, D. Krauss-Varban, and N. Omidi. On the generation and structure of the quadrupole magnetic field in the reconnection process: Comparative simulation study. *Geophys. Res. Lett*, 31:L07806, April 2004. doi: 10.1029/2004GL019553.

[134] D. A. Uzdensky and R. M. Kulsrud. Physical origin of the quadrupole out-of-plane magnetic field in Hall-magnetohydrodynamic reconnection. *Physics of Plasmas*, 13(6):062305, June 2006. doi: 10.1063/1.2209627.

[135] T. D. Arber and M. Haynes. A generalized Petschek magnetic reconnection rate. *Phys. Plasmas*, 13(11):112105, November 2006. doi: 10.1063/1.2375039.

[136] T. Terasawa. Hall current effect on tearing mode instability. *Geophys. Res. Lett*, 10:475–478, June 1983. doi: 10.1029/GL010i006p00475.

[137] H. Karimabadi, D. Krauss-Varban, N. Omidi, and H. X. Vu. Magnetic structure of the reconnection layer and core field generation in plasmoids. *J. Geophys. Res.*, 104:12313–12326, June 1999. doi: 10.1029/1999JA900089.

[138] K. Arzner and M. Scholer. Kinetic structure of the post plasmoid plasma sheet during magnetotail reconnection. *J. Geophys. Res.*, 106:3827–3844, March 2001. doi: 10.1029/2000JA000179.

[139] H. Karimabadi, J. Dorelli, H. X. Vu, B. Loring, and Y. Omelchenko. Is Quadrupole Structure of Out-of-Plane Magnetic Field Evidence for Hall Reconnection? In D. Vassiliadis, S. F. Fung, X. Shao, I. A. Daglis, and J. D. Huba, editors, *American Institute of Physics Conference Series*, volume 1320 of *American Institute of Physics Conference Series*, pages 137–143, January 2011. doi: 10.1063/1.3544318.

[140] H. Karimabadi, V. Roytershteyn, C. G. Mouikis, L. M. Kistler, and W. Daughton. Flushing effect in reconnection: Effects of minority species of oxygen ions. *Planet. Space Sci.*, 59:526–536, May 2011. doi: 10.1016/j.pss.2010.07.014.

[141] P. L. Pritchett. Energetic electron acceleration during multi-island coalescence. *Physics of Plasmas*, 15(10):102105, October 2008. doi: 10.1063/1.2996321.

[142] M. Hoshino and K. Higashimori. Generation of Alfvenic Waves and Turbulence in Magnetic Reconnection Jets. *J. Geophys. Res. (Submitted)*, 2015.

[143] L. Dai. Collisionless Magnetic Reconnection via Alfvén Eigenmodes. *Physical Review Letters*, 102(24):245003, June 2009. doi: 10.1103/PhysRevLett.102.245003.

[144] J. Graf von der Pahlen and D. Tsiklauri. The effect of guide-field and boundary conditions on collisionless magnetic reconnection in a stressed X-point collapse. *Physics of Plasmas*, 21(1):012901, January 2014. doi: 10.1063/1.4861258.

[145] J. G. Graf von der Pahlen and D. Tsiklauri. Octupolar out-of-plane magnetic field structure generation during collisionless magnetic reconnection in a stressed X-point collapse. *Physics of Plasmas*, 21(6):060705, June 2014. doi: 10.1063/1.4885378.

[146] J. Graf von der Pahlen and D. Tsiklauri. The effects of ion mass variation and domain size on octupolar out-of-plane magnetic field generation in collisionless magnetic reconnection. *Physics of Plasmas*, 22(3):032905, March 2015. doi: 10.1063/1.4916128.

[147] Michael Hesse, Karl Schindler, Joachim Birn, and Masha Kuznetsova. The diffusion region in collisionless magnetic reconnection. *Physics of Plasmas*, 6(5), 1999.

[148] M. Hesse, M. Kuznetsova, and J. Birn. The role of electron heat flux in guide-field magnetic reconnection. *Physics of Plasmas*, 11:5387–5397, December 2004. doi: 10.1063/1.1795991.

[149] K. Schindler, M. Hesse, and J. Birn. General magnetic reconnection, parallel electric fields, and helicity. *Journal of Geophysical Research*, 93:5547–5557, June 1988. doi: 10.1029/JA093iA06p05547.

[150] R. G. Kleva, J. F. Drake, and F. L. Waelbroeck. Fast reconnection in high temperature plasmas. *Physics of Plasmas*, 2:23–34, January 1995. doi: 10.1063/1.871095.

[151] H. G. Mitchell, Jr. and J. R. Kan. Merging of magnetic fields with field-aligned plasma flow components. *Journal of Plasma Physics*, 20:31–45, August 1978. doi: 10.1017/S0022377800021346.

[152] A. Otto and D. H. Fairfield. Kelvin-Helmholtz instability at the magnetotail boundary: MHD simulation and comparison with Geotail observations. *Journal of Geophysics Research*, 105:21175, September 2000. doi: 10.1029/1999JA000312.

[153] Dongsheng Cai, Bertrand Lembège, Hiroshi Hasegawa, and Ken-Ichi Nishikawa. Identification of 3D Vortex structure using Cluster satellite magnetic field data. In *EGU General Assembly 2015*, pages EGU2015–10087, Vienna, Austria, April 2015. URL `https://hal-insu.archives-ouvertes.fr/insu-01143342`.

[154] G. Haller. An objective definition of a vortex. *Journal of Fluid Mechanics*, 525:1–26, February 2005. doi: 10.1017/S0022112004002526.

[155] P. Chakraborty, S. Balachandar, and R. J. Adrian. On the relationships between local vortex identification schemes. *Journal of Fluid Mechanics*, 535:189–214, July 2005. doi: 10.1017/S0022112005004726.

[156] J. C. R. Hunt, A. A. Wray, and P. Moin. Eddies, streams, and convergence zones in turbulent flows. In *Studying Turbulence Using Numerical Simulation Databases, 2*, pages 193–208, December 1988.

[157] S. D. Baalrud, A. Bhattacharjee, and Y.-M. Huang. Reduced magnetohydrodynamic theory of oblique plasmoid instabilities. *Physics of Plasmas*, 19(2):022101, February 2012. doi: 10.1063/1.3678211.

[158] C. Akçay, W. Daughton, V. S. Lukin, and Y.-H. Liu. A two-fluid study of oblique tearing modes in a force-free current sheet. *Physics of Plasmas*, 23(1):012112, January 2016. doi: 10.1063/1.4940945.

[159] C. Huang, Q. Lu, M. Wu, S. Lu, and S. Wang. Out-of-plane electron currents in magnetic islands formed during collisionless magnetic reconnection. *Journal of Geophysical Research (Space Physics)*, 118:991–996, March 2013. doi: 10.1002/jgra.50185.

[160] H. Karimabadi, V. Roytershteyn, W. Daughton, and Y.-H. Liu. *Space Science Reviews*, 178:307–323, October 2013. doi: 10.1007/s11214-013-0021-7.

[161] H. L. Kuo. Motions of Vortices and Circulating Cylinder in Shear Flow with Friction. *Journal of Atmospheric Sciences*, 26:390–398, May 1969. doi: 10.1175/1520-0469(1969)026⟨0390:MOVACC⟩2.0.CO;2.

[162] F. S. Mozer and P. L. Pritchett. Regions associated with electron physics in asymmetric magnetic field reconnection. *Geophys. Res. Lett.*, 36:L07102, April 2009. doi: 10.1029/2009GL037463.

[163] S. Zenitani, M. Hesse, A. Klimas, and M. Kuznetsova. New Measure of the Dissipation Region in Collisionless Magnetic Reconnection. *Physical Review Letters*, 106(19):195003, May 2011. doi: 10.1103/PhysRevLett.106.195003.

[164] G. Chen and L. Chacón. A multi-dimensional, energy- and charge-conserving, nonlinearly implicit, electromagnetic Vlasov-Darwin particle-in-cell algorithm. *Computer Physics Communications*, 197:73–87, December 2015. doi: 10.1016/j.cpc.2015.08.008.

[165] Pawan Kumar, Stefano Markidis, Giovanni Lapenta, Karl Meerbergen, and Dirk Roose. High performance solvers for implicit particle in cell simulation. *Procedia Computer Science*, 18:2251 – 2258, 2013. ISSN 1877-0509. doi: http://dx.doi.org/10.1016/j.procs.2013.05.396. URL `http://www.sciencedirect.com/science/article/pii/S1877050913005395`. 2013 International Conference on Computational Science.